

Diese Dissertation haben begutachtet:

.....



TECHNISCHE
UNIVERSITÄT
WIEN

DISSERTATION

Measurement of the decay $B \rightarrow D\ell\nu_\ell$
in fully reconstructed events and
determination of the CKM matrix element $|V_{cb}|$

Ausgeführt zum Zwecke der Erlangung des akademischen Grades eines Doktors der
technischen Wissenschaften unter der Leitung von

Privatdoz. Dipl.-Ing. Dr.techn. Christoph Schwanda
E141

Atominstitut der Technischen Universität Wien

eingereicht an der Technischen Universität Wien
Fakultät für Physik

von

Dipl.-Ing. Robin Glattauer

Matrikel-Nr. 0526148

Hardeggasse 67/32/4

1220 Wien

Wien, am 6.4.2016

Kurzfassung

Die Physik subatomarer Teilchen wird durch das sogenannte Standardmodell der Teilchenphysik beschrieben. In der mathematischen Formulierung einer Quanteneichfeldtheorie beschreibt es die Phänomene von Elektromagnetismus, der schwachen und der starken Wechselwirkung. Innerhalb des Standardmodells werden Übergänge zwischen Quarks unterschiedlicher Generationen durch den sogenannten Cabibbo-Kobayashi-Maskawa (CKM)-Mechanismus beschrieben. Der CKM-Mechanismus wird dargestellt durch die unitäre 3×3 CKM-Matrix V , welche Massen-Eigenzustände der Quarks in ihre schwachen Eigenzustände rotiert. Die Unitarität reduziert die freien Parameter der CKM-Matrix auf drei Winkel und eine komplexe Phase. Diese sind fundamentale Parameter des Standardmodells, das heißt sie werden darin nicht vorhergesagt und müssen experimentell bestimmt werden. Das Ziel dieser Analyse ist die Messung des Betrags von V_{cb} – jenem Element der CKM-Matrix, welches für Übergänge von Bottom-Quarks zu Charm-Quarks verantwortlich ist.

Die höchstmögliche Präzision in der Messung von $|V_{cb}|$ kann durch die Analyse semileptonischer B -Meson Zerfälle erreicht werden. Die B -Mesonen für diese Analyse wurden am Belle Experiment am KEKB Elektron-Positron Beschleuniger in Tsukuba, Japan über die $\Upsilon(4S)$ -Resonanz produziert. Eine hohe Luminosität und der dominante Zerfallsmodus $\Upsilon(4S) \rightarrow B\bar{B}$ ergeben einen Datensatz reich an B -Mesonen.

In jüngster Zeit gibt es ein gestiegenes Interesse an $|V_{cb}|$ -Messungen mit semileptonischen B -Zerfällen, das sich darin begründet, dass die beiden am besten gemessenen Zerfallskanäle $B \rightarrow D^*\ell\nu_\ell$ und $B \rightarrow X_c\ell\nu_\ell$ Diskrepanzen in der Größe von zwei bis drei Standardabweichungen zeigen. In dieser Arbeit wird der Zerfall $B \rightarrow D\ell\nu_\ell$ zum ersten Mal mit dem vollen Belle-Datensatz an der $\Upsilon(4S)$ Resonanz analysiert, welcher rund 770 Millionen $B\bar{B}$ Ereignisse beinhaltet, um Einsichten in diese Diskrepanz zu erhalten und $|V_{cb}|$ mit höherer Präzision zu bestimmen.

Einer der zentralen Aspekte dieser Arbeit ist die volle Rekonstruktion von Ereignissen durch Zusammensetzen auch des zweiten B -Mesons aus dem $\Upsilon(4S) \rightarrow B\bar{B}$ Zerfall in einem hadronischen Modus. Dies führt zu der Kenntnis der Viererimpulse aller Teilchen eines Ereignisses mit Ausnahme des Neutrinos. Auf dieses kann man jedoch durch Viererimpulserhaltung Rückschlüsse ziehen und somit Signal von Untergrund trennen. Der dazu verwendete Parameter ist die fehlende rekonstruierte Masse in dem Ereignis. Die volle Rekonstruktion resultiert in einer starken Reduktion von kombinatorischem Untergrund und erhöht die Präzision, mit der die Kinematik des Zerfalls gemessen werden kann.

Die Extraktion von $|V_{cb}|$ führt über die differentielle Zerfallsbreite von $B \rightarrow D\ell\nu_\ell$. Diese kann in einen leptonischen Strom und einen Formfaktor, welcher die hadronische Komponente beschreibt, faktorisiert werden. Ich messe die differentielle Zerfallsbreite in 10 Bins der kinematischen Variable $w = v_{B\mu}v_D^\mu$, wobei $v_{B\mu}$ und v_D^μ jeweils die Vierergeschwindigkeiten des B - und D -Mesons sind. Um $|V_{cb}|$ zu berechnen, nutze ich Formfaktor-Berechnungen von Gitter-QCD Gruppen und zwei verschiedene Methoden der Formfaktor-Parametrisierung. Ich interpretiere die gemessenen Zerfallsbreiten zuerst mit der Parametrisierung von Caprini, Lellouch und Neubert, und verwende eine Messung des Formfaktors bei $w = 0$ der FNAL/MILC Kollaboration. Daraus erhalte ich den Wert $\eta_{\text{EW}}|V_{cb}| = (40.12 \pm 1.34) \times 10^{-3}$, wobei η_{EW} nicht faktorisierbare elektroschwache Korrekturen beinhaltet. Eine etwas höhere Präzision konnte ich erreichen, indem ich die modellunabhängige Parametrisierung von Boyd, Grinstein und Lebed und mehrere Formfaktor-Daten von den Kollaborationen FNAL/MILC und HPQCD in einem kombinierten Fit verwendet habe. Dies resultiert in dem Wert $\eta_{\text{EW}}|V_{cb}| = (41.10 \pm 1.14) \times 10^{-3}$. Beide Werte liegen zwischen jenen der Messungen von $B \rightarrow D^*\ell\nu_\ell$ und $B \rightarrow X_c\ell\nu_\ell$, ohne eine davon klar zu favorisieren.

Des weiteren habe ich die Verzweigungsverhältnisse des Zerfalls $B \rightarrow D\ell\nu_\ell$ bestimmt und erhalte den gemittelten Wert $\mathcal{B}(B^0 \rightarrow D^-\ell^+\nu_\ell) = (2.31 \pm 0.03(\text{stat}) \pm 0.11(\text{syst}))\%$.

Abstract

The physics of subatomic particles is described by the so-called Standard Model of particle physics. It is formulated as a quantum gauge field theory and successfully describes electromagnetism, weak interaction and strong interaction. Within the Standard Model, the Cabibbo-Kobayashi-Maskawa (CKM) mechanism describes the transitions between quarks of different generations. This is expressed in the 3×3 CKM matrix V which rotates the mass eigenstates of quarks into their weak eigenstates. The unitarity of the matrix constrains it to 4 independent values: 3 angles and 1 complex phase. These are fundamental parameters of the Standard Model and thus need to be determined experimentally. The aim of this analysis is to measure the magnitude of V_{cb} , the entry in the CKM matrix responsible for the transition of bottom to charm quarks.

The highest precision available for the determination of $|V_{cb}|$ can be achieved by analyzing semileptonic B meson decays. The B mesons studied in this thesis were produced at the Belle experiment at the KEKB electron-positron collider in Tsukuba, Japan via the $\Upsilon(4S)$ resonance. This offers a perfect environment for the study of semileptonic B decays due to the high luminosities and the dominant decay mode of $\Upsilon(4S) \rightarrow B\bar{B}$, resulting in a data sample very rich in B mesons.

Recent years have seen a lot of interest in semileptonic B decays due to discrepancies in the order of two to three standard deviations in $|V_{cb}|$ between the best measured decay modes $B \rightarrow D^*\ell\nu_\ell$ and $B \rightarrow X_c\ell\nu_\ell$. In this analysis $B \rightarrow D\ell\nu_\ell$ is analyzed for the first time using the full Belle data sample at the $\Upsilon(4S)$ resonance containing about 770 million $B\bar{B}$ pairs to give insight into this problem and to increase the precision of the value of $|V_{cb}|$.

One of the key components of this thesis is the full reconstruction of events by also assembling the second B meson from the $\Upsilon(4S) \rightarrow B\bar{B}$ decay in a hadronic mode. This results in the knowledge of the kinematics of all involved final state particles with exception of the neutrino. 4-momentum conservation can then be used to infer the neutrino and distinguish signal from background via the mass missing in the decay. Full reconstruction greatly reduces combinatorial background and allows for high precision measurements of the $B \rightarrow D\ell\nu_\ell$ decay kinematics.

$|V_{cb}|$ is extracted using the differential decay width of $B \rightarrow D\ell\nu_\ell$ which can be decomposed into the leptonic current and a form factor describing the hadronic components. I determine the $B \rightarrow D\ell\nu_\ell$ decay width in 10 bins of the kinematic variable $w = v_{B\mu}v_D^\mu$, where $v_{B\mu}$ and v_D^μ are the 4-velocities of the B and D mesons.

In order to measure $|V_{cb}|$ I use calculations of the form factor by Lattice QCD groups and two different parameterization schemes. Interpreting the decay width with the $B \rightarrow D\ell\nu_\ell$ form-factor parameterization by Caprini, Lellouch and Neubert and using the predicted form factor at zero hadronic recoil by FNAL/MILC, the value $\eta_{\text{EW}}|V_{cb}| = (40.12 \pm 1.34) \times 10^{-3}$ is obtained, where η_{EW} accounts for non-factorizable electroweak corrections. A slightly higher precision is possible utilizing the model-independent form-factor description by Boyd, Grinstein and Lebed and using multiple form-factor data from FNAL/MILC and HPQCD, leading to the value $\eta_{\text{EW}}|V_{cb}| = (41.10 \pm 1.14) \times 10^{-3}$. In relation to $|V_{cb}|$ determined from $B \rightarrow X_c\ell\nu_\ell$ and $B \rightarrow D^*\ell\nu_\ell$, these values fall into the middle, not clearly favoring either.

I further determine the branching ratios of the decay $B \rightarrow D\ell\nu_\ell$ to be $\mathcal{B}(B^0 \rightarrow D^-\ell^+\nu_\ell) = (2.31 \pm 0.03(\text{stat}) \pm 0.11(\text{syst}))\%$.

Contents

1. Introduction	1
1.1. Natural Units	2
2. Theory	3
2.1. The Standard Model of Particle Physics	3
2.1.1. Quantum Electrodynamics	5
2.1.2. Symmetries	9
2.1.3. Electroweak Quantum Field Theory	11
2.1.3.1. The Cabibbo-Kobayashi-Maskawa Mechanism	13
2.1.3.2. CP Violation in the Bottom Quark Sector	15
2.1.4. The Strong Interaction	16
2.1.4.1. Lattice QCD	18
2.2. The Description of the Decay $B \rightarrow D\ell\nu_\ell$	20
2.2.1. Differential Decay Width	20
2.2.1.1. The Feynman Diagram	21
2.2.1.2. Reference Frames	22
W -Frame	22
B -Frame	23
2.2.1.3. The Squared Matrix Element	25
The Leptonic Matrix	25
The Hadronic Matrix	27
Product of Leptonic and Hadronic Matrices	28
2.2.1.4. Phase Space	28
2.2.1.5. Combining Phase Space and the Matrix Element	29
2.2.1.6. From q^2 to w	29
2.2.2. Heavy Quark Effective Theory	31
2.2.3. Form Factor Parameterization	32
2.2.4. Electroweak Correction Factor	34
3. Experimental Status of V_{cb}	35
4. The Belle Experiment	37
4.1. The KEKB Accelerator	38
4.2. The Belle Detector	39
4.2.1. The Interaction Region	39

4.2.2.	The Tracking System	40
4.2.2.1.	The Silicon Vertex Dector	41
4.2.2.2.	The Central Drift Chamber	42
4.2.3.	The Aerogel Cherenkov Counter	43
4.2.4.	The Time-Of-Flight Counter	44
4.2.5.	The Electromagnetic Calorimeter	44
4.2.6.	The K_L^0 and μ Detection System	45
4.2.7.	Particle Identification	45
5.	Data Sample	48
5.1.	Offline Data Processing	48
5.2.	MC Production	49
6.	Experimental Procedure	51
6.1.	Hadronic Tag	51
6.2.	Skim	53
6.3.	$B \rightarrow D\ell\nu_\ell$ Reconstruction	54
6.3.1.	Charged Lepton Reconstruction	54
6.3.2.	D Meson Reconstruction	54
6.3.3.	Further Background Suppression	59
6.3.4.	Optimization of the Selection on Monte Carlo Data	59
6.3.5.	Signal Yield Extraction	63
7.	Verification of the Procedure on Monte Carlo Data	67
7.1.	Resolution of w	67
7.2.	Validation of the Signal Yield Extraction with the Barlow-Beeston Fit	68
7.3.	Validation of the Fit Procedure	69
7.4.	Stability w.r.t. Binning	71
8.	MC Corrections	74
8.1.	Correction of Hadronic D Branching Fractions	75
8.2.	Correction of Semileptonic $B \rightarrow X_c\ell\nu_\ell$ Decays	76
8.3.	Correction of Semileptonic $B \rightarrow X_u\ell\nu_\ell$ Decays	77
8.4.	Correction of Particle Identification Efficiencies	77
8.5.	Correction of Luminosity and $\Upsilon(4S)$ Decay Widths	78
8.6.	Hadronic Tag Correction	79
8.6.1.	$B \rightarrow X\ell\nu_\ell$ Reconstruction	79
8.6.2.	Calibration Coefficients	79
8.6.3.	Comparison of Real Data and MC for $B \rightarrow X\ell\nu_\ell$	81
8.7.	Comparison of Real Data and MC	82
8.8.	Signal Peak Resolution Correction	83
9.	Results	85
9.1.	Systematic Errors	88

10. Discussion	92
10.1. CLN Parameterization Interpretation	92
10.2. Model-Independent BGL Fit	95
11. Summary	100
A. Figure of Merit of D Decay Channels	103
B. D-Mass Fits	104
C. Full Systematic Correlation Matrix	107
Bibliography	111
Acknowledgements	117

1. Introduction

The theoretical description of particle physics is currently based on the so-called Standard Model (SM). The SM is formulated as a quantum gauge field theory of the gauge group $SU(3) \times SU(2) \times U(1)$ assembled from electroweak physics which combines $U(1)$ electromagnetic and $SU(2)$ weak interactions, and $SU(3)$ quantum chromodynamics.

In the electroweak part of the Standard Model the so-called Cabibbo-Kobayashi-Maskawa (CKM) mechanism accounts for transitions between the six fundamental particles called quarks. This mixing can be described by the unitary 3×3 CKM matrix which can be reduced to 3 mixing angles and one complex phase. Those 4 parameters are fundamental properties of the SM and thus need to be measured by experiment. This analysis aims at measuring the magnitude of the matrix element V_{cb} which accounts for the transition of bottom to charm quarks. Additional motivation for the measurement of $|V_{cb}|$ comes from conflicting past measurements of $|V_{cb}|$ in the two most precise decays $B \rightarrow D^* l \nu_\ell$ and $B \rightarrow X_c l \nu_\ell$.

I extract $|V_{cb}|$ by analyzing the decay $B \rightarrow D l \nu_\ell$ in the 711 fb^{-1} data sample recorded by the Belle experiment at the $\Upsilon(4S)$ resonance. The B mesons are provided by the decays of $\Upsilon(4S) \rightarrow B\bar{B}$ amounting to over 96% of the $\Upsilon(4S)$ decay width. This results in about 772 million $B\bar{B}$ pairs produced at Belle giving it the name of a B Factory. The $B \rightarrow D l \nu_\ell$ decay is reconstructed by searching events for a charged lepton and assembling the D meson from exclusive hadronic decay products.

The neutrino is not directly detectable in the Belle detector. Its loss is compensated however, by full hadronic reconstruction of the second B meson from the $\Upsilon(4S) \rightarrow B\bar{B}$ decay and by applying 4-momentum conservation. $|V_{cb}|$ can then be extracted by analyzing the differential decay width in dependence of the decay kinematics. Additionally the branching fractions of the decay and multiple parameters of the used decay models are measured.

This thesis is organized as follows. In chapter 2 I present an introduction to the SM followed by a more detailed description of the decay $B \rightarrow D l \nu_\ell$. Chapter 3 describes the current experimental status of $|V_{cb}|$ measurements. In chapter 4 the Belle experiment is introduced. Chapter 5 details the data sample taken at Belle on which this analysis is based. In chapter 6 I explain the experimental procedure for measuring the differential decay width and in chapter 7 verifications of this procedure on Monte Carlo data are shown. Chapter 8 describes corrections applied on Monte Carlo data to account for differences to real data. In chapter 9 the resulting measured widths, branching fractions and their systematic errors are presented. Finally, in chapter 10 the widths are interpreted and $|V_{cb}|$ is extracted.

1.1. Natural Units

The preferred unit of energy for subatomic physics is the electron volt eV. Due to the energy scale of the Belle experiment most values in this text will be in the order of GeV. I follow the standard in particle physics and utilize “natural units” which set $c = 1$, $\hbar = 1$ and $\epsilon_0 = 1$. This directly relates different quantities such as length, time and momentum to powers of energy. *E.g.* momentum is expressed as energy and time is expressed as inverse energy. I omit the use of c and \hbar in the units, *e.g.* momenta are given in GeV and not GeV/ c . Missing units of c and \hbar can easily be recovered via dimensional analysis.

2. Theory

This analysis is based on the description of particle physics by the Standard Model. In this chapter I give an overview over its constituent parts with a special focus on the ingredients vital to the decay $B \rightarrow D\ell\nu_\ell$ and the theoretical description of its properties.

2.1. The Standard Model of Particle Physics

The Standard Model (SM) is one of the most successful theories in modern physics. It describes the behaviour of subatomic particles with a very high precision. Since the completion of its formalism in the 1970s it has been verified with great scrutiny, the most recent success being the discovery of the predicted Higgs Boson in 2012 at the Large Hadron Collider accelerator at CERN. While there are known deficiencies of the model, most prominently the facts that it does neither describe dark matter nor include gravity, a replacement not only capable of explaining the missing phenomena, but also holding up to experimental verification has yet to come.

While I will point out multiple important aspects of the SM, especially those of relevance to this analysis, the SM and its mathematical foundation are incredibly complex and can thus only be glossed over in a thesis. Therefore I will leave out many points of interest and recommend the books [1] and [2] for the quantum field theoretical description and [3] for a good overview and introduction into the matter.

Excluding gravity, the SM contains the other known fundamental forces of electromagnetism, the weak and the strong force. Within the SM these are actually two forces since electromagnetism and weak interaction are combined into the electroweak interaction. Likewise attempts are made at including the strong force into a so-called “Grand Unified Theory” (GUT). While at the low energy scale typical to human experience¹ electromagnetic, weak and strong force exhibit separate behaviors, at higher energies between the GeV and TeV scale electroweak unification becomes visible at modern particle physics facilities. At even higher energies of 10^{16} GeV – the so-called GUT scale – grand unification of electroweak and strong interaction is expected. Finally, at the even higher energies of the Planck scale at 10^{19} GeV, a further inclusion of gravity is necessary. Although probing effects on these scales is highly desirable, current machines – even using indirect detection mechanisms – are far from probing those energy regions and thus the SM completely suffices for the prediction of most phenomena.

¹Visible light has an energy in the order of $O(\text{eV})$, thermal processes at room temperature have an energy in the order of $O(0.01\text{eV})$.

2. Theory

The formalism of the SM is that of a quantum gauge field theory based on the gauge groups of $SU(3) \times SU(2) \times U(1)$, where $SU(2) \times U(1)$ correspond to the electroweak interaction and $SU(3)$ to the strong interaction. I will discuss the implications of the different gauge groups in the following sections.

Table 2.1 lists all particles of the Standard Model and some of their properties.

Leptons			Gauge Bosons	Higgs Boson
e 511 keV 1/2 -1	μ 105.66 MeV 1/2 -1	τ 1776.86 ± 0.12 MeV 1/2 -1	g 0 1 0	H 125.09 ± 0.24 GeV 0 0
ν_e < 2 eV 1/2 0	ν_μ < 0.19 MeV 1/2 0	ν_τ < 18.2 MeV 1/2 0	γ 0 1 0	
u $2.3^{+0.7}_{-0.5}$ MeV 1/2 2/3	c 1.275 ± 0.025 GeV 1/2 2/3	t 173.21 ± 0.87 GeV 1/2 2/3	Z 91.188 ± 0.002 GeV 1 0	
d $4.8^{+0.5}_{-0.3}$ MeV 1/2 -1/3	s 95 ± 5 MeV 1/2 -1/3	b 4.66 ± 0.03 GeV 1/2 -1/3	W 80.385 ± 0.015 GeV 1 ± 1	
Quarks			<i>spin</i>	<i>electric charge</i>

Table 2.1.: The fundamental particles of the Standard Model with their mass, spin and electric charge.

They can be categorized into four groups:

- **Leptons** are fermions with a spin of $1/2$. There are three generations increasing in mass². Each generation contains a charged lepton (electron e , muon μ and tau τ) with an electric charge³ of -1 and a neutrino with no electric charge. While charged leptons have antiparticles (*i.e.* with an electric charge of $+1$) it is not yet clear whether neutrinos are their own antiparticles or not. Leptons are subject to the electroweak force but not to the strong force.

²While originally neutrinos were assumed to be massless, it is meanwhile clear that they too must have mass - albeit small. Whether they follow the same order of higher masses for higher generations is an ongoing research.

³I list the electric charges of the particles since this is a very prominent internal quantum number. However, there are many more available such as weak isospin, color, lepton number and quark flavor numbers such as strangeness. I will depict those in the respective sections on the different interactions.

- **Quarks** are fermions with a spin of $1/2$ and a charge of either $+2/3$ (up-type quarks named up u , charm c and top t) or $-1/3$ (down-type quarks named down d , strange s and bottom b). Like leptons, quarks come in three generations increasing in mass. Each quark has a corresponding antiparticle. Quarks are subject to all known fundamental forces. Due to confinement (see section 2.1.4) quarks are found only within composite particles called hadrons. These can be further classified into mesons which contain a quark and an antiquark, and baryons which contain three quarks.
- **Gauge Bosons** are the force carriers of the Standard Model with a spin of 1. Photons (γ) relay electromagnetic interactions and are massless. This results in the infinite range of electromagnetism. They possess no electric charge and are their own antiparticles.

W^\pm and Z^0 bosons convey weak interactions. The two W bosons carry an electric charge of plus or minus one and are each other's antiparticle. The Z^0 boson has no electric charge and is its own antiparticle. The high masses of W^\pm and Z^0 lead to the short distances of the weak force and are what makes the weak interaction weak at low energy scales.

Finally, 8 types of gluons (g) are the quanta of the strong interaction. While they are massless, the gauge group $SU(3)$ from which they arise causes the range of the strong interaction to be very short.

- The **Higgs Boson** is the only fundamental particle with spin 0. In 2012 it was discovered at the mass of ~ 125 GeV at the LHC and completed the list of fundamental particles predicted by the SM. Its importance stems from being a manifestation of the Higgs-mechanism, which is an integral part of the electroweak sector of the SM. The Higgs boson carries no electric charge and is its own antiparticle.

2.1.1. Quantum Electrodynamics

The simplest sector of the Standard Model and its historically first and widely successful part is Quantum Electrodynamics (QED). It combines quantum effects with special relativity to describe electromagnetic interactions. Its success made it a blueprint for the other interactions of the Standard Model. For this reason I will review some of its details representative of the SM.

On the mathematical level QED is specified by the lagrangian density

$$\mathcal{L} = \bar{\psi}(i\gamma^\mu D_\mu - m)\psi - \frac{1}{4}F_{\mu\nu}F^{\mu\nu}. \quad (2.1)$$

2. Theory

What follows is a short derivation⁴ of this equation. Since charged leptons are spin 1/2 particles I start with the lagrangian for a free spin 1/2 particle:

$$\mathcal{L}_{\text{free},s=\frac{1}{2}} = \bar{\psi}(i\gamma^\mu\partial_\mu - m)\psi. \quad (2.2)$$

I now require invariance under a local U(1) gauge transformation:

$$\psi \longrightarrow e^{i\theta(x)}\psi. \quad (2.3)$$

Inserting the transformed ψ results in

$$\mathcal{L}_{\text{free},\frac{1}{2}} = \bar{\psi}(i\gamma^\mu\partial_\mu - m)\psi - \bar{\psi}\gamma^\mu\psi\partial_\mu\theta(x). \quad (2.4)$$

Invariance under local gauge transformations is then recovered if the additional term on the right vanishes. Since the free lagrangian does not satisfy this requirement, I add an interaction term with a new field A_μ and a coupling constant e :

$$\mathcal{L} = \bar{\psi}(i\gamma^\mu\partial_\mu - m)\psi - e\bar{\psi}\gamma^\mu A_\mu\psi. \quad (2.5)$$

If A_μ transforms under local gauge transformation as

$$A_\mu \longrightarrow A_\mu - \partial_\mu \frac{\theta(x)}{e}, \quad (2.6)$$

then applying a local gauge transformations to equation 2.5 results in the two extra terms compensating and local gauge invariance is thus restored by the addition of the vector field.

Having introduced an additional field I need to add its free field term to the lagrangian. Note that this term needs to be gauge invariant as well which is exactly satisfied by the lagrangian

$$\mathcal{L}_{\text{free},s=1} = -\frac{1}{4}F_{\mu\nu}F^{\mu\nu} \quad (2.7)$$

$$F^{\mu\nu} = \partial^\mu A^\nu - \partial^\nu A^\mu, \quad (2.8)$$

which is invariant under the transformation

$$A_\mu \longrightarrow A_\mu - \partial_\mu\lambda(x), \quad (2.9)$$

for any function $\lambda(x)$, *i.e.* it is also invariant under $\lambda(x) = \theta(x)/e$.

⁴Derivation is maybe too strong a word. I am using gauge invariance as a starting point to arrive at the QED lagrangian. Gauge invariance is also what leads to the electroweak and strong lagrangians and it thus seems to be a common characteristic of the mathematics that govern our world. However, gauge invariance is merely a first principle from where to start. The fact that the resulting lagrangian indeed seems to model particle physics is what gives it justification.

Therefore gauge invariance leads to a coupling with and the introduction of a massless vector field⁵. The free term can be identified as the lagrangian that governs the Maxwell equations and thus describes electromagnetism. The full lagrangian of QED can be written as

$$\mathcal{L} = \bar{\psi}(i\gamma^\mu\partial_\mu - m)\psi - e\bar{\psi}\gamma^\mu A_\mu\psi - \frac{1}{4}F_{\mu\nu}F^{\mu\nu} \quad (2.10)$$

$$= \bar{\psi}(i\gamma^\mu D_\mu - m)\psi - \frac{1}{4}F_{\mu\nu}F^{\mu\nu} \quad (2.11)$$

$$= \bar{\psi}(i\not{D} - m)\psi - \frac{1}{4}F_{\mu\nu}F^{\mu\nu}. \quad (2.12)$$

In the second line I introduced the covariant derivative $D_\mu = \partial_\mu + ieA_\mu$ and in the last line I introduced the so-called slash notation: $\gamma^\mu X_\mu = \not{X}$.

In order to derive cross sections or differential decay widths of processes described by this lagrangian, the typical procedure is to start from the free fields and introduce the interaction terms as perturbation⁶ For this, one derives the interaction Hamiltonian from the interaction term in the lagrangian. The evolution of an initial state to a final state is then governed by a time operator evaluated between initial and final state. The time operator consists of a time ordered exponential of an integral of the interaction Hamiltonian. For any order n of the Taylor expansion of this exponential one then has one or more integrals over multiple time ordered operators. All field operators are then decomposed into creation and annihilation operators and initial and final state are written as creation operators acting on the vacuum. The problem is then to evaluate the time ordered operators. This can be done using Wick's theorem. It prescribes how a time ordered sequence of operators can be written as a sum of multiple normal-ordered operator terms multiplied with so-called Feynman propagators. This is then a situation that can be solved, since Feynman propagators are just complex numbered functions and normal ordered operators can be applied directly on initial and final states. After inserting multiple vacuum-identities, and integrating over resulting delta functions one finally arrives at the amplitude for the interaction of two states in a given order of the expansion. One then sums up the amplitudes until an order that gives sufficient precision.

Although this is a very brief description, one sees how this process is very tedious. However, it follows a fixed set of rules and the terms appearing from Wick's theorem follow the same combinatoric patterns each time. It is thus, that Feynman introduced the Feynman rules which relate the terms from Wick's theorem to graphical representations, so-called Feynman diagrams, together with a prescription on how to collect the terms that appear in the amplitude.

⁵There is a more general form of a lagrangian for a spin 1 field which includes a mass term. However, this mass term makes gauge invariance impossible and thus the mass must be zero if gauge invariance is to hold. This basic problem is what made the Higgs mechanism necessary in order to introduce mass-like behavior of W and Z bosons without an initial mass term in the free lagrangian.

⁶Perturbative treatment works very well for the QED lagrangian, however the strong interaction in the low energy regime cannot be treated this way.

2. Theory

The Feynman rules for QED are⁷:

- For each particle in the initial state an incoming line is drawn and for each particle in the final state an outgoing line is drawn.
- Time runs symbolically from left to right.
- Photons are drawn as wavy lines, fermions as straight lines with an arrow that denotes particles (in the direction of time) or antiparticles (opposite direction).
- Vertices are connected with a line allowed by conservation laws (*e.g.* electric charge conservation).
- Each line has a 4-momentum. The outer lines correspond to the 4-momenta of the physical particles. Internal lines may have 4-momenta which do not match the mass of the particle - so-called “off-shell” or “virtual” particles.
- Each vertex conserves 4-momentum.
- The terms in the amplitude can be assembled as a product of the following constituents:
 - Each external fermion results in a spinor (typically u or v for incoming and \bar{u} , \bar{v} for outgoing ones).
 - Each external photon gives a polarization vector (typically ϵ^μ).
 - Each vertex contributes with $ie\gamma^\mu$.
 - Each internal fermion gives $\frac{i(\not{q}+m)}{q^2-m^2}$, where q is the 4-momentum of the fermion.
 - Each internal photon gives $\frac{-ig_{\mu\nu}}{q^2}$.
 - Each vertex contributes a momentum conserving delta function.
- One then integrates over the momentum of the internal line.
- Diagrams are summed up for every topologically different setup including a minus sign for diagrams that differ only in exchange of two fermions of same type.
- The result is $i\mathcal{M}(2\pi)^4\delta^4(p_1 + p_2 - p_3 - p_4)$, where \mathcal{M} is the amplitude of the scattering process as it would have been derived in the classical fashion.

The genius of the Feynman diagrams is then not only the simplification of the calculation but also the foundation to talk and describe physical processes on the particle level with an easy picture language. An example of Feynman diagrams is shown for the tree level contributions to electron-positron scattering in Figure 2.1.

⁷For the sake of brevity the Feynman rules presented here only describe tree level events with four external lines and one internal one.

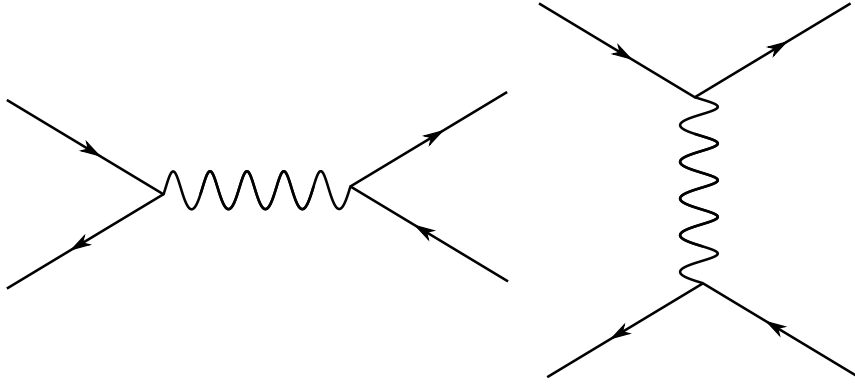


Figure 2.1.: The two Feynman diagrams on tree level that contribute to electron-positron scattering - so-called Bhabha scattering.

2.1.2. Symmetries

Having introduced the QED lagrangian is a good point to discuss symmetries in the Standard Model. There are multiple symmetries under which the Standard Model or rather its lagrangian is invariant.

Being formulated in a special relativistic fashion the Standard Model implicitly exhibits the symmetries of the Poincaré group and thus is symmetric with respect to translations, rotations and relativistic boosts. The Noether theorem [4] states that for any differentiable symmetry of the action of a system there exists a corresponding conserved quantity. For translational symmetry (in space and time) the conserved quantity is the 4-momentum and for rotations the conserved quantity is angular momentum⁸.

While the Poincaré symmetries are continuous, there also exist 3 important discrete symmetries:

- Charge conjugation (C) changes the signs of all internal quantum numbers of the involved particles. Internal quantum numbers include electric charge (thus the name of the symmetry), color charges, lepton numbers, etc. They do not include spin, mass or 4-momentum.
- Parity transformation (P) changes the sign of all spatial coordinates and is thus a reflection w.r.t. the origin of the coordinate system.
- Time reversal (T) reverses the direction of time.

Formulated as operators the eigenvalues of these symmetries are always ± 1 and applying them twice results in the original state.

⁸I left out the conserved quantity corresponding to the boost. After all the Poincaré group has 10 degrees of freedom: 3+1 for spatial and time translation, 3 for rotation and another 3 degrees of freedom for boosts. The last three result in a conservation of the position of the center of mass at time zero. Since this quantity seems trivial and has usually little impact, it is seldom mentioned in texts.

2. Theory

One very important aspect of these three symmetries is shown by the *CPT* theorem [5]: the combined application of *CPT* is a fundamental symmetry of any Lorentz invariant local quantum field theory with a lower bound on the Hamiltonian (and thus a stable vacuum). It is not possible to formulate such a theory that violates *CPT* symmetry. So far no experimental violations of *CPT* have been found. Such a discovery could be considered a revolution in particle physics.

The discussed QED lagrangian is not only invariant under *CPT* but also under the single *C*, *P* and *T* transformations. Since parity plays an important role in weak physics as discussed later, I want to have a look at the parity transformation in QED. Under parity transformation scalar fields stay unchanged, while vector fields have the sign of their spatial coordinates reversed. With that in mind, it is obvious that the free electromagnetic field term will stay exactly the same since the vector field only comes in pairs and any sign reversals will cancel⁹. The term with the spinors is more interesting. As is shown in chapter 3 of reference [2] spinors transform under parity as:

$$P : \quad \psi(t, \vec{x}) \longrightarrow \gamma^0 \psi(t, -\vec{x}) . \quad (2.13)$$

One can then see how the left side of the QED lagrangian is *P* invariant. From the spinors on the sides one gets two γ^0 matrices. In the middle every term changes sign in the spatial components due to the parity inversion. Moving the right γ^0 through to the left will change the signs in the spatial components back to their original state, because γ^0 anticommutes with the γ^i matrices, while the time-component stays untouched as γ^0 trivially commutes with itself. Once γ^0 arrives on the left side it annihilates with the other γ^0 ($\gamma^0 \gamma^0 = 1$) and the equation is back where it started.

This is only possible because of the γ^μ in between the spinors. In general any spinor bilinear can be decomposed into 5 different types:

- $\bar{\psi}\psi$ a scalar,
- $\bar{\psi}\gamma_5\psi$ a pseudoscalar,
- $\bar{\psi}\gamma^\mu\psi$ a vector,
- $\bar{\psi}\gamma^\mu\gamma_5\psi$ a pseudovector,
- $\bar{\psi}\sigma^{\mu\nu}\psi$ an antisymmetric tensor, with $\sigma^{\mu\nu} = \frac{i}{2}[\gamma^\mu, \gamma^\nu]$.

Every bilinear can be written as a combination of those five types. Note that while the scalars have one free component, the vectors have four and the antisymmetric tensor has 6 components. In sum those cover all 16 components of a real bilinear product. This grouping is very useful as each type specifies how it acts under parity.

⁹Of course the signs of the coordinates have changed from \vec{x} to $-\vec{x}$ but that has no impact since in the action the lagrangian is integrated over the whole space.

Scalars will – as the name suggests – keep unchanged under parity, pseudoscalars on the other hand will reverse their sign. Vectors will change the sign in the spatial ($\mu = 1, 2, 3$) components, while pseudovectors do not. Finally, the antisymmetric tensor changes sign in the cases where exactly one of its indices is spatial.

QED thus describes a so-called vector coupling and one can very quickly see that it is parity invariant. On the other hand, I will later show that the addition of a pseudovector component in the lagrangian of the weak interaction is what violates parity. There I will also write about the combined CP symmetry and its violation.

The next interesting symmetry is the one I applied as first principle - the gauge invariance. Since it is a complex phase it can be categorized as $U(1)$ gauge invariance, where $U(1)$ denotes a 1×1 unitary complex matrix in group theory. A similar – albeit more complex – situation will arise in the weak interaction with the group $SU(2)$ and in QCD with the group $SU(3)$. While the gauge symmetry is local, within all possible transformations it also contains a global symmetry - *i.e.* where the phase does not depend on space. Thus it also gives rise to a conserved quantity, which is the electric charge.

2.1.3. Electroweak Quantum Field Theory

One of the great successes of the Standard Model is the unification of electromagnetism and the weak interaction into an $SU(2) \times SU(1)$ gauge theory. As such the photon of QED and the gauge bosons of the weak interaction (W^\pm and Z^0) all originate from the same set of massless gauge bosons of electroweak theory - the W_i and B . A gauge theory cannot be constructed with mass terms from the outset, but the addition of the Higgs-field leads via spontaneous symmetry breaking to effective mass terms of the weak gauge bosons while the photon stays massless. The resulting bosons after symmetry breaking are linear combinations of the originals:

$$W^\pm = \frac{1}{\sqrt{2}}(W_1 \mp iW_2) \quad (2.14)$$

$$\gamma = \cos\theta_W B + \sin\theta_W W_3 \quad (2.15)$$

$$Z^0 = \cos\theta_W W_3 - \sin\theta_W B, \quad (2.16)$$

with the so-called “weak mixing angle” θ_W .

The lagrangian of electroweak theory after symmetry breaking can be split into many separate terms. These include Higgs boson interactions with itself or other particles, three and four point interactions of W^\pm and Z^0 , interactions between weak gauge bosons and fermions, and kinetic terms of all involved particles.

Of most interest for this analysis is the term describing the interaction between W^\pm and fermions, the so-called charged current:

$$\mathcal{L}_{cc} = -\frac{g}{\sqrt{2}} \left[\bar{u}_i \gamma^\mu \frac{1 - \gamma_5}{2} V_{ij} d_j + \bar{\nu}_i \gamma^\mu \frac{1 - \gamma_5}{2} \ell_i \right] W_\mu^+ + h.c. \quad (2.17)$$

2. Theory

Here, g denotes the weak coupling constant, u_i represents up-type quark spinors (*i.e.* u, c, t) and d_i represents down-type quark spinors (*i.e.* d, s, b). All spinors are given in their mass eigenstates. Charged lepton spinors are denoted with ℓ_i and neutrino spinors with ν_i . The index i is the generation number and the complete lagrangian would include a sum over i from one to three.

It is instructive to compare this lagrangian to the QED lagrangian. Looking at the leptonic part on the right, one sees that additional to a vector term (γ^μ) a pseudovector term ($\gamma^\mu\gamma_5$) appears. As discussed in section 2.1.2 it behaves under parity not like a vector, but rather an axial vector in that its spatial components do not change their signs under parity transformation. As was shown for QED, the vector component leads to a conserved parity. The pseudovector on the other hand adds a violation of parity symmetry. In early descriptions of weak interactions often the form $\gamma^\mu(1 + \epsilon\gamma_5)$ was used, assuming a small deviation from parity conservation. It turned out however, that $\epsilon = -1$ and parity is thus maximally violated in the weak interaction.

Another way to describe this effect is to look at the property of the $\frac{1-\gamma_5}{2}$ operator. Acting on a spinor this operator behaves as a projection onto left handed chiral states. One can thus say that weak interaction only acts on left handed fermions (or right handed anti-fermions). This parity violation had a huge impact on physics, because each single symmetry of CPT is conserved in both electromagnetic and strong interactions both in theoretical description and experiment¹⁰. In 1957 the famous experiment by C. S. Wu [6] added the experimental data on the situation for weak processes by examining the beta decay of Cobalt-60. The emitted electrons were observed to be preferentially emitted in the direction of the Cobalt spin and thus violated parity symmetry.

After it was clear that P symmetry was violated by the weak interaction, the question arose whether the combined CP symmetry would still hold. That this is not the case can be seen in the left term of equation 2.17; more specifically by the introduced matrix V_{ij} . This Cabibbo-Kobayashi-Maskawa matrix includes a CP violating phase as I will discuss in section 2.1.3.1.

For now I want to briefly discuss other symmetries of the weak lagrangian. The conserved quantity corresponding to the $SU(2)$ gauge invariance of the lagrangian is the so-called weak isospin. The name derives from the earlier idea of isospin. Neutrons and protons behave like similar particles under strong interactions, differing only by a quantity called isospin. Due to its $SU(2)$ nature its mathematical description resembles that of spin. The same idea was then later used to describe the weak interaction. Weak isospin T is - like spin - a vector, and the conserved quantity is actually its third component T_3 . However, the third component is often referred to as weak isospin as well.

¹⁰In general the strong interaction has the capability to violate CP and thus also T symmetry. The parameter that governs the strength of this violation however is a free parameter and seems to be zero, resulting in CP conservation in the strong interaction. So far there is no confirmed explanation of why this is the case and thus presents a typical fine tuning problem, which in literature is called the “strong CP problem”.

Charged leptons and up-type quarks have $T_3 = +\frac{1}{2}$, while neutrinos and down-type quarks have $T_3 = -\frac{1}{2}$. W^\pm bosons which couple down-type quarks to up type quarks and charged leptons to neutrinos thus carry a third isospin component of ± 1 . This further differentiates them from photons in that they carry charge themselves and this results in self-coupling terms in the lagrangian.

There are further symmetries of the electroweak lagrangian which are also true for the strong lagrangian and thus the overall SM. These are the lepton numbers¹¹ (electron number, muon number and tau number) and the quark number. Each of those is conserved in the SM and experimentally no deviations have been found¹².

Finally I want to introduce the two most important contributions to Feynman diagrams used in this analysis: the W propagator and the weak vertex factor. The weak vertex factor is¹³:

$$\frac{ig_W}{2\sqrt{2}}\gamma^\mu(1 - \gamma_5). \quad (2.18)$$

And the W propagator is:

$$\frac{-i(g_{\mu\nu} - q_\mu q_\nu / m_W^2)}{q^2 - m_W^2}. \quad (2.19)$$

For decays with q far smaller than the W mass¹⁴ that propagator can be replaced with:

$$\frac{ig_{\mu\nu}}{m_W^2}. \quad (2.20)$$

2.1.3.1. The Cabibbo-Kobayashi-Maskawa Mechanism

It is a peculiarity of the weak interaction that its quark eigenstates differ from their mass eigenstates. It is therefore that in equation 2.17 the so-called Cabibbo-Kobayashi-Maskawa (CKM) matrix V_{ij} is used to rotate the mass eigenstates into the weak eigenstates.

¹¹Lepton numbers are only exact symmetries for the case of massless neutrinos. Since the existence of neutrino masses is meanwhile established, lepton numbers are only approximate symmetries of the Standard Model.

¹²There is however a good reason to assume that quark number is violated somewhere. As we can observe, the universe seems to contain mostly matter over antimatter. To achieve such an asymmetry the quark number must be violated. Interestingly, there are two further requirements for matter-antimatter asymmetry, one of which is CP violation at a level much higher than is allowed by the weak interaction.

¹³This weak vertex factor is given for weak eigenstates. If one works with the mass eigenstates one has to add the corresponding CKM matrix element.

¹⁴This is the case for the $B \rightarrow D\ell\nu_\ell$ decay. In the B rest frame the energy of the B meson is $m_B \approx 5.28$ GeV. The largest q^2 value is reached when the D meson gets the minimum amount of energy and is also produced at rest, requiring an energy of $m_D \approx 1.87$ GeV. This leaves $5.28 - 1.87 = 3.41$ GeV and thus $q_{\max}^2 \approx 11.63$ GeV². Compared to $m_W^2 = 6461.75$ GeV² this is below 0.2%.

2. Theory

The first one to apply this principle was Cabibbo in 1963. In a time where only up, down and strange quarks were known¹⁵ he suggested a 2×2 mixing matrix and thus explained how the strange quark could change into an up quark. A unitary matrix of size $N \times N$ is reduced by unitarity to N^2 real parameters. The number of free parameters can be further reduced by absorbing phases into the quark fields. There are $2N$ fields, so since one overall phase is unphysical, $2N - 1$ degrees of freedom can be subtracted. This leaves $(N - 1)^2$ free parameters. The Cabibbo matrix thus only has one free parameter - a mixing angle.

In 1973 Kobayashi and Maskawa extended the matrix to 3 quark generations¹⁶ in order to account for CP violation. With $N = 3$ the free parameters are 3 mixing angles and one complex phase. This complex phase is the source of all CP violation in the Standard Model. The CKM mechanism thus explained CP violation and predicted a third quark generation which indeed was found later.

Denoting weak eigenstates of down-type quarks with a subscript w and their mass eigenstates with subscript m the CKM matrix rotates one into the other as

$$\begin{pmatrix} d_w \\ s_w \\ b_w \end{pmatrix} = \begin{pmatrix} V_{ud} & V_{us} & V_{ub} \\ V_{cd} & V_{cs} & V_{cb} \\ V_{td} & V_{ts} & V_{tb} \end{pmatrix} \begin{pmatrix} d_m \\ s_m \\ b_m \end{pmatrix}. \quad (2.21)$$

Note that it is only conventional to rotate the down-type quarks, one could as well rotate the up-type quarks.

Naming the complex phase $e^{i\delta}$, the three rotation angles θ_{12} , θ_{13} and θ_{23} , and abbreviating sine with s and cosine with c the CKM matrix can be written as

$$V_{ij} = \begin{pmatrix} c_{12}c_{13} & s_{12}c_{13} & s_{13}e^{-i\delta} \\ -s_{12}c_{23} - c_{12}s_{23}s_{13}e^{i\delta} & c_{12}c_{23} - s_{12}s_{23}s_{13}e^{i\delta} & s_{23}c_{13} \\ s_{12}s_{23} - c_{12}c_{23}s_{13}e^{i\delta} & -c_{12}s_{23} - s_{12}c_{23}s_{13}e^{i\delta} & c_{23}c_{13} \end{pmatrix}. \quad (2.22)$$

To give an overview of the relative sizes, the approximate values of the magnitudes are

$$\begin{pmatrix} |V_{ud}| & |V_{us}| & |V_{ub}| \\ |V_{cd}| & |V_{cs}| & |V_{cb}| \\ |V_{td}| & |V_{ts}| & |V_{tb}| \end{pmatrix} \approx \begin{pmatrix} 0.97 & 0.23 & 0.004 \\ 0.23 & 0.97 & 0.04 \\ 0.01 & 0.04 & 0.999 \end{pmatrix}. \quad (2.23)$$

¹⁵Actually, when he proposed this mechanism in 1963 the quark model was just at its start. Gell-Mann had already proposed the Eightfold way, but the term quark itself was only coined in 1964 and quarks were not confirmed until 1968. It is easier however from a modern viewpoint, to see it as a quark eigenstate problem.

¹⁶This proposal was as remarkable as Cabibbos. While the existence of quarks was already confirmed in 1973, only the lightest three quarks – up, down and strange – were known. Thus half the quarks necessary for the CKM mechanism to work were unknown when it was proposed.

2.1.3.2. CP Violation in the Bottom Quark Sector

The study of CP violation is a very wide field within particle physics. It can be studied in kaon, D and B meson systems, and via multiple decay topologies with different magnitudes of effect, interferences, and theoretical and experimental limitations. For example, one of the simpler modes, the decay of a K_L^0 meson to either $\pi^- e^+ \nu_e$ or $\pi^+ e^- \bar{\nu}_e$ shows direct CP violation via its different decay rates to those two final states. However, the size of the effect is below the percent level. In the B meson system on the other hand much stronger effects can be observed in the mixing of neutral B mesons and the subsequent decays into CP eigenstates.

A thorough description of CP violation in multiple sectors can be found in reference [7] and a good introduction into its measurements at B factories is given in reference [8]. While CP violation has a negligible impact on the decay $B \rightarrow D \ell \nu_\ell$, I want to briefly introduce it for two reasons. First, the main motivation behind the Belle experiment was the study of CP violation and the CKM mechanism in B meson systems. And second, $|V_{cb}|$ plays a role in the determination of the properties of the CKM matrix. As mentioned in the previous section the elements of the CKM matrix are all connected through unitarity of the matrix. Different measurements yield constraints of single CKM parameters as in this analysis, or yield combinations of those. In order to determine the entire matrix a combined fit including as many measurements as possible is desirable. This is done by groups such as the CKMfitter group [9] and $|V_{cb}|$ is one of multiple input parameters.

CP violating decays can be grouped into three distinct categories:

- **CP violation in decay** happens when the amplitudes for a decay and its CP conjugation have different magnitudes. The mentioned $K_L^0 \rightarrow \pi^- e^+ \nu_e$ decay is an example of this. An example in the B meson sector as studied at Belle is the decay $B^+ \rightarrow K^+ K^- \pi^+$ [10].
- **CP violation in mixing** only concerns neutral particles and denotes CP violation in the mixing between the two neutral states. An example of this are the decays $B^0 \rightarrow X^- \ell^+ \nu_\ell$, where CP violating mixing with \bar{B}^0 results in a slightly different amplitude than for the conjugate mode $\bar{B}^0 \rightarrow X^+ \ell^- \bar{\nu}_\ell$. However, this effect is very small, below 0.001.
- **CP violation in interference between a decay without mixing and a decay with mixing** describes asymmetries in the rates of the direct decay $B \rightarrow f$ and the decay over mixing $B \rightarrow \bar{B} \rightarrow f$, where f is a common final state to both B and \bar{B} . An example is the decay $B^0 \rightarrow J/\Psi K_S^0$ [11].

The largest impact of CP violation in the B sector is seen in the third category, and the decay $B^0 \rightarrow J/\Psi K_S^0$ is considered its golden mode. Experimentally the $J/\Psi \rightarrow \ell^+ \ell^-$ decay has a very clean signature, and the $K_S^0 \rightarrow \pi^+ \pi^-$ decays are also well reconstructable. From a theoretical viewpoint the decay has the advantage of a very small contribution from so-called ‘‘penguin’’ diagrams.

2. Theory

The asymmetry of the decay is given by [7]:

$$\mathcal{A}(t) \equiv \frac{\Gamma(\bar{B}^0 \rightarrow J/\Psi K_S^0) - \Gamma(B^0 \rightarrow J/\Psi K_S^0)}{\Gamma(\bar{B}^0 \rightarrow J/\Psi K_S^0) + \Gamma(B^0 \rightarrow J/\Psi K_S^0)} = \sin(|\Delta m|t) \sin(2\phi_1). \quad (2.24)$$

Here, Δm is the mass difference between the two mass eigenstates of the neutral B mesons and ϕ is an angle defined as¹⁷:

$$\phi_1 \equiv \arg \left(\frac{-V_{cd}V_{cb}^*}{V_{td}V_{tb}^*} \right). \quad (2.25)$$

In experiments such as Belle, the B^0 and \bar{B}^0 meson are produced from the $\Upsilon(4S)$ resonance in an entangled state - a typical example of an Einstein-Podolsky-Rosen situation. When one of them decays, the wave function collapses and the type of the second meson is determined¹⁸. Determining the type of one B meson – so-called tagging – allows knowledge about the second one. This leads to a formulation similar to equation 2.24, but with a time Δt relative to the decay time of the tagged B meson. However, an average over time would integrate out the asymmetry. Thus measuring CP violation in such a setup requires to resolve the decay times of both B mesons. Unfortunately, the lifetime of the B meson limits its flight length to about $30 \mu\text{m}$ in the $\Upsilon(4S)$ rest frame. That is much too short for measuring the decay times via vertex displacement. As I will explain in chapter 4 this had an important impact on the design of the Belle experiment.

2.1.4. The Strong Interaction

The final ingredient to the Standard Model is the strong interaction. Historically a hint about its fundamentals was presented with the Δ^{++} meson. Consisting of three up quarks with aligned spin and with no further angular momentum it provided a conundrum: how can three identical fermions exist in a bound state all in the same configuration without violating the Pauli principle? The answer was the addition of another internal quantum number: color charge, which obviously needs (at least) 3 possible values, which are called red, green and blue. The color scheme is a useful visualization since in the additive color model their combination results in white and all known hadrons are in a “white” configuration. These colors are what lends the theory of strong interaction its name of quantum chromodynamics (QCD).

¹⁷The unitarity of the CKM matrix can be expressed with so-called “unitarity triangles”. There are six such triangles, the most prominent one arises from the unitarity equation $V_{ud}V_{ub}^* + V_{cd}V_{cb}^* + V_{td}V_{tb}^* = 0$. Three complex values summing up to zero can be expressed as a triangle in the complex plane. ϕ_1 , ϕ_2 and ϕ_3 are then the angles of this triangle. In the CKM mechanism all triangles have the same non-zero area and thus finite angles.

¹⁸Note that the type of the second B meson is only fixed for the moment in which the first one decays. Afterwards it will keep mixing with its conjugate state.

A gauge theory resulting in 3 charges is reached by using the $SU(3)$ gauge group. Using $SU(3)$, QCD can be constructed in the same fashion as QED, but the difference between $U(1)$ and $SU(3)$ leads to fundamental changes. First, the quantum of the interaction field – the gluon – is massless like the photon, but in contrast carries color charge itself. For this reason the gluons couple to themselves. The impact of that can hardly be overstated. A property of QED I have not mentioned so far is the so-called “screening”. The effective charge of any electromagnetic particle decreases with distance. This is due to vacuum polarization: virtual electron-positron pairs shield the charge - analogous to polarization in a dense medium. In terms of Feynman diagrams this comes dominantly from chains of electron-positron loops (see Figure 2.2). Summing over these components in higher and higher orders leads to a decrease in coupling with higher distances (or equivalently lower energies).

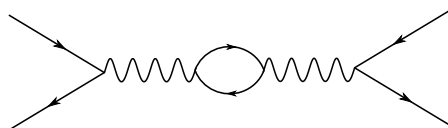


Figure 2.2.: An electron-positron pair loop in QED in the one-loop order. The dominating contribution to vacuum polarization in QED comes from chains of such loops.

The quark-antiquark loops of QCD have exactly the same effect. However, additional to virtual quark-antiquark pairs the self-coupling of gluons adds similar diagrams with gluon loops (see Figure 2.3). Summing over these contributions from gluon loops has the opposite effect of screening, termed “anti-screening”.

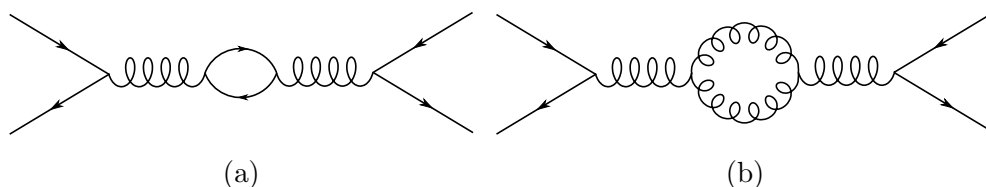


Figure 2.3.: Possible contributions to vacuum polarization in QCD in the one loop order. a) shows a quark-antiquark loop which results in screening. b) shows a gluon-gluon loop which contributes to anti-screening.

In sum, the impact of the gluons loops exceeds the impact of the quark-antiquark loops. This results in a running coupling that is the opposite of that in QED: the lower the energy (or the higher the distances) the stronger the color force gets. The coupling constant goes as

$$\alpha_S(|q^2|) \propto \frac{1}{(11n - 2f)\ln(|q^2|/\Lambda_{\text{QCD}}^2)}. \quad (2.26)$$

2. Theory

The constant Λ_{QCD} is in the order of 200 MeV. The integers n and f are the number of colors and flavors in QCD respectively. Thus it is due to the 3 colors and 6 flavors of quarks that QCD exhibits an anti-screening behavior. There are two phenomena linked to the running coupling constant. First, at high energies quarks and gluons act like free particles and can be treated perturbatively. This is called asymptotic freedom. On the other hand for low energies the force between quarks increases linearly with distance. Quarks and gluons are confined to colorless compounds. If the distance of a quark from the others within the colorless compound grows, the energy increases linearly with the distance until new particles are created that lead to two separate colorless states. One can thus never find quarks or gluons in an unbound state. This is called confinement¹⁹. The problem is, that this behavior makes QCD not accessible to perturbation theory at small energies.

The lagrangian of QCD is²⁰

$$\mathcal{L} = \bar{\psi}_\alpha (i\not{D}_{\alpha\beta} - m\delta_{\alpha\beta}) \psi_\beta - \frac{1}{4} G_{\mu\nu}^a G_a^{\mu\nu}. \quad (2.27)$$

This resembles the lagrangian for QED, but instead of $U(1)$, the symmetry group at hand is $SU(3)$. This results in the sums over α and β which run from 1 to 3, representing the three colors and in the field strength tensor having an index a running from 1 to 8. Further, an additional term appears in the field strength tensor:

$$G_{\mu\nu}^a = \partial_\mu \mathcal{A}_\nu^a - \partial_\nu \mathcal{A}_\mu^a + g f^{abc} \mathcal{A}_\mu^b \mathcal{A}_\nu^c, \quad (2.28)$$

where \mathcal{A}_ν^a are the gluon fields and f^{abc} are the so-called structure constants of QCD. It is the additional term which gives rise to the gluon carrying color charges and consequently its self-interactions.

2.1.4.1. Lattice QCD

Asymptotic freedom of QCD means that one can calculate high energy interactions such as jets with perturbation theory, but low energy states like bound states cannot be treated perturbatively.

The idea behind lattice QCD (LQCD) is to evaluate the system at hand on a discrete Euclidean space-time grid. On this grid the path integrals (from the path integral formulation of QCD) can be evaluated numerically. Fermions are placed on the lattice sites and gluons on the links between those sites. The lagrangian can then be formulated in such a way that when the lattice spacing is taken to zero the action of the continuum theory is recovered. Hadronic states are then placed and calculated on the lattice in different spacings and then extrapolated to the continuum.

¹⁹Proving confinement in QCD is highly non-trivial. To this day there is no analytical proof of this phenomenon although it can be shown to arise in Lattice QCD.

²⁰For the sake of brevity the sum over flavors is omitted here.

While LQCD is a great way to calculate low energy QCD from first principles without relying on phenomenology, it has multiple complications. First, the evaluation of the path integrals is computationally intensive and since it is done on a multidimensional grid the required computing power rises very fast with more lattice points or smaller lattice spacing. LQCD thus requires modern supercomputers to perform its calculations.

Other difficulties arise from artifacts of the discrete lattice. For example, fermions on the lattice come with the usual derivative term in the action. Working on a lattice, the derivative is replaced with a symmetric difference. This however introduces for every fermion a second unphysical fermion called “doubler”. The Nielsen-Ninomiya theorem [12] states that it is impossible to define lattice fermions with continuum-like (chiral) symmetries without introducing these doublers. To counteract their impact, so-called “clover” fermions are used which introduce additional terms to the lagrangian resulting in doublers vanishing in the continuum extrapolation.

Similar to this example there is a multitude of specialized techniques to deal with artifacts, to reduce computational load or to reduce statistic and systematic errors. The two Lattice QCD calculations I am using in this analysis contain multiple of those. However, since LQCD is a very wide and complicated topic in itself I will not go into its details here. For a good introduction see the review chapter “Lattice quantum chromodynamics” in reference [13].

2.2. The Description of the Decay $B \rightarrow D\ell\nu_\ell$

With the Standard Model introduced, I want to discuss the specifics of the decay $B \rightarrow D\ell\nu_\ell$ which I will use to extract $|V_{cb}|$. In this section I will show how to derive the differential decay width and discuss some of the aspects that enter into the calculation.

2.2.1. Differential Decay Width

The differential decay width of $B \rightarrow D\ell\nu_\ell$ can be found in the literature [8] as

$$\frac{d\Gamma}{dw} = \frac{G_F^2 m_D^3}{48\pi^3} (m_B + m_D)^2 (w^2 - 1)^{3/2} \eta_{EW}^2 |V_{cb}|^2 \mathcal{G}(w)^2. \quad (2.29)$$

Here, w is the product of the 4-velocities of the B and D meson

$$w = v_{B\mu} v_D^\mu, \quad (2.30)$$

and G_F is the Fermi constant defined as

$$G_F = \frac{\sqrt{2}g_W^2}{8m_W^2}. \quad (2.31)$$

m_B and m_D are the masses of the B and D meson respectively. The electroweak correction factor η_{EW} takes into account electroweak interactions between leptonic and hadronic current and will be discussed in section 2.2.4. $|V_{cb}|$ is the magnitude of the CKM matrix linking b and c quarks. Note that the charged lepton ℓ discussed here is a light charged lepton, *i.e.* electron or muon. For taus both theoretical description and experimental reconstruction exhibit additional complications. Finally, $\mathcal{G}(w)$ is a hadronic form factor which takes into account the hadronic dynamics of the decay.

In order to derive this formula I start at Fermi's golden rule for a relativistic quantum field theory

$$d\Gamma = \frac{1}{2m_B} |\mathcal{M}|^2 d\Pi_3, \quad (2.32)$$

where $d\Pi_3$ is the Lorentz invariant phase space (LIPS). In the following, I will first calculate the matrix element \mathcal{M} starting from the Feynman rules and then derive the corresponding phase space before combining the results.

2.2.1.1. The Feynman Diagram

Treating only the bare quarks involved in the weak process of the decay, the Feynman diagram looks as in Figure 2.4a. Using the Feynman rules for weak interaction

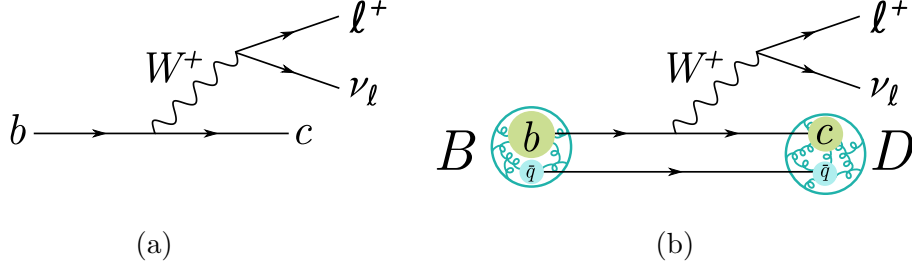


Figure 2.4.: Feynman diagram of the semileptonic decay of a b to a c quark, with bare quarks (a) and within the context of the mesons of the $B \rightarrow D\ell\nu_\ell$ decay (b). The multiple gluon lines in the hadrons symbolize the complicated nature of the bound hadronic state.

discussed in section 2.1.3 one can write down the matrix element \mathcal{M} as

$$\mathcal{M} = \left[\bar{u}_\ell \frac{-ig_W}{2\sqrt{2}} \gamma^\mu (1 - \gamma_5) v_\nu \right] \frac{ig_{\mu\nu}}{m_W^2} \left[\bar{c} V_{cb} \frac{-ig_W}{2\sqrt{2}} \gamma^\nu (1 - \gamma_5) b \right], \quad (2.33)$$

where u_ℓ , v_ν , c and b are the spinors of the charged lepton, neutrino, charm quark and bottom quark respectively. Note that no integration over internal W momentum (q) is involved since I used the W propagator for low energies from equation 2.19. This is often referred to as “integrating out” the degrees of freedom of the W . Reorganizing and using the Fermi constant G_F results in

$$\mathcal{M} = -i \frac{G_F}{\sqrt{2}} V_{cb} [\bar{u}_\ell \gamma^\mu (1 - \gamma_5) v_\nu] [\bar{c} \gamma_\mu (1 - \gamma_5) b]. \quad (2.34)$$

For the complete $B \rightarrow D\ell\nu_\ell$ decay as shown in Figure 2.4b one needs to include the interaction of the b and c quark with their hadronic environment and thus insert the states of B and D meson:

$$\mathcal{M} = -i \frac{G_F}{\sqrt{2}} V_{cb} [\bar{u}_\ell \gamma^\mu (1 - \gamma_5) v_\nu] \langle D | \bar{c} \gamma_\mu (1 - \gamma_5) b | B \rangle. \quad (2.35)$$

I will refer to the left bracket as the leptonic current L^μ and the right one as the hadronic current H_μ :

$$L^\mu = \bar{u}_\ell \gamma^\mu (1 - \gamma_5) v_\nu \quad (2.36)$$

$$H_\mu = \langle D | \bar{c} \gamma_\mu (1 - \gamma_5) b | B \rangle \quad (2.37)$$

$$\mathcal{M} = -i \frac{G_F}{\sqrt{2}} V_{cb} L^\mu H_\mu. \quad (2.38)$$

2. Theory

The reason semileptonic decays such as $B \rightarrow D\ell\nu_\ell$ are preferred for $|V_{cb}|$ measurements is this factorization into a leptonic and hadronic current which can be evaluated separately. This is not possible for hadronic decays. However, the factorization presented here is only valid at the tree level and higher order corrections need to be taken into account with an electroweak correction factor. This will be discussed in section 2.2.4.

2.2.1.2. Reference Frames

Before evaluating the matrix element and the phase space, it is useful to define the reference frames which will be used in the process and to establish some relations. There are two reference frames which are especially convenient: the rest frame of the virtual W boson (W -frame) and the rest frame of the B meson (B -frame). I first define q^μ as usual as the 4-momentum of the virtual W :

$$q^\mu = p_W^\mu = p_B^\mu - p_D^\mu = p_\ell^\mu + p_\nu^\mu. \quad (2.39)$$

Its square ($q^2 = q^\mu q_\mu$) is then the mass of the virtual W .

W -Frame I will denote quantities in the W -frame with a hat, such as \hat{p}_ℓ^μ . Figure 2.5 shows a schematic of the W -frame.

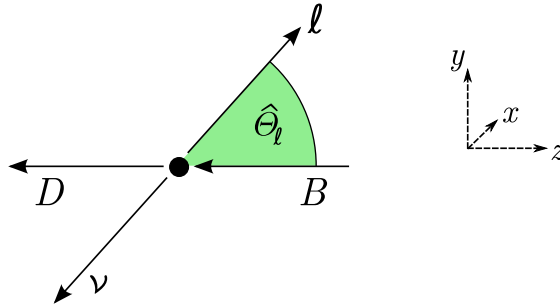


Figure 2.5.: Kinematics in the W -Frame. Charged lepton and neutrino are produced back-to-back, *i.e.* with opposite 3-momenta. The D meson carries the same 3-momentum as the incoming B meson.

Without loss of generality I choose the direction of the B meson as the negative z -axis and the plane in which the decay happens as the yz -plane. Since the W is at rest and due to 3-momentum conservation it follows that

$$\hat{p}_\ell = -\hat{p}_\nu. \quad (2.40)$$

Assuming zero lepton mass²¹:

$$\hat{p}_\ell^\mu = \begin{pmatrix} |\hat{p}_\ell| \\ \hat{p}_\ell \end{pmatrix}, \hat{p}_\nu^\mu = \begin{pmatrix} |\hat{p}_\ell| \\ -\hat{p}_\ell \end{pmatrix}. \quad (2.41)$$

²¹Since I am working with light charged leptons, their masses ($m_e \approx 0.5$ MeV and $m_\mu \approx 106$ MeV) are much smaller than the involved momenta.

2.2. The Description of the Decay $B \rightarrow D\ell\nu_\ell$

From

$$(\hat{p}_\ell^\mu + \hat{p}_\nu^\mu)^2 = q^2, \quad (2.42)$$

follows

$$|\hat{p}_\ell| = \frac{q}{2}. \quad (2.43)$$

The 3-momentum of the B meson is completely passed on to the D meson:

$$\hat{p}_B = \hat{p}_D, \quad (2.44)$$

and the 4-momentum of the B can thus be written as:

$$\hat{p}_B^\mu = \begin{pmatrix} \hat{E}_\ell + \hat{E}_\nu + \hat{E}_D \\ \hat{p}_D \end{pmatrix} = \begin{pmatrix} q + \hat{E}_D \\ \hat{p}_D \end{pmatrix}. \quad (2.45)$$

The invariant mass of the B meson can then be expressed as

$$m_B^2 = \hat{p}_B^2 \quad (2.46)$$

$$= q^2 + 2q\hat{E}_D + \hat{E}_D^2 - |\hat{p}_D|^2 \quad (2.47)$$

$$= q^2 + 2q\hat{E}_D + m_D^2. \quad (2.48)$$

Rearranging for \hat{E}_D yields

$$\hat{E}_D = \frac{m_B^2 - m_D^2 - q^2}{2q}. \quad (2.49)$$

The magnitude of the D momentum is then

$$|\hat{p}_D| = \sqrt{\hat{E}_D^2 - m_D^2} \quad (2.50)$$

$$= \sqrt{\frac{(m_B^2 - m_D^2 - q^2)^2}{4q^2} - m_D^2}. \quad (2.51)$$

B -Frame I will denote quantities in the B -frame with a tilde, such as \tilde{p}_ℓ^μ . In the B rest frame the B meson has zero 3-momentum:

$$\tilde{p}_B^\mu = \begin{pmatrix} m_B \\ 0 \end{pmatrix}, \quad (2.52)$$

and

$$\tilde{p}_D^\mu = \tilde{p}_B^\mu - \tilde{q}^\mu = \begin{pmatrix} m_B - \tilde{q}^0 \\ \tilde{\vec{q}} \end{pmatrix}. \quad (2.53)$$

2. Theory

This time I use the invariant mass of the D meson

$$m_D^2 = \tilde{p}_D^2 \quad (2.54)$$

$$= m_B^2 - 2m_B\tilde{q}^0 + (\tilde{q}^0)^2 - |\tilde{\vec{q}}|^2 \quad (2.55)$$

$$= m_B^2 - 2m_B\tilde{q}^0 + q^2, \quad (2.56)$$

and solve for \tilde{q}^0 :

$$\tilde{q}^0 = \frac{m_B^2 - m_D^2 + q^2}{2m_B}. \quad (2.57)$$

The energy of the D meson is thus

$$\tilde{E}_D = \frac{m_B^2 + m_D^2 - q^2}{2m_B}, \quad (2.58)$$

and the magnitude of its 3-momentum can be evaluated to be

$$|\tilde{\vec{p}}_D| = \sqrt{\tilde{E}_D^2 - m_D^2} \quad (2.59)$$

$$= \sqrt{\frac{(m_B^2 + m_D^2 - q^2)^2}{4m_B^2} - m_D^2}. \quad (2.60)$$

To relate this quantity to the same quantity in the W -frame I multiply by m_B/q :

$$\frac{m_B|\tilde{\vec{p}}_D|}{q} = \sqrt{\frac{(m_B^2 + m_D^2 - q^2)^2}{4q^2} - \frac{m_D^2 m_B^2}{q^2}} \quad (2.61)$$

$$= \sqrt{\frac{(m_B^2 + m_D^2 - q^2)^2 - 4m_D^2 m_B^2}{4q^2}} \quad (2.62)$$

$$= \sqrt{\frac{(m_B^2 - m_D^2 - q^2)^2 + 4m_D^2 m_B^2 - 4m_D^2 q^2 - 4m_D^2 m_B^2}{4q^2}} \quad (2.63)$$

$$= \sqrt{\frac{(m_B^2 - m_D^2 - q^2)^2 - 4m_D^2 q^2}{4q^2}} \quad (2.64)$$

$$= \sqrt{\frac{(m_B^2 - m_D^2 - q^2)^2}{4q^2} - m_D^2} = |\hat{\vec{p}}_D|, \quad (2.65)$$

and thus:

$$|\hat{\vec{p}}_D| = \frac{m_B|\tilde{\vec{p}}_D|}{q}. \quad (2.66)$$

2.2.1.3. The Squared Matrix Element

In this section there will be a lot of indices. As a general rule ν and ℓ are used exclusively to denote the charged lepton and the neutrino and are not used to indicate a co- and contravariant indices.

Squaring equation 2.38 yields

$$|\mathcal{M}|^2 = \frac{G_F^2 |V_{cb}|^2}{2} L^\mu L^{\rho*} H_\mu H_\rho^*. \quad (2.67)$$

The Leptonic Matrix I will start by examining the leptonic matrix $L^\mu L^{\rho*}$

$$L^\mu L^{\rho*} = [\bar{u}_\ell \gamma^\mu (1 - \gamma_5) v_\nu] [\bar{u}_\ell \gamma^\rho (1 - \gamma_5) v_\nu]^*. \quad (2.68)$$

This equation still contains multiple spin configurations. Since I am only interested in the spin-averaged result, I use the trace-formula for spin averaging (see *e.g.* chapter “Spin Sums” in reference [1]).

$$L^\mu L^{\rho*} = Tr[\gamma^\mu (1 - \gamma_5) (\not{p}_\nu + m_\nu) \gamma^0 (\gamma^\rho (1 - \gamma_5))^\dagger \gamma^0 (\not{p}_\ell + m_\ell)] \quad (2.69)$$

$$= Tr[\gamma^\mu (1 - \gamma_5) \not{p}_\nu \gamma^0 (\gamma^\rho (1 - \gamma_5))^\dagger \gamma^0 \not{p}_\ell] \quad (2.70)$$

$$= Tr[\gamma^\mu (1 - \gamma_5) \not{p}_\nu \gamma^0 (1 - \gamma_5) \gamma^{\rho\dagger} \gamma^0 \not{p}_\ell] \quad (2.71)$$

$$= p_{\nu\alpha} p_{\ell\beta} Tr[\gamma^\mu (1 - \gamma_5) \gamma^\alpha \gamma^0 (1 - \gamma_5) \gamma^{\rho\dagger} \gamma^0 \gamma^\beta]. \quad (2.72)$$

Here, I first ignored the light masses of the leptons, applied the hermitian conjugate and then moved the momenta outside the brackets. Multiplying out the brackets and using $Tr(A + B) = Tr(A) + Tr(B)$ gives

$$L^\mu L^{\rho*} = p_{\nu\alpha} p_{\ell\beta} \{ Tr[\gamma^\mu \gamma^\alpha \gamma^0 \gamma^{\rho\dagger} \gamma^0 \gamma^\beta] + Tr[\gamma^\mu \gamma_5 \gamma^\alpha \gamma^0 \gamma_5 \gamma^{\rho\dagger} \gamma^0 \gamma^\beta] \\ - Tr[\gamma^\mu \gamma_5 \gamma^\alpha \gamma^0 \gamma^{\rho\dagger} \gamma^0 \gamma^\beta] - Tr[\gamma^\mu \gamma^\alpha \gamma^0 \gamma_5 \gamma^{\rho\dagger} \gamma^0 \gamma^\beta] \}. \quad (2.73)$$

Moving the γ_5 matrices to the left taking into account that they anticommute with the other gamma matrices, results in

$$L^\mu L^{\rho*} = p_{\nu\alpha} p_{\ell\beta} \{ 2Tr[\gamma^\mu \gamma^\alpha \gamma^0 \gamma^{\rho\dagger} \gamma^0 \gamma^\beta] + 2Tr[\gamma_5 \gamma^\mu \gamma^\alpha \gamma^0 \gamma^{\rho\dagger} \gamma^0 \gamma^\beta] \} \quad (2.74)$$

$$= p_{\nu\alpha} p_{\ell\beta} \{ 2Tr[\gamma^\mu \gamma^\alpha \gamma^\rho \gamma^\beta] + 2Tr[\gamma_5 \gamma^\mu \gamma^\alpha \gamma^\rho \gamma^\beta] \}. \quad (2.75)$$

Formulas for traces of gamma matrices can be found in most quantum field theory textbooks, for example in the section “Trace Technology” of reference [2]. Here, I will use

$$Tr[\gamma^\mu \gamma^\alpha \gamma^\rho \gamma^\beta] = 4(g^{\mu\alpha} g^{\rho\beta} - g^{\mu\rho} g^{\alpha\beta} + g^{\mu\beta} g^{\alpha\rho}) \quad (2.76)$$

$$Tr[\gamma_5 \gamma^\mu \gamma^\alpha \gamma^\rho \gamma^\beta] = -4i\epsilon^{\mu\alpha\rho\beta}. \quad (2.77)$$

And thus:

$$L^\mu L^{\rho*} = 8p_{\nu\alpha} p_{\ell\beta} (g^{\mu\alpha} g^{\rho\beta} - g^{\mu\rho} g^{\alpha\beta} + g^{\mu\beta} g^{\alpha\rho} - i\epsilon^{\mu\alpha\rho\beta}) \quad (2.78)$$

$$= 8(p_\nu^\mu p_\ell^\rho - g^{\mu\rho} (p_{\nu\alpha} p_\ell^\alpha) + p_\ell^\mu p_\nu^\rho) - 8ip_{\nu\alpha} p_{\ell\beta} \epsilon^{\mu\alpha\rho\beta}. \quad (2.79)$$

2. Theory

This expression further simplifies in the W -frame. As a reminder, in the W -frame:

$$\hat{p}_\ell^0 = \hat{p}_\nu^0 = \frac{q}{2} \quad (2.80)$$

$$\hat{\vec{p}}_\ell = -\hat{\vec{p}}_\nu \quad (2.81)$$

$$\hat{p}_\ell \hat{p}_\nu = -\frac{q^2}{4} \quad (2.82)$$

$$\hat{p}_{\nu\alpha} \hat{p}_\ell^\alpha = \frac{q^2}{2}. \quad (2.83)$$

With this, the non-spatial components (*i.e.* where μ and/or ρ are 0) vanish. To see that this is indeed the case, I start with the energy component ($\mu = 0, \rho = 0$):

$$\hat{L}^0 \hat{L}^{0*} = 8(p_\nu^0 p_\ell^0 - g^{00}(p_{\nu\alpha} p_\ell^\alpha) + p_\ell^0 p_\nu^0) - 8i p_{\nu\alpha} p_{\ell\beta} \epsilon^{0\alpha\beta} \quad (2.84)$$

$$= 8\left(\frac{q^2}{4} - \frac{q^2}{2} + \frac{q^2}{4}\right) \quad (2.85)$$

$$= 0. \quad (2.86)$$

Next, I will examine the mixed components by looking at $\mu = 0$ and $\rho = i = 1, 2, 3$.

$$\hat{L}^0 \hat{L}^{i*} = 8(p_\nu^0 p_\ell^i - g^{0i}(p_{\nu\alpha} p_\ell^\alpha) + p_\ell^0 p_\nu^i) - 8i p_{\nu\alpha} p_{\ell\beta} \epsilon^{0\alpha i\beta} \quad (2.87)$$

$$= 8(p_\ell^0 p_\ell^i - p_\ell^0 p_\ell^i) - 8i p_{\nu\alpha} p_{\ell\beta} \epsilon^{0\alpha i\beta} \quad (2.88)$$

$$= -8i p_{\nu\alpha} p_{\ell\beta} \epsilon^{0\alpha i\beta} \quad (2.89)$$

$$= -8i(p_{\nu j} p_{\ell k} - p_{\nu k} p_{\ell j}) \quad (2.90)$$

$$= -8i\left(-\frac{q^2}{4} + \frac{q^2}{4}\right) \quad (2.91)$$

$$= 0. \quad (2.92)$$

From equation 2.89 to equation 2.90 I used that for any given i the $\epsilon^{0\alpha i\beta}$ has only two non-zero components, ϵ^{0jik} and ϵ^{0kij} , with $k \neq i \neq j$. Since they differ by a single permutation, they have opposite signs. Without loss of generality let j have a value such that $\epsilon^{0jik} = 1$, then $\epsilon^{0kij} = -1$.

With the non-spatial components all zero, I restrict the further calculation to the spatial part of the leptonic matrix which I will denote as \hat{L}^{ij} . Consequently, only the spatial components of the hadronic matrix will have impact on the product in the W -frame. \hat{L}^{ij} can be simplified to

$$\hat{L}^{ij} = 8(\hat{p}_\nu^i \hat{p}_\ell^j - g^{ij}(\hat{p}_{\nu\alpha} \hat{p}_\ell^\alpha) + \hat{p}_\ell^i \hat{p}_\nu^j) - 8i \hat{p}_{\nu\alpha} \hat{p}_{\ell\beta} \epsilon^{i\alpha j\beta} \quad (2.93)$$

$$= 8\left(-\frac{q^2}{4} \hat{e}^i \hat{e}^j + \delta^{ij} \frac{q^2}{2} - \frac{q^2}{4} \hat{e}^i \hat{e}^j\right) + 8i 2 \hat{p}_{\nu i} \hat{p}_{\ell j} \epsilon^{ijk} \quad (2.94)$$

$$= 8\left(\delta^{ij} \frac{q^2}{2} - \frac{q^2}{2} \hat{e}^i \hat{e}^j\right) - 8i \frac{q^2}{2} \hat{e}^i \hat{e}^j \epsilon^{ijk} \quad (2.95)$$

$$= 4q^2(\delta^{ij} - \hat{e}^i \hat{e}^j - i \hat{e}^i \hat{e}^j \epsilon^{ijk}). \quad (2.96)$$

2.2. The Description of the Decay $B \rightarrow D\ell\nu_\ell$

From equation 2.93 to equation 2.94 I introduced \hat{e}^i , the unit vector of the lepton direction. I also reduced the dimension of the Levi-Civita tensor with the following argument:

$$\hat{p}_{\nu\alpha}\hat{p}_{\ell\beta}\epsilon^{i\alpha j\beta} = \hat{p}_{\nu 0}\hat{p}_{\ell k}\epsilon^{i0jk} + \hat{p}_{\nu k}\hat{p}_{\ell 0}\epsilon^{ikj0} \quad (2.97)$$

$$= \hat{p}_{\ell 0}\hat{p}_{\ell k}\epsilon^{i0jk} - \hat{p}_{\ell k}\hat{p}_{\ell 0}\epsilon^{ikj0} \quad (2.98)$$

$$= \hat{p}_{\ell 0}\hat{p}_{\ell k}\epsilon^{i0jk} + \hat{p}_{\ell k}\hat{p}_{\ell 0}\epsilon^{i0jk} \quad (2.99)$$

$$= 2\hat{p}_{\ell 0}\hat{p}_{\ell k}\epsilon^{i0jk} \quad (2.100)$$

$$= -2\hat{p}_{\ell 0}\hat{p}_{\ell k}\epsilon^{0ijk}, \quad (2.101)$$

where I used that since i and j are not zero, either α or β has to be zero in order to give non-vanishing factors. This again results in exactly two components.

The Hadronic Matrix For a given q^2 the hadronic current can be constructed from the available four-vectors. Since B and D are pseudoscalars, there are no polarization vectors and there are thus only two independent 4-vectors for which usually $p_B^\mu + p_D^\mu$ and $p_B^\mu - p_D^\mu = q^\mu$ are taken. The dependence on q^2 can then be encapsulated into two form factors:

$$H_\mu = \langle D | \bar{c}\gamma_\mu(1 - \gamma_5)b | B \rangle = F_+(q^2)(p_{B\mu} + p_{D\mu}) + F_-(q^2)q_\mu. \quad (2.102)$$

Of those two form factors only F_+ contributes to the differential decay width since

$$L^\mu q_\mu = 0. \quad (2.103)$$

This can most easily be seen in the W -frame where L^μ has only a spatial component and q_μ has only an energy component since the W is at rest. This argument of course only holds for negligible lepton masses and thus can only be applied to the light leptons. For the differential decay width of $B \rightarrow D\ell\nu_\ell$ the hadronic current thus reduces to

$$H_\mu = F_+(q^2)(p_{B\mu} + p_{D\mu}). \quad (2.104)$$

I will again switch to the W -frame, where as just discussed only the spatial components contribute. I therefore reduce the treatment to \hat{H} :

$$\hat{H} = F_+(q^2)(\hat{p}_B + \hat{p}_D) \quad (2.105)$$

$$= 2F_+(q^2)\hat{p}_D \quad (2.106)$$

$$= -2F_+(q^2)|\hat{p}_D|\hat{e}_z. \quad (2.107)$$

Here, \hat{e}_z is the unit vector in z -direction. Switching from the D momentum in the B -frame to the one in the W -frame will be useful later. Using equation 2.66 yields

$$\hat{H} = -2F_+(q^2)\frac{m_B}{q}|\tilde{p}_D|\hat{e}_z. \quad (2.108)$$

2. Theory

Product of Leptonic and Hadronic Matrices Inserting equations 2.108 and 2.96 into equation 2.67 results in:

$$|\mathcal{M}|^2 = \frac{G_F^2 |V_{cb}|^2}{2} 4q^2 (\delta^{ij} - \hat{e}^i \hat{e}^j - i \hat{e}^i \hat{e}^j \epsilon^{ijk}) 4F_+^2(q^2) \frac{m_B^2}{q^2} |\tilde{p}_D|^2 \hat{e}_{zi} \hat{e}_{zj} \quad (2.109)$$

$$= 8G_F^2 |V_{cb}|^2 F_+^2(q^2) m_B^2 |\tilde{p}_D|^2 (\delta^{ij} - \hat{e}^i \hat{e}^j - i \hat{e}^i \hat{e}^j \epsilon^{ijk}) \hat{e}_{zi} \hat{e}_{zj} \quad (2.110)$$

$$= 8G_F^2 |V_{cb}|^2 F_+^2(q^2) m_B^2 |\tilde{p}_D|^2 (1 - \cos^2 \hat{\theta}_\ell) \quad (2.111)$$

$$= 8G_F^2 |V_{cb}|^2 F_+^2(q^2) m_B^2 |\tilde{p}_D|^2 \sin^2 \hat{\theta}_\ell. \quad (2.112)$$

Here, I used that \hat{e}^i is in the yz plane and $\hat{e}^i \hat{e}^j \epsilon^{ijk}$ thus points into x direction and is therefore perpendicular to \hat{e}_{zi} .

2.2.1.4. Phase Space

The Lorentz invariant phase space from Fermi's golden rule is defined as

$$d\Pi_3 = (2\pi)^4 \delta^4(p_B^\mu - p_D^\mu - p_\ell^\mu - p_\nu^\mu) \frac{d\vec{p}_D}{(2\pi)^3 2E_D} \frac{d\vec{p}_\ell}{(2\pi)^3 2E_\ell} \frac{d\vec{p}_\nu}{(2\pi)^3 2E_\nu}. \quad (2.113)$$

And thus

$$\int d\Pi_3 = \frac{1}{(2\pi)^5} \int \frac{d\vec{p}_D}{(2\pi)^3 2E_D} \int \frac{d\vec{p}_\ell}{(2\pi)^3 2E_\ell} \int \frac{d\vec{p}_\nu}{(2\pi)^3 2E_\nu} \delta^4(p_B^\mu - p_D^\mu - p_\ell^\mu - p_\nu^\mu). \quad (2.114)$$

I derive the following identity with the usual $q^\mu = p_\ell^\mu + p_\nu^\mu$:

$$\int dq^2 \int \frac{d\vec{q}}{2E_q} \delta^4(q^\mu - p_\ell^\mu - p_\nu^\mu) = \int dq^2 \frac{1}{2E_q} \delta(E_q - (E_\ell + E_\nu)) \quad (2.115)$$

$$= \int dE_q \delta(E_q - (E_\ell + E_\nu)) \quad (2.116)$$

$$= 1. \quad (2.117)$$

Here, I used $dq^2 = 2E_q dE_q$. Inserting this identity into equation 2.114 and using $q^\mu = p_\ell^\mu + p_\nu^\mu = p_B^\mu - p_D^\mu$ yields

$$\int d\Pi_3 = \frac{1}{(2\pi)^5} \int dq^2 \frac{d\vec{q}}{2E_q} \int \frac{d\vec{p}_D}{2E_D} \int \frac{d\vec{p}_\ell}{2E_\ell} \int \frac{d\vec{p}_\nu}{2E_\nu} \delta^4(p_B^\mu - p_D^\mu - q^\mu) \delta^4(q^\mu - p_\ell^\mu - p_\nu^\mu) \quad (2.118)$$

$$= \frac{1}{2\pi} \int dq^2 (2\pi)^4 \int \frac{d\vec{q}}{(2\pi)^3 2E_q} \int \frac{d\vec{p}_D}{(2\pi)^3 2E_D} \delta^4(p_B^\mu - p_D^\mu - q^\mu) \int \frac{d\vec{p}_\ell}{(2\pi)^3 2E_\ell} \int \frac{d\vec{p}_\nu}{(2\pi)^3 2E_\nu} \delta^4(q^\mu - p_\ell^\mu - p_\nu^\mu) \quad (2.119)$$

$$= \frac{1}{2\pi} \int dq^2 \int d\Pi_2(B, D, q) \int d\Pi_2(q, \ell, \nu). \quad (2.120)$$

The problem thus reduces to the LIPS integral of two separate two-body decays. The evaluation of this quantity can be found *e.g.* in the review ‘‘Kinematics’’ of reference [13]:

$$d\Pi_2 = \frac{1}{(4\pi)^2} \frac{|\vec{p}_1|}{M} d\Omega_1. \quad (2.121)$$

Here, \vec{p}_1 and Ω_1 are the momentum and solid angle of the first decay particle in the reference frame of the mother particle. The mass of the mother particle is denoted with M . Without the integral sign this results in

$$d\Pi_3 = \frac{1}{2\pi} \frac{1}{(4\pi)^2} \frac{|\vec{p}_D|}{m_B} \frac{1}{(4\pi)^2} \frac{|\hat{p}_\ell|}{q} dq^2 d\tilde{\Omega}_D d\hat{\Omega}_\ell \quad (2.122)$$

$$= \frac{1}{(4\pi)^5} \frac{|\vec{p}_D|}{m_B} dq^2 d\tilde{\Omega}_D d\hat{\Omega}_\ell. \quad (2.123)$$

Here, I used $|\hat{p}_\ell| = q/2$.

2.2.1.5. Combining Phase Space and the Matrix Element

Putting the results together yields

$$d\Gamma = \frac{1}{2m_B} |\mathcal{M}|^2 d\Pi_3 \quad (2.124)$$

$$= \frac{1}{2m_B^2} |\mathcal{M}|^2 \frac{|\vec{p}_D|}{(4\pi)^5} dq^2 d\tilde{\Omega}_D d\hat{\Omega}_\ell \quad (2.125)$$

$$= \frac{4}{m_B^2} G_F^2 |V_{cb}|^2 F_+^2(q^2) m_B^2 \sin^2 \hat{\theta}_\ell \frac{|\vec{p}_D|^3}{(4\pi)^5} dq^2 d\tilde{\Omega}_D d\hat{\Omega}_\ell \quad (2.126)$$

$$= \frac{4}{m_B^2} G_F^2 |V_{cb}|^2 F_+^2(q^2) m_B^2 \sin^2 \hat{\theta}_\ell \frac{|\vec{p}_D|^3}{(4\pi)^4} dq^2 d\hat{\Omega}_\ell \quad (2.127)$$

$$= \frac{4}{m_B^2} G_F^2 |V_{cb}|^2 F_+^2(q^2) m_B^2 \frac{8\pi}{3} \frac{|\vec{p}_D|^3}{(4\pi)^4} dq^2. \quad (2.128)$$

Thus I arrive at the differential decay width in dependence of q^2

$$\frac{d\Gamma}{dq^2} = \frac{G_F^2 |V_{cb}|^2}{24\pi^3} |\vec{p}_D|^3 F_+^2(q^2). \quad (2.129)$$

2.2.1.6. From q^2 to w

Equation 2.129 can already be found in some of the literature, but a more common form uses w and a different form factor \mathcal{G} . The definition of w is

$$w = v_{B\mu} v_D^\mu. \quad (2.130)$$

2. Theory

Using

$$q^2 = (p_B^\mu - p_D^\mu)^2 = m_B^2 + m_D^2 - 2p_B^\mu p_{D\mu} \quad (2.131)$$

$$p_B^\mu p_{D\mu} = \frac{m_B^2 + m_D^2 - q^2}{2}, \quad (2.132)$$

one can write w as

$$w = \frac{p_B^\mu p_{D\mu}}{m_B m_D} = \frac{m_B^2 + m_D^2 - q^2}{2m_B m_D}. \quad (2.133)$$

I can now rewrite the differential width in terms of w :

$$dw = \frac{-dq^2}{2m_B m_D} \quad (2.134)$$

$$\frac{d\Gamma}{dw} = 2m_B m_D \frac{d\Gamma}{dq^2} \quad (2.135)$$

$$= \frac{G_F^2 |V_{cb}|^2}{12\pi^3} m_B m_D |\tilde{p}_D|^3 F_+(w)^2. \quad (2.136)$$

Note that the minus sign from the transformation is dropped since I also reverse the future integration order of w so that I can integrate from low w values to higher ones. I now need to evaluate $|\tilde{p}_D|^3$ in dependence of w .

$$|\tilde{p}_D|^3 = \left(\frac{(m_B^2 + m_D^2 - q^2)^2}{4m_B^2} - m_D^2 \right)^{\frac{3}{2}} \quad (2.137)$$

$$= \left(\frac{(2m_B m_D w)^2}{4m_B^2} - m_D^2 \right)^{\frac{3}{2}} \quad (2.138)$$

$$= (m_D^2 w^2 - m_D^2)^{\frac{3}{2}} \quad (2.139)$$

$$= m_D^3 (w^2 - 1)^{\frac{3}{2}}. \quad (2.140)$$

Inserting this into the differential decay width

$$\frac{d\Gamma}{dw} = \frac{G_F^2 |V_{cb}|^2}{12\pi^3} m_B m_D^4 (w^2 - 1)^{\frac{3}{2}} F_+(w)^2, \quad (2.141)$$

and switching to the form factor $\mathcal{G}(w)$ which is defined as

$$F_+(w)^2 = \frac{\left(1 + \frac{m_D}{m_B}\right)^2}{4 \frac{m_D}{m_B}} \mathcal{G}(w)^2, \quad (2.142)$$

results in the formula typically found in the literature

$$\frac{d\Gamma}{dw} = \frac{G_F^2 m_D^3}{48\pi^3} (m_B + m_D)^2 (w^2 - 1)^{3/2} \eta_{EW}^2 |V_{cb}|^2 \mathcal{G}(w)^2. \quad (2.143)$$

I also included the electroweak correction factor (η_{EW}) which I will discuss in section 2.2.4.

2.2.2. Heavy Quark Effective Theory

Before introducing the form-factor parameterizations used in this analysis I need to mention Heavy Quark Effective Theory (HQET) which is a constraint for one of the parameterizations. The hadrons involved in the decay $B \rightarrow D\ell\nu_\ell$ represent a special situation insofar that both the B and the D meson consist of two quarks where one is much heavier (b, c) than the other (u, d). The scale of QCD denoted by $\Lambda_{\text{QCD}} \sim 200 \text{ MeV}$ governs in which momentum transfer region coupling is large ($\ll 200 \text{ MeV}$) or small ($\gg 200 \text{ MeV}$). In a bound state the velocity of the heavy quark (here denoted as Q) will then be in the order of:

$$|\vec{v}_Q| = \frac{|\vec{p}_Q|}{m_Q} \sim \frac{\Lambda_{\text{QCD}}}{m_Q}. \quad (2.144)$$

If the heavy quark had an infinite mass it would thus sit still in the center of mass frame of the meson and behave like a static color field. The magnetic color moment is proportional to $1/m_Q$ and would thus decouple from the dynamics in this limit. Further, if both the b and c quark were such infinitely heavy quarks, replacing the b quark with a c quark would have no impact on the QCD interaction as long as they both have the same velocity. This is called “heavy quark symmetry”.

Of course this limit is violated by both b and c quarks having high (relative to Λ_{QCD}) but finite masses. The idea behind HQET is then to use heavy quark symmetry as a starting point and to make an expansion in E/m_Q , where E denotes the studied energy. Heavy quark symmetry is the leading order contribution to this expansion. Working close to the heavy quark symmetry, HQET usually uses the velocities rather than the momenta of the quarks to describe the system and thus w is often preferred over q^2 .

The kinematic situation where there is no velocity change between the b and c quark and thus between the B and D meson is called “zero recoil”, as the the D meson does not recoil from the B meson. The large overlap of initial and final state leads to the form factor being highest at this kinematic point. It is also at this point that the theoretical description of the form factor via LQCD is most precise. For this reason LQCD measurements were only available at zero recoil for a long time until with the improvements in lattice simulation recent studies now include additional kinematic points. Note that at zero recoil $w = w_{\text{min}} = 1$ and $q^2 = q_{\text{max}}^2 = (m_B - m_D)^2 \approx 11.63 \text{ GeV}^2$. The opposite kinematic point is called maximum recoil and corresponds to $w = w_{\text{max}} \approx 1.6$ and $q^2 = q_{\text{min}}^2 \approx 0 \text{ GeV}^2$.

2.2.3. Form Factor Parameterization

Although the form factor is maximum at zero recoil, one can see from equation 2.29 that zero recoil is also the point where $B \rightarrow D\ell\nu_\ell$ is most suppressed kinematically and thus experimentally the smallest amount of events is available there. To successfully combine LQCD data which are usually either at zero recoil or in its close vicinity, and experimental data which range over the whole kinematic region, it is necessary to find a common parametrization of the form factor which can be used for a combined fit.

I will introduce two different parameterizations here, the Boyd Grinstein Lebed (BGL) parametrization [14] and the Caprini Lellouch Neubert (CLN) parameterization [15]. BGL is the more general one. It is model independent, while CLN adds model dependent HQET constraints. Historically, CLN was widely used in $|V_{cb}|$ measurements because its additional constraints result in only two free parameters in the form-factor parameterization. With recent improvements on both the theoretical and experimental side, enough data is available to utilize the model-independent approach with more free parameters. Further, the precision of $|V_{cb}|$ has meanwhile reached a level where the systematic error CLN introduces (estimated to be $< 2\%$) stops being negligible.

Both parameterizations revolve around the so-called z -expansion, where z is defined as

$$z(w) = \frac{\sqrt{w+1} - \sqrt{2}}{\sqrt{w+1} + \sqrt{2}}. \quad (2.145)$$

Mapping to z has the effect that all physical values of the form factor lie on the real axis between zero and one (for $B \rightarrow D\ell\nu_\ell$ only between 0 and ≈ 0.06). Poles in the form factor which can arise from resonant states appear on the negative real axis and on the unit circle. One can then introduce so-called ‘‘Blaschke factors’’ to cancel poles and make a Taylor expansion in z :

$$f_i(z) = \frac{1}{P_i(z)\phi_i(z)} \sum_{n=0}^N a_{i,n} z^n, \quad i = +, 0. \quad (2.146)$$

This is already the BGL parameterization. $P_i(z)$ are the Blaschke factors containing the explicit poles (*e.g.* the B_c or B_c^* poles) in q^2 and $\phi_i(z)$ are the ‘‘outer functions,’’ which are arbitrary but required to be analytic without any poles or branch cuts. The $a_{i,n}$ are free parameters and N is the order at which the series is truncated. The index i denotes the type of form factor, where f_+ and f_0 are defined as

$$\langle D|\bar{c}\gamma_\mu(1 - \gamma_5)b|B\rangle = f_+(q^2) \left[(p_B + p_D)_\mu - \frac{M_B^2 - M_D^2}{q^2} q_\mu \right] + f_0(q^2) \frac{M_B^2 - M_D^2}{q^2} q_\mu. \quad (2.147)$$

Comparing these to the definitions of F_+ and F_- I made in equation 2.102 there are two things to notice²². First, the f_+ term has an additional dependence on q_μ . However, this term does not contribute to the decay width in the limit of zero lepton mass. Second, the F_- form factor is replaced with the f_0 form factor which differs by the factor $(M_B^2 - M_D^2)/q^2$ from F_- .

Following reference [16], I choose²³ $P_i(z) = 1$ and the outer functions as

$$\phi_+(z) = 1.1213(1+z)^2(1-z)^{1/2}[(1+r)(1-z) + 2\sqrt{r}(1+z)]^{-5} \quad (2.148)$$

$$\phi_0(z) = 0.5299(1+z)(1-z)^{3/2}[(1+r)(1-z) + 2\sqrt{r}(1+z)]^{-4}. \quad (2.149)$$

Here, r denotes the ratio of the D and B meson mass $r = m_D/m_B$. This choice of outer functions is based on the ones by Boyd, Grinstein and Lebed in reference [14] and results in a unitarity inequality of the simple form

$$\sum_{n=0}^N |a_{i,n}|^2 \leq 1, \quad (2.150)$$

for any order N .

The CLN parametrization adds further constraints from Heavy Quark symmetry (corrected in leading order) to reduce the number of free parameters:

$$\mathcal{G}(z) = \mathcal{G}(1)(1 - 8\rho^2 z + (51\rho^2 - 10)z^2 - (252\rho^2 - 84)z^3). \quad (2.151)$$

Note that CLN is typically given for $\mathcal{G}(w)$, while BGL uses f_+ . One of the advantages of the CLN parametrization is that it contains only two free parameters. $\mathcal{G}(1)$ is the form factor at zero recoil and can be determined in lattice QCD. This makes the separate treatment of experiment and theory especially easy since one only needs to fit the product $\eta_{\text{EW}}\mathcal{G}(1)|V_{cb}|$ and the form factor slope ρ^2 on the experimental side, and can later divide by $\mathcal{G}(1)$ as determined by LQCD.

For the BGL parameterization on the other hand, the best approach is a combined fit of both LQCD and experimental data with the $a_{i,n}$ as free parameters. One slight advantage of BGL is that the parametrized f_0 can be included into the fit (if LQCD data for f_0 is available) since f_0 and f_+ can be related by a kinematic constraint:

$$f_0(w_{\text{max}}) = f_+(w_{\text{max}}). \quad (2.152)$$

This constraint follows from the poles in equation 2.147 for $q^2 = 0$ (*i.e.* for $w = w_{\text{max}}$). In order for the poles to cancel, the kinematic constraint has to be true.

²²There exists a multitude of possible form factor definitions depending on what constants one chooses to be contained within the form factors and on what pair of 4-vectors is used as base. In the literature these form factors are further often denoted with varying letters (often f , h , F or G) and subscripts (usually 0, 1, + and -) which are not necessarily consistent across different authors. In this thesis I use the F_+ and F_- form factors as defined in equation 2.102, the form factor \mathcal{G} as defined in equation 2.142 and the form factors f_+ and f_0 as used by FNAL/MILC in reference [16].

²³It was verified in [16] that the omittance of poles has no relevant impact on the fits of $B \rightarrow D\ell\nu_\ell$.

2.2.4. Electroweak Correction Factor

My initial derivation of the differential decay width started with the assumption that there is no further interaction between the leptonic and hadronic current. While this is true on the tree level decay description, higher orders can add terms with photons, W^\pm , Z^0 or the Higgs boson. The highest impact in the leading order comes from the electromagnetic interactions depicted in Figure 2.6, so-called radiative corrections. Calculating those contributions not only involves higher order terms, it also involves contributions from all three sectors of the Standard Model and is thus quite complex. Therefore I will only present the result of such calculations here. The derivation can be found in reference [17].

In the limit of high Z boson mass, the contributing terms in first order lead to a correction of the Matrix element \mathcal{M} of

$$|\mathcal{M}_{\text{corr}}|^2 = |\mathcal{M}|^2 \left(1 + \frac{\alpha}{\pi} \ln\left(\frac{m_Z}{\mu}\right) \right) = |\mathcal{M}|^2 \eta_{\text{EW}}. \quad (2.153)$$

Here, α is the fine-structure constant

$$\alpha = \frac{e^2}{4\pi}, \quad (2.154)$$

m_Z is the mass of the Z boson and μ is the mass scale characterizing the process at hand. Finally, η_{EW} is the electroweak correction factor which I already introduced in equation 2.29. Using the mass of the B meson for the mass scale and varying it by a factor 2 to estimate the error of η_{EW} one gets:

$$\eta_{\text{EW}} = 1.0066 \pm 0.0016. \quad (2.155)$$

This value only depicts the leading order correction and is often termed as ‘‘Sirlin factor’’. The optimal way to calculate further electroweak contributions outside the Sirlin factor is currently an ongoing discussion within the CKM community and no final consensus has been found yet. For this reason I prefer to give my results including the electroweak correction factor. Ultimately a world average for $|V_{cb}|$ without η_{EW} has to be averaged from multiple experiments using one common electroweak correction method. This is for example done by the Heavy Flavor Averaging Group (HFAG) which in its next publication will include the $\eta_{\text{EW}}|V_{cb}|$ results from this thesis.

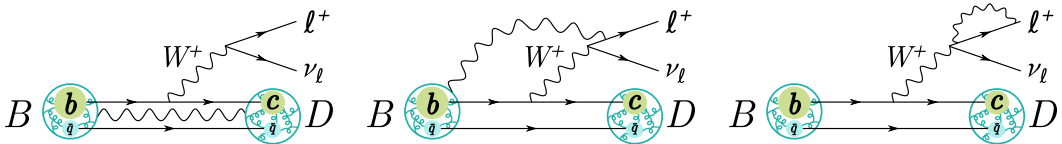


Figure 2.6.: Photonic terms contributing to the leading order electroweak correction.

3. Experimental Status of $|V_{cb}|$

In this chapter I outline the motivations for the common decays used in $|V_{cb}|$ measurements and their landscape together with the resulting average values. The $|V_{cb}|$ values measured in this analysis are excluded in this overview.

Although the CKM element V_{cb} affects every bottom to charm quark transition, only a subset is accessible to precise experimental measurements. In order to exclude contributions to the decay width from other quark transitions, tree-level decays are preferred for $|V_{cb}|$ measurements. B and B_s mesons offer the necessary b quark content. While B_s mesons have advantages in their theoretical description¹ they have the large drawback of not having a production channel comparable to $\Upsilon(4S) \rightarrow B\bar{B}$. For this reason B_s production plays a minor role at the B Factories². This is illustrated by the fact that Belle has only a data sample of 121 fb^{-1} at the $\Upsilon(5S)$ resonance – *i.e.* less than a fifth of the $\Upsilon(4S)$ sample – which via $\Upsilon(5S) \rightarrow B_{(s)}^{(*)}\bar{B}_{(s)}^{(*)}$ produces B_s mesons. BaBar has not produced B_s mesons at all.

There are then two categories of B decays involving b to c transitions: hadronic and semileptonic decays. In the hadronic decay mode the B meson decays into a meson containing a c quark and a second spectator meson, *i.e.* the W decays into hadronic products. While such modes can easily be reconstructed on the experimental side, the theoretical description is very hard due to the QCD interactions between the two resulting hadronic currents. Semileptonic decays on the other hand can reasonably well be modeled due to the factorization of leptonic and hadronic current (see section 2.2). The biggest experimental obstacle to semileptonic decays is the impossibility to directly measure the neutrino. This can be compensated by inferring it indirectly from 4-momentum conservation as is the case in this thesis (see chapter 6).

Semileptonic decays can be measured either in an inclusive decay mode $B \rightarrow X_c \ell \nu_\ell$, where X_c is a sum over all final states containing a charm quark within a given region of phase space, or from exclusive decays $B \rightarrow D^* \ell \nu_\ell$ or $B \rightarrow D \ell \nu_\ell$.

¹The higher mass of the s quark compared to light quarks reduces its kinematic components relative to sea quarks and gluons allowing for a more precise simulation in Lattice QCD.

²The same argument holds for baryonic states containing b quarks and neither BaBar nor Belle have energies high enough for their production. An example of a measurement with baryons at an experiment that is not at a B Factory is the recent study at LHCb [18] of Λ_b decays for the determination of $|V_{ub}|/|V_{cb}|$. However, since $|V_{ub}|$ has a much larger error than $|V_{cb}|$ this does not contribute to the determination of $|V_{cb}|$. Further studies of decays such as $\Lambda_b \rightarrow \Lambda_c \mu \nu_\mu$ for a direct $|V_{cb}|$ measurement at LHCb are currently ongoing efforts, but due to the complicated experimental situation precisions below those from semileptonic B decays are expected.

3. Experimental Status of $|V_{cb}|$

The decay $B \rightarrow D^* \ell \nu_\ell$ has been measured by Belle [19] and BaBar [20] and resulted in a determination of $\eta_{\text{EW}} \mathcal{F}(1) |V_{cb}|$ with a precision of about 3%, where $\mathcal{F}(1)$ is the normalization of the decay form factor similar to $\mathcal{G}(1)$ for $B \rightarrow D \ell \nu_\ell$. The current world average value obtained by the Heavy Flavour Averaging Group (HFAG) is [21]

$$\eta_{\text{EW}} \mathcal{F}(1) |V_{cb}|_{B \rightarrow D^* \ell \nu_\ell} = (35.81 \pm 0.11_{\text{stat}} \pm 0.44_{\text{syst}}) \times 10^{-3}. \quad (3.1)$$

The decay $B \rightarrow D \ell \nu_\ell$ has been measured in fully reconstructed events by BaBar [22], leading to a determination of $\eta_{\text{EW}} \mathcal{G}(1) |V_{cb}|$ with a precision of about 5%. Though still worse than $B \rightarrow D^* \ell \nu_\ell$ this is much better than the most precise Belle measurement of $B \rightarrow D \ell \nu_\ell$ prior to this analysis, which determined $\eta_{\text{EW}} \mathcal{G}(1) |V_{cb}|$ to the level of 17% [23]. A measurement of $B \rightarrow D \ell \nu_\ell$ with the full Belle data sample was thus highly motivated. For the world average of $\eta_{\text{EW}} \mathcal{G}(1) |V_{cb}|$ without the results from this analysis, HFAG obtained

$$\eta_{\text{EW}} \mathcal{G}(1) |V_{cb}|_{B \rightarrow D \ell \nu_\ell} = (42.65 \pm 0.72_{\text{stat}} \pm 1.35_{\text{syst}}) \times 10^{-3}. \quad (3.2)$$

Table 3.1 compares the resulting exclusive $|V_{cb}|$ values based on the mentioned world averages and using different form factor predictions ($\mathcal{F}(1)$ and $\mathcal{G}(1)$) by multiple Lattice QCD and Light Cone Sum Rule calculations. Here, the Sirlin factor of $\eta_{\text{EW}} = 1.00662$ was used.

$B \rightarrow D^* \ell \nu_\ell$		
Method	$\eta_{\text{EW}} \mathcal{F}(1)$	$ V_{cb} (10^{-3})$
Lattice QCD	0.912 ± 0.013 [24]	$39.27 \pm 0.50_{\text{exp}} \pm 0.56_{\text{th}}$
Sum rules	0.866 ± 0.020 [25]	$41.35 \pm 0.52_{\text{exp}} \pm 0.96_{\text{th}}$
$B \rightarrow D \ell \nu_\ell$		
Method	$\eta_{\text{EW}} \mathcal{G}(1)$	$ V_{cb} (10^{-3})$
Lattice QCD	1.0611 ± 0.0084 [16]	$40.19 \pm 1.44_{\text{exp}} \pm 0.32_{\text{th}}$
Lattice QCD	1.0418 ± 0.040 [26]	$40.94 \pm 1.47_{\text{exp}} \pm 1.57_{\text{th}}$
Sum rules	1.047 ± 0.020 [27]	$40.74 \pm 1.46_{\text{exp}} \pm 0.78_{\text{th}}$

Table 3.1.: Results for $|V_{cb}|$ from exclusive decays obtained using the HFAG averages [21] and different form factor normalizations.

This can be compared to $|V_{cb}|$ obtained from the inclusive decay $B \rightarrow X_c \ell \nu_\ell$ and theoretical expressions calculated using the Heavy Quark Expansion [28],

$$|V_{cb}|_{\text{inclusive}} = (42.42 \pm 0.86) \times 10^{-3}. \quad (3.3)$$

Assuming the most precise lattice QCD form factor measurements, there is thus a discrepancy of two to three standard deviations between $|V_{cb}|$ from $B \rightarrow D^* \ell \nu_\ell$ and inclusive decays. This difference can be due to underestimated experimental or theoretical systematics or shortcomings of the underlying models. Using $|V_{cb}|$ from $B \rightarrow D \ell \nu_\ell$ decays for the comparison yields a smaller difference ($\sim 1.3 \sigma$), but comes with high experimental errors. Improving this uncertainty and thus giving a better grasp on the inclusive-exclusive discrepancy is one of the main aims of this analysis.

4. The Belle Experiment

As discussed in section 2.1.3.1 the CKM mechanism predicted a third generation of quarks together with a CP violating phase. After first discoveries of CP violation (1964 indirectly with neutral kaon decays [29]) and the discovery of the b quark in 1977 [30] there was a great motivation in the 1980s to build experiments testing CP violation in B meson systems. From a multitude of proposals the two B Factories Belle and BaBar emerged. Their basic mode of operation was the same: using a high luminosity electron-positron synchrotron to produce B mesons via the $\Upsilon(4S)$ resonance.

Being energetically just above the rest mass of two B mesons, the $\Upsilon(4S)$ resonance predominantly ($> 96\%$ [13]) decays into a $B\bar{B}$ pair. As described in section 2.1.3.2 the measurement of CP violation with neutral B mesons requires measuring the time difference between two B decays. This can best be done at a collider by determining the difference in positions of the B decay vertices. This not only requires high vertexing capabilities of the detector, but also a high displacement between the two vertices. If the $\Upsilon(4S)$ resonance were created at rest in the lab frame, the two B mesons would decay almost at the same position making decay time measurements impossible. For this reason the colliding electron and positron beams at Belle (and BaBar) have asymmetric energies, thus adding a forward boost to the system in the lab frame. This results in the two B mesons moving forward after their creation. Different decay times of the two mesons then lead to a displacement of the vertices along the beam axis.

The measurement of CP violation in the B system at BaBar and Belle finally lead to the Nobel Prize for Kobayashi and Maskawa in 2008. Besides the measurement of CP violation, Belle achieved multiple other physics goals [31] such as the determination of different CKM matrix elements, searches for physics beyond the Standard Model in rare CKM suppressed decays or the measurement of CP violation in the D meson sector. Additional to studies at the $\Upsilon(4S)$ resonance Belle also operated at multiple other Υ resonances. In summary, Belle collected 5.7 fb^{-1} at $\Upsilon(1S)$, 24.9 fb^{-1} at $\Upsilon(2S)$, 2.9 fb^{-1} at $\Upsilon(3S)$, 711 fb^{-1} at $\Upsilon(4S)$, and 121.4 fb^{-1} at the $\Upsilon(5S)$ resonance. In this analysis solely the data sample at the $\Upsilon(4S)$ resonance is used.

The Belle experiment was located at the KEKB accelerator complex in Tsukuba, Japan and has been in operation from 1999 to 2010. At its peak about 500 scientists worked in the Belle collaboration and currently over 400 peer reviewed papers with physics results have been published by the collaboration. The great success of the experiment resulted in the currently ongoing construction of the improved Belle II experiment which aims at increasing the Belle luminosity by a factor of 50.

4.1. The KEKB Accelerator

A schematic of the KEKB electron-positron collider complex [32] can be seen in Figure 4.1. At the beginning of the chain, electrons and positrons are accelerated with a linear accelerator to 8 and 3.5 GeV respectively and inserted into the synchrotron. There are two synchrotron rings, each 3016 m long. The electron ring is operating at a higher energy and is thus called the high energy ring (HER), and the positron ring is named low energy ring (LER). The luminosity of these two beams reached a peak of $2.1 \times 10^{34} \text{ cm}^{-2}\text{s}^{-1}$. During this time each synchrotron typically contained 1584 bunches with an average spacing between the bunches of 1.84 m.

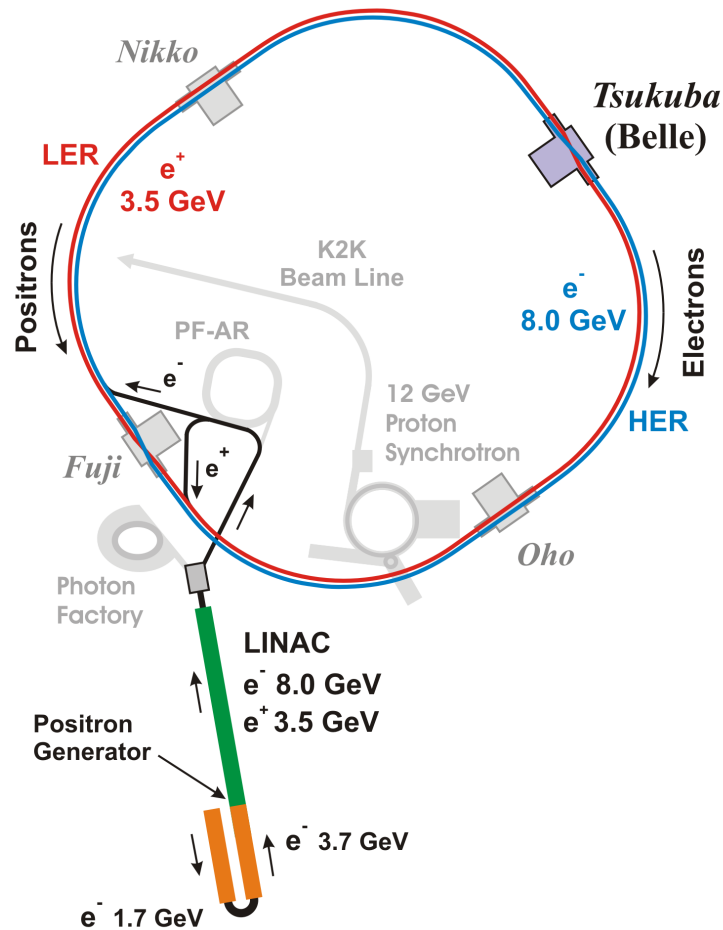


Figure 4.1.: The KEKB accelerator complex.

Both rings run in parallel and keep electrons and positrons at their insertion energies of 8 and 3.5 GeV. Since electron and positron beams are operated at different energies two separate synchrotron rings were required. The boost factor resulting from the energy asymmetry is $\beta\gamma \approx 0.425$, which corresponds to a typical flight length of the produced B mesons in the order of $200 \mu\text{m}$. There is a single interaction point (IP) located in the Tsukuba experiment hall where the two beams are crossing with an angle of $\pm 11 \text{ mrad}$. This is where the Belle detector is located and where the interactions are recorded.

The electron-positron beams at the IP define the coordinate system used in the Belle experiment:

- The z -axis is inverse to the direction of the positron beam. Note that this is not exactly equal to the electron direction due to the finite crossing angle of the beams.
- The x -axis lies in the plane of the synchrotron and points outwards.
- The y -axis then points upwards from the beam plane.
- The angle θ is defined as the angle w.r.t. the positive z -axis. Small θ values (*i.e.* close to the direction of the electron beam) are called the “forward region”, high θ values are called the “backward region”. In between (*i.e.* transversal to the beam) is the “barrel region”.
- The xy -plane is also denoted as $R\phi$ -plane, where R is the magnitude in the plane, and ϕ is the angle w.r.t. the positive x -axis.

4.2. The Belle Detector

The Belle Detector is a general-purpose detector with a primary aim on measuring the decay vertices of B meson pairs and high particle identification capabilities. Since the beam energies are asymmetric the detector maximizes efficiency by placing more instrumentation in the forward region, *e.g.* tracking and calorimetry is extended down to a smaller polar angle. The general configuration of the detector can be seen in Figure 4.2. I will introduce its components in the following sections.

4.2.1. The Interaction Region

The region surrounding the IP is called the interaction region. Electron and positron beams travel to the IP inside high vacuum beam pipes to reduce the possibility of interaction with atoms during their circulation. The pipes consist of double walled beryllium cylinders with an inner radius of 20 mm at the start of operations. During the upgrade 2003 the radius was reduced to 15 mm. In between the double walls (2.5 mm) liquid paraffin is used to cool the apparatus which is needed in order not to heat up detectors close to the beam pipe such as the Silicon Vertex Detector.

4. The Belle Experiment

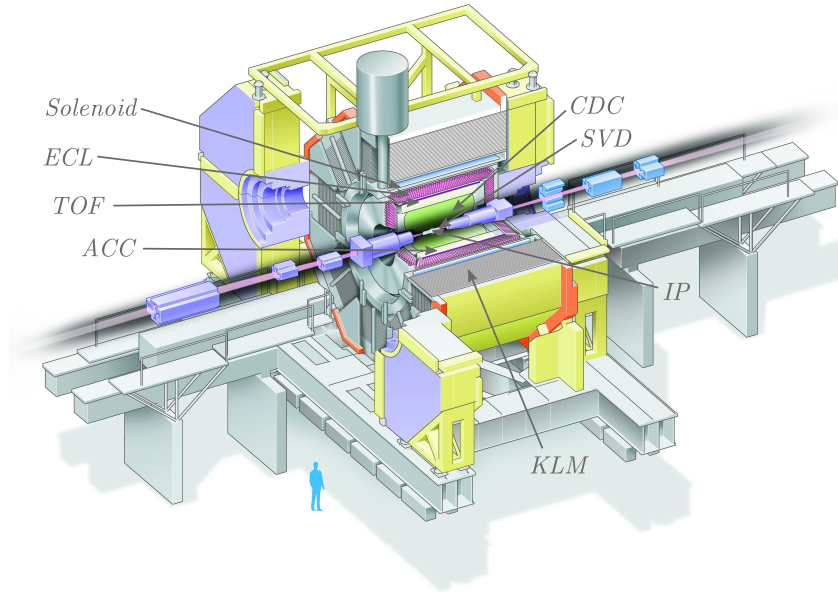


Figure 4.2.: The Belle detector. Source: [33], annotations by the author.

In order to reduce scattering of particles from the beam pipe and thus make vertexing more precise, it is important to reduce the thickness of the beam pipe as much as possible. The total material thickness of the beam pipe in the interaction region is thus designed to be only 0.3% of a radiation length.

At the IP the two beams meet at an angle of $\theta = 22$ mrad resulting in a center of mass energy of

$$\sqrt{s} = \sqrt{2E_{\text{HER}}E_{\text{LER}}(1 + \cos(\theta))} = 10.58 \text{ GeV}. \quad (4.1)$$

4.2.2. The Tracking System

The tracking system makes up the innermost part of the detector directly surrounding the beam pipe. Since the primary goal of Belle was measurement of CP violation in the B system via the displacement of neutral B vertices, the tracking system is required to have an excellent vertex resolution in the order of $100 \mu\text{m}$. The achieved resolutions in z -direction and the $R\phi$ -plane are

$$\sigma_z = 27.8 \oplus 31.9/p \mu\text{m} \quad (4.2)$$

$$\sigma_{R\phi} = 21.9 \oplus 35.5/p \mu\text{m}, \quad (4.3)$$

where p denotes the momentum in GeV and \oplus denotes quadratic addition.

Also, a high momentum resolution is important for particle type discrimination and kinematic reconstruction of decays. The achieved transversal momentum resolution is

$$\frac{\sigma_{p_T}}{p_T} = 0.0019p_T \oplus 0.0030/\beta, \quad (4.4)$$

where p_T is the transversal momentum in GeV.

The tracking system of Belle consists of a silicon vertex detector (SVD) close to the Interaction Point and a Central Drift Chamber (CDC) outside of the SVD. Both are fast electronic detectors and are situated inside a 1.5 T magnet. The produced magnetic field is homogeneous and parallel to the z -axis. It allows to determine the transversal momentum of charged particles via their radius on the spiral trajectories through the magnetic field.

4.2.2.1. The Silicon Vertex Detector

The innermost detector of Belle is the Silicon Vertex Detector (SVD). It is responsible for measuring the positions (so-called “hits”) of charged tracks close to the IP.

The SVD consists of double sided silicon strip detectors (DSSD). A silicon strip detector is made in its simplest form from a layer of doped silicon between a conducting plate on one side and conducting strips on the other side. A high voltage is applied between the strips and the backplate, so that when a charged particle causes electron-hole pairs in the silicon, the electrons and holes drift to opposite sides and a charge deposit can be measured on the strips. Between the strips a thin isolation ensures that the charge deposit stays local and can be used to determine the place where the charged particle intersected. A single strip detector allows only for a 2-dimensional measurement¹. Double sided strip detectors therefore also segment the backplate in the direction transversal to the other strip side. This results in a three-dimensional position measurement.

To ensure precise B meson vertex measurements, the SVD is placed right outside the beam pipe which also aids in τ and D meson vertex reconstruction. Since the particle energies at Belle are in the order of $O(1)$ GeV the dominant effect on vertex resolution comes from multiple scattering. To reduce this effect the SVD was built as thin as possible amounting to 1.94 radiation lengths, most of which is active detector material.

The SVD consists of 3 layers of DSSDs at 30 mm, 45.5 mm and 60.5 mm distance from the IP. Each layer is made from multiple rectangular ladders oriented in the z -direction and perpendicular to R . The ladders form a circle in the $R\phi$ -plane and are thus effectively cylinder-like structures. Going from the inside to the outside, the lengths of the ladders increase, resulting in a total angular coverage of $23^\circ < \theta < 140^\circ$. Note that this is a bit less than the full acceptance of the detector of $17^\circ < \theta < 150^\circ$.

¹Displacement along the strip direction can usually not be measured.

4. The Belle Experiment

In the summer of 2003 the SVD was upgraded to the so-called “SVD2”, the prior version now commonly denoted as “SVD1”. The SVD2 had four layers (at 20, 44, 70 and 88 mm) and an increased angular coverage of $17^\circ < \theta < 150^\circ$. All in all, 85 % of Belle data were taken using the SVD2.

4.2.2.2. The Central Drift Chamber

Outside the SVD the Central Drift Chamber (CDC) is placed. While the SVD is responsible for a good vertex resolution, it is the CDC that allows the reconstruction of the full particle trajectories. The hits from the SVD can then be assigned to these tracks after an inward extrapolation from the CDC. Extrapolating in the outward direction on the other hand allows to link a charged particle trajectory to a cluster measured in the electromagnetic calorimeter (see section 4.2.5).

The CDC is a so-called drift chamber filled with a mixture of 50% He and 50% C₂H₆ gas. Charged particles traversing the gas cause the creation of electrons and ions which then drift to charged wires running mostly in z -direction. The charge then moves through the wire to the end of the detector where it is measured. Since the current moves much faster through the wire than the electrons move through the gas, the timing of the measurement is mainly affected by the radial distance between a charge deposit and the wire. This can then be used to estimate the distance in which the charged particle traveled from the wire, *i.e.* a circle in the $R\phi$ -plane. Combining multiple such circles, the movement in the $R\phi$ -plane can be reconstructed. In order to obtain z coordinates so-called “stereo layers” are used in which the wires are tilted by a small amount. This shifts the measured signals in the $R\phi$ -plane depending on the θ angle of the track. The displacement can then be used in the track reconstruction algorithms to estimate the z positions of the trajectory.

The CDC contains 50 super-layers, each with three to six axial (in z -direction) or small angle stereo layers and three cathode layers which help to keep the electric potential. The CDC covers the angular range of $17^\circ < \theta < 150^\circ$ and is thus asymmetric like the rest of the detector. It starts right outside the SVD and ends at a distance of 880 mm from the beam axis.

The CDC contributes to particle identification via the energy loss (dE/dx) of charged tracks. The energy loss of a charged particles in a medium follows a characteristic curve depending on the particle type² as can be seen in Figure 4.3. For particles with low transverse momenta which do not reach the further particle identification detectors, the energy loss in the CDC is the only means of identification.

²Energy loss of charged particles via ionization and atomic excitation is described by the so-called Bethe-Bloch curve. Its shape in the Belle relevant momentum region can be seen for kaons, pions and protons in Figure 4.3. While the general shape is the same for different particles, the curves are displaced, *e.g.* the minimum can always be found at $\beta\gamma = p/m \approx 3.5$, which is shifted for different particle masses. Note that the Bethe-Bloch formula is only valid for heavy charged particles ($m > m_e$) and does not describe electrons which mainly lose their energy via bremsstrahlung.

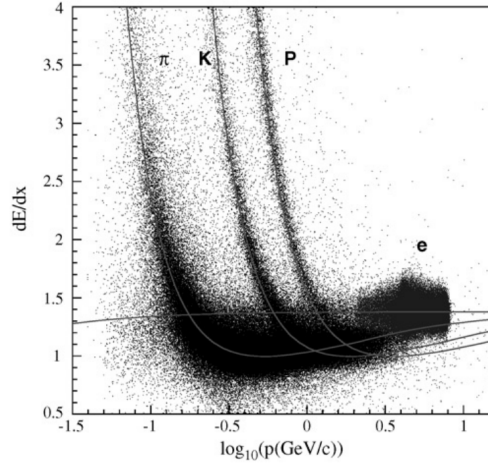


Figure 4.3.: Energy loss (dE/dx) dependence on momentum for kaons, pions, protons and electrons. Picture from reference [34].

4.2.3. The Aerogel Cherenkov Counter

Cherenkov detectors utilize materials in which charged particles move faster through the medium than light. This leads to polarizations in the material coherently summing up to a light wave, similar to a Mach-cone. The velocity necessary for the production of such a Cherenkov light needs to be

$$v \geq \frac{c}{n}, \quad (4.5)$$

with n being the refractive index and c the vacuum speed of light. *I.e.* the higher the refractive index of the material, the lower the speed of the particle can be to cause Cherenkov light.

In a Cherenkov counter this phenomenon is applied to distinguish between particles of similar momenta but different masses, hence different velocities. At Belle the Cherenkov counters are mainly used to discriminate between charged kaons and pions. Since pions are lighter, they have higher velocities for the same momentum. In a Cherenkov counter with suiting refractive index (for a specific momentum region) they produce Cherenkov light while kaons pass through without causing Cherenkov radiation.

The aerogel Cherenkov counter (ACC) at Belle consists of 960 counter modules in barrel and forward region ($33.3^\circ < \theta < 127.9^\circ$), each equipped with a photomultiplier tube for light detection. To achieve separation of pions and kaons at the typical Belle energies, refractive indices range between 1.01 and 1.03.

The material providing such low refractive indices chosen is silica aerogel. An aerogel is basically a gel (here silica-gel, *i.e.* a gel consisting of sodium silicate SiO_2) with a high amount of additional air in a porous structure. This results in a very light material with low density and small refractive indices.

4.2.4. The Time-Of-Flight Counter

A further sub-detector used for particle identification purposes is the time-of-flight counter (TOF). The basic principle of this detector is to measure the time when a charged particle passes through it in relation to the time of the collision. Combining the time of flight with the particle momentum measured by the CDC can be used to test different mass hypotheses for the particle.

The TOF is mounted in the the barrel region and is made up from 128 plastic scintillator counters which are positioned right between the ACC and the inner wall of the ECL at a distance of 1.2 m from the IP. Two counters each are grouped into a module (resulting in 64 modules) together with a trigger scintillation counter (TSC). The scintillators offer a resolution of ~ 100 ps, resulting in a good discrimination for particles below 1.2 GeV. This energy region covers $\sim 90\%$ of the charged final state particles at Belle's $\Upsilon(4S)$ resonance. The angular range covered by the TOF amounts to $33^\circ < \theta < 121^\circ$.

4.2.5. The Electromagnetic Calorimeter

The purpose of the electromagnetic calorimeter (ECL) is to measure the energy of photons, electrons and positrons. It surrounds the TOF in the barrel region and has forward and backward endcaps. The ECL utilizes scintillator crystals made from cesium iodide crystals doped with thallium CsI(Tl). The atoms of the crystals are easily excited by electromagnetic interactions and in the retransmission to their ground state emit a photon. These photons are then detected by photomultipliers attached to each crystal, converting them into a measurable electric signal.

For optimal detection the aim is to fully stop incoming light electromagnetic particles so that their full energy is deposited in the ECL. The energy deposit does not happen at once but rather an electromagnetic cascade is triggered, called an “electromagnetic shower”. In the shower, photons decay into electron-positron pairs, while electrons and positrons will experience bremsstrahlung effects and radiate off photons. In each occurrence of such a process the number of particles grows and the average energy is reduced until the entire shower is absorbed by the material. During this process the shower also spreads in the transverse direction allowing to measure a “shower shape”. Since the ECL has a thickness of 16 radiation lengths (for e^\pm and γ) almost the entire energy of an electromagnetic shower is contained. However, only electrons, positrons and photons have high enough electromagnetic cross sections to be stopped in the ECL. Neutral particles, hadrons and muons interact only in a minor fashion and usually pass through the ECL.

The Belle ECL consists of 8736 CsI(Tl) crystals covering an angular range of $17^\circ < \theta < 150^\circ$. The energy resolution is about 4% at 100 MeV and 1.6% at 8 GeV³.

³Note that this resolution is worse than the momentum resolution. This can be for example seen in the mass distribution of reconstructed D mesons in section 6.3.2 where channels with neutral pions (which decay into two photons that are only seen in the ECL) have the broadest peaks.

The ECL provides multiple important contributions to particle identification. First, if an ECL cluster is not matched by a charged track it can be attributed to a photon. Second, the deposited energy is used to determine the coefficient E/p of charged tracks, which can be used to distinguish electrons and positrons from hadrons which are not stopped in the ECL. Finally, the shower shape is also characteristic for electrons and positrons.

4.2.6. The K_L^0 and μ Detection System

Outside the calorimeter is the last sub-detector of Belle, the K_L^0 and μ detection system (KLM). Since it is located outside the calorimeter only muons and hadrons are able to reach it. It is positioned in the barrel and endcap regions covering an overall range of $20^\circ < \theta < 155^\circ$.

The KLM consists of alternating layers of iron plates and double-gap resistive plate counters. The iron plates serve two purposes. First, they make up an iron return yoke for the electromagnet. Second, they provide stopping material mainly for K_L^0 mesons summing up to 3.9 interaction lengths. This leads to the K_L^0 showering in the KLM which allows to determine their direction. However, this is not enough to contain the entire average shower and energy measurements of K_L^0 mesons are thus not possible.

Charged particles are detected in the resistive plate counters (RPC). These consist of two parallel electrodes made from glass with a high voltage difference of 8 kV and high resistance. The space between the plates is filled with gas which is ionized by the passing charged particles. The RPCs are operated in the so-called streamer mode which is at an electric potential above the avalanche mode adding the creation of a plasma “streamer” which causes local discharges on the plates. Pick-up wires then use capacitive coupling to measure the deposited charges. The high resistance of the plates limits the spread of the charges and improves spatial resolution.

4.2.7. Particle Identification

The number of particles stable enough to reach even the innermost tracking layers is rather small: electrons, muons, kaons (K^\pm , K_L^0 , K_S^0), pions (π^\pm , π^0), lambdas, protons, neutrons, photons and neutrinos. Every other particle decays before and has to be reconstructed from its decay products. K_S^0 mesons and lambdas live long enough to decay still within in the region of the tracking detector. They are identified by their characteristic decays $K_S^0 \rightarrow e^+e^-$ and $\Lambda^0 \rightarrow p^+\pi^-$. Neutrinos cannot be seen in the detector directly. This will play an important role in the reconstruction of the $B \rightarrow D\ell\nu_\ell$ decay. Photons are identified by their shower in the ECL without a matching charged particle track.

Electrons, muons, kaons, protons, and pions are identified via likelihood methods. For a given particle hypothesis multiple measured quantities are used to generate likelihoods which are then multiplied to generate an overall likelihood which can be used to test different particle hypotheses in relation to each other.

4. The Belle Experiment

To separate kaons and pions the likelihoods for the dE/dx measured in the CDC (L^{CDC}), for the time traveled between IP and TOF (L^{TOF}), and for the yields in the ACC (L^{ACC}) are determined and multiplied:

$$L = L^{CDC} \times L^{TOF} \times L^{ACC} \quad (4.6)$$

Calculating this likelihood once with the kaon hypothesis (L_K) and once with the pion hypothesis (L_π) one can define a likelihood ratio:

$$L(K : \pi) = \frac{L_K}{L_K + L_\pi}, \quad (4.7)$$

which ranges from zero to one. One represents a high probability of the particle being a kaon and zero being a pion.

To identify electrons (or positrons), likelihoods for the following five quantities are used [35]:

1. **Track-cluster matching:** The distance between the nearest extrapolated track and the ECL cluster position.
2. **E/p:** The ratio of the energy measured in the ECL over the momentum measured in the CDC.
3. **Shower shape:** The transversal shape of the shower in the ECL measured as the ratio of energy deposited in a 3×3 cell cluster ($E9$) and a 5×5 cell cluster ($E25$). Different shapes of $E9/E25$ can be seen for pions and electrons in Figure 4.4a.
4. **dE/dx in the CDC:** Energy loss of charged tracks in the CDC. See Figure 4.4b for the different distribution of electrons and pions.
5. **Light yield in the ACC:** The threshold for electron momenta to produce light in the ACC is in the order of a few MeV while pions need a few hundred MeV to be fast enough to cause Cherenkov light.

The overall likelihood for electron identification is then:

$$L_{\text{eid}} = \frac{\prod_{i=1}^n L_e^i}{\prod_{i=1}^n L_e^i + \prod_{i=1}^n L_{\bar{e}}^i} \quad (4.8)$$

where i runs over the five likelihood contributions and $L_{\bar{e}}$ denotes a likelihood for a non-electron particle hypothesis. Figure 4.5 shows the resulting L_{eid} distribution for electrons and pions.

Finally, muons are identified based on likelihoods [36] determined from the KLM system using the range of the muon candidate in the KLM (L^{range}) and the quality of a track fit in the KLM (L^{fit}). The overall muon likelihood is then:

$$L_{\mu\text{id}} = \frac{\prod_{i=1}^n L_\mu^i}{\prod_{i=1}^n L_\mu^i + \prod_{i=1}^n L_\pi^i + \prod_{i=1}^n L_K^i} \quad (4.9)$$

where i runs over the two likelihoods just mentioned. Note that no electron likelihoods appear in the denominator since electrons do not reach the KLM system.

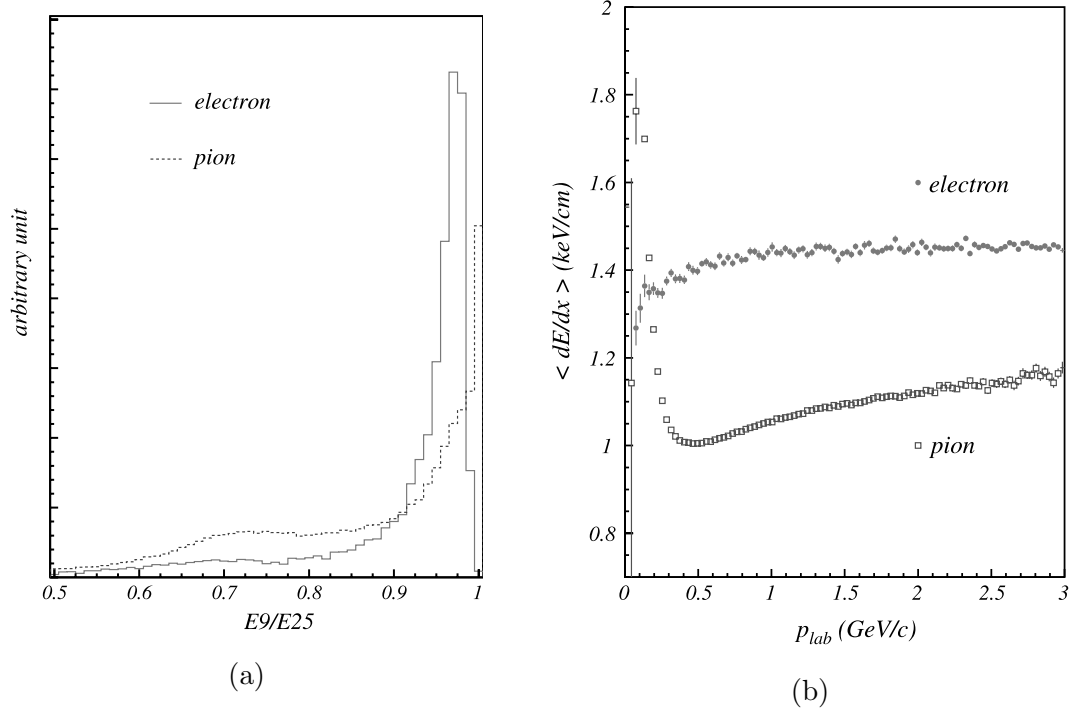


Figure 4.4.: Two important quantities for identifying electrons: the cluster shape in the ECL (a) and the momentum dependent energy loss in the CDC (b). Here shown in comparison to the same quantity for pions. Pictures from reference [34].

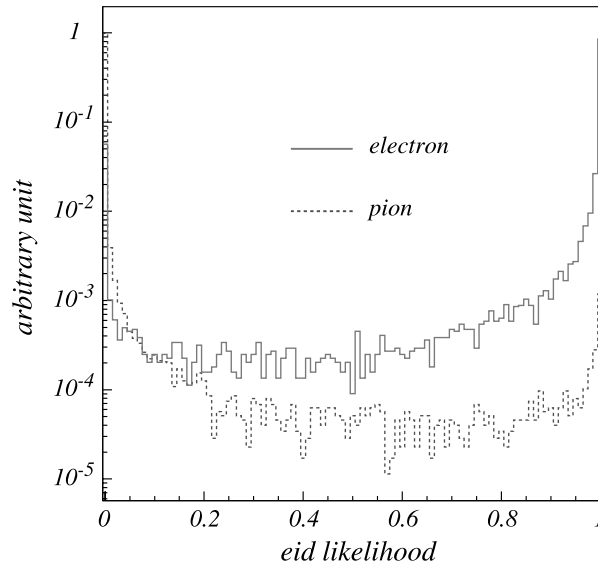


Figure 4.5.: Electron ID likelihood (L_{eid}) distribution for electrons and pions. Picture from reference [34].

5. Data Sample

This analysis is based on the entire Belle $\Upsilon(4S)$ data sample of 711 fb^{-1} . The Belle experiment was collecting data from June 1999 to June 2010 including regular shutdowns, *e.g.* for maintenance, hardware replacement and detector alignment. The periods between the shutdowns were labeled as **experiments**. Each **experiment** further consists of multiple **runs** which each last up to 8 hours and mark a continuous taking of data under the same responsible staff.

During data taking the events detected by the Belle detector were processed by an online hardware trigger ($O(1\text{kHz})$) looking for hadronic events (such as Υ events) by selecting events with either 3 or more charged tracks, high energy deposited in the ECL or four separate neutral clusters in the ECL. A further software trigger ($O(100\text{Hz})$) then removed events with charged tracks of low quality. Finally the reduced amount of data is saved to digital video tape for later offline data processing.

5.1. Offline Data Processing

The data recorded by the Belle experiment amounts to about one petabyte of disk space. This data was further processed offline with the **Belle Analysis Framework (BASF)** and stored in the so-called **Panther** format. **Panther** essentially consists of tables based on the entity-relationship model [37]. Typical **Panther** tables are for example tables of reconstructed photons, charged particles or $V0$ -type particles (K_S^0 , Λ). The entity-relationship model then allows to *e.g.* find the daughter particles from which a K_S^0 is assembled or to retrieve the ECL cluster associated with a photon. Other information stored in the tables includes energies and momenta. During the multiple reconstruction steps (*e.g.* skimming, tag side reconstruction) **Panther** tables are often modified, added or removed in order to keep exactly the amount of data needed in specific applications.

These procedures all happen within the Belle Analysis Framework, an object oriented C++ framework for data analysis. In **BASF** users write software modules implementing multiple callback methods which are then invoked by the framework during runtime. The modules are compiled to shared object libraries and dynamically loaded into **BASF** which is then invoked for a specified set of events. This procedure can be done in parallel processing allowing for a fast handling of a large number of events.

A typical callback method implemented by the user is for example the `event` function which is called by `BASF` for every single event. In this analysis, `event` is the place where the assembly of the $B \rightarrow D\ell\nu_\ell$ decay and the subsequent storage of the decay parameters happens. Other methods exist for the begin and end of runs or for the initial setup and final teardown.

The framework allows to store results from the process as additional panther tables or as `HBOOK` [38] n-tuples. The former is used by the tag reconstruction which I will describe in section 6.1. The modules written by the author for the signal side on the other hand generate output as `HBOOK` n-tuples which are later converted into `ROOT` [39] files for further analysis.

The data processing mentioned so far took all place at the computing facilities at KEK which offer a large amount of parallel processors in a queued environment. For example, the typical reconstruction of the decay $B \rightarrow D\ell\nu_\ell$ as described in section 6.3 took on average a day of processing utilizing over 200 processor cores in parallel.

5.2. MC Production

The real data recorded at Belle is accompanied with a simulated generic Monte Carlo (MC) sample five times the size of the real data sample. The content of the generic MC is grouped into five “MC streams” labeled with 0-4, each stream corresponding roughly to the amount of data in the real data sample.

Among many other possible decays, the $B \rightarrow D\ell\nu_\ell$ signal and its different background components discussed in this analysis are modeled in the generic MC. An additional $B \rightarrow X_u\ell\nu_\ell$ signal MC was added later to the MC streams to model the $B \rightarrow X_u\ell\nu_\ell$ decays missing in the original generic simulation.

Monte Carlo simulated data plays an important role in this analysis. First, it allows to optimize and study the entire procedure of the analysis before using real data and thus prevents bias. Second, MC can be used to study efficiencies and third, by varying the MC one can study multiple systematic error components and model their propagation through the analysis procedure.

The goal of the generic MC production is to simulate the entire experiment from the production of particles at the primary vertex to the detection in the different sub-detectors and the following reconstruction in `BASF`.

In the first step of the MC simulation a so-called event generator, `EvtGen` [40] simulates the decays at and shortly after the primary vertex. Different decay models are used with multiple input parameters such a branching ratios and decay constants. For example the decay $B \rightarrow D\ell\nu_\ell$ is simulated with the `HQET2` model of `EvtGen` which is based on the CLN form-factor parameterization. Thus ρ^2 is specified as input parameter along with the branching ratio. These automatically fix $|V_{cb}|$ in the generic MC. The `PHOTOS` package [41] is used to additionally take into account the possibility of bremsstrahlung by charged particles in this early stage of the event. The generator in principal only simulates the decay of short lived particles not reaching the area of the detector (*i.e.* inside the SVD).

5. Data Sample

In the next step the particle trajectories are extrapolated by **GEANT3** [42]. Interactions with the detector material (ionization, energy loss, multiple scattering etc.) are taken into account and further particle decays within the detector region are simulated. Detector responses are realistically estimated and data is taken in a fashion analogue to real data taking. The **Panther** tables resulting from this procedure closely mimic the tables from real data, but contain additional MC information which gives access to efficiency studies and similar purposes.

Since modern measurements are more recent than the Belle generic MC, it is important to correct its description before comparing it to real data. I will describe the corrections applied to the MC in chapter 8 and discuss the corresponding systematic errors in section 9.1.

6. Experimental Procedure

This chapter describes the experimental procedure starting from the recorded Belle data in the Panther tables up to the determination of the $B \rightarrow D\ell\nu_\ell$ differential decay widths. The interpretation and extraction of $|V_{cb}|$ will be discussed chapter 10.

6.1. Hadronic Tag

The “full reconstruction” in the title of this thesis specifies the process of reconstructing both B mesons from the $\Upsilon(4S) \rightarrow B\bar{B}$ decay, one B meson (B_{sig}) decaying into the signal decay mode ($B \rightarrow D\ell\nu_\ell$), and the second B meson (B_{tag}) decaying into a hadronic mode. This procedure is called hadronic tagging and allows the reconstruction of all involved particles in the analysis with the exception of the neutrino which is then constrained by 4-momentum conservation.

There are multiple benefits of hadronic tagging. First and most important, it reduces the combinatoric background to a very high degree¹. Second, the full reconstruction gives access to the missing 4-momentum of the event which for genuine events has an invariant mass of the missing neutrino, *i.e.* a value very close to zero. Finally, the full reconstruction also leads to a high precision of the measured decay kinematics.

Reconstruction of B mesons in hadronic modes is a very complex topic of its own due to the multitude of possible decay modes. In order to recover as many B mesons as possible, a high number of decay structures need to be taken into consideration. Since hadronic tagging is an often required procedure at Belle there exists a software package called `EKPFullrecon`² [43] designed for that task. The `EKPFullrecon` package searches 1104 different hadronic decay topologies and selects candidates using the NeuroBayes neural network framework [44]. The number 1104 is a result of the combinatorics of subsequent decays.

¹One might wonder why no hadronic tagging is used in $|V_{cb}|$ measurements with $B \rightarrow D^*\ell\nu_\ell$. The answer lies in the different kinematic situation. In the decay of D^* to a D meson and a pion, mass constraints lead to a very small available phase space. Combinatoric background is not restricted by this and varies over a much wider phase space region and can thus be well separated from the signal. Hadronic tagging is thus not necessary.

²Note that `EKPFullrecon` is a Belle-internal package name and in the cited article the software is only titled as “B-meson full reconstruction algorithm designed for the Belle experiment”.

6. Experimental Procedure

At the uppermost level charged B meson candidates are reconstructed from 17 different decays to $D^{*0}\pi^-$, $D^{*0}\pi^-\pi^0$, $D^{*0}\pi^-\pi^-\pi^+$, $D^0\pi^-$, $D^0\pi^-\pi^0$, $D^0\pi^-\pi^-\pi^+$, $D^{*0}D_s^{*-}$, $D^{*0}D_s^-$, $D^0D_s^{*-}$, $D^0D_s^-$, $J/\psi K^-$, $J/\psi K^-\pi^+\pi^-$, D^0K^- , $D^{*0}\pi^-\pi^-\pi^+\pi^0$, $D^+\pi^-\pi^-$, $J/\psi K^-\pi^0$, and $J/\psi K_S^0\pi^-$, and neutral B meson candidates are reconstructed from 15 decays to $D^{*+}\pi^-$, $D^{*+}\pi^-\pi^0$, $D^{*+}\pi^-\pi^+\pi^-$, $D^+\pi^-$, $D^+\pi^-\pi^+\pi^-$, $D^+\pi^-\pi^0$, $D^{*+}D_s^{*-}$, $D^{*+}D_s^-$, $D^+D_s^{*-}$, $D^+D_s^-$, $J/\psi K_S^0$, $J/\psi K^-\pi^+$, $J/\psi K_S^0\pi^+\pi^-$, $D^0\pi^0$, and $D^{*+}\pi^-\pi^-\pi^+\pi^0$. Note that charge conjugated decays are always implied. The further hadronic decays of D^{*0} , D^{*+} , D^0 , D^+ , D_s^{*+} and D_s^+ and the lepton-pair decays of the J/ψ then result in 1104 topologies in total.

The decay-chains are grouped into 4 separate stages, starting at the level of individual finale state particles measured as charged tracks or photons up to the top level of the B mesons. Figure 6.1 gives a schematic view of the categorization. In order to keep the combinatoric load within a feasible level, each stage is reconstructed and preselected by the neural network before the next stage is considered. At each stage a multivariate classifier o_{tag} is calculated representing the quality of the reconstruction. Values of o_{tag} range from 0 to 1 where 1 corresponds to signal-like candidates and 0 corresponds to background-like candidates. These values are then in turn used as input parameters for the next level of the reconstruction.

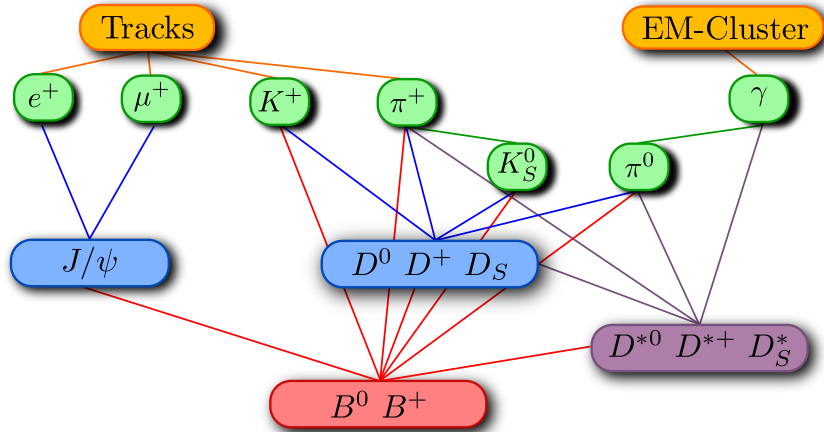


Figure 6.1.: The four layers of the hadronic tag reconstruction. Selection criteria are applied after each level. Lines indicate dependence on the output of prior levels. Image source: [43].

For every event, the package generates a list of charged and neutral B meson candidates, which each again have a multivariate classifier o_{tag} . Only candidates with $o_{\text{tag}} > 10^{-6}$ are retained and at most the best 3 charged and best 3 neutral ones are stored in a **Panther** table. Hadronic tagging is available for the entire Belle $\Upsilon(4S)$ data sample both for real data and the five MC streams used in this analysis.

6.2. Skim

To reduce the amount of available data which is in the order of one petabyte, a so-called skim is used. Skims are implemented as **BASF** modules which determine whether events fulfill certain requirements. Passing events are either stored in new **Panther** tables or as lists referencing indices in existing tables. By applying one or more skims, the amount of data can be thinned out until it is small enough to be feasible for repeated analysis.

In this analysis the so-called **xlnu-skim** was used on both real data and MC simulated events. Events fulfill the requirements of the skim if they contain at least one B_{tag} candidate and at least one charged lepton (electron or muon) satisfying:

- Impact parameters in $R\phi$ (Δr) and z (Δz): $\Delta r < 0.5$ cm and $\Delta z < 2$ cm,
- Belle electron likelihood (L_{eid}) greater than 0.5 or Belle muon likelihood ($L_{\mu\text{id}}$) greater than 0.9,
- Laboratory frame momentum greater than 0.3 GeV.

The efficiency of the **xlnu-skim** on real data is about 1.7% and reduces the amount of data to about 20 terabytes.

6.3. $B \rightarrow D\ell\nu_\ell$ Reconstruction

In the events remaining after the `xlnu-skim` the signal side B meson (B_{sig}) is reconstructed in the decay mode $B \rightarrow D\ell\nu_\ell$. In the following, I separate the data into 4 sub-samples according to the charge of B_{sig} ³ and the type of the charged signal side lepton giving the following 4 sub-samples: $B^0 \rightarrow D^- e^+ \nu_e$, $B^0 \rightarrow D^- \mu^+ \nu_\mu$, $B^+ \rightarrow \bar{D}^0 e^+ \nu_e$ and $B^+ \rightarrow \bar{D}^0 \mu^+ \nu_\mu$. The separation for B meson charge is motivated by different background shapes in the sub-samples. The separation in leptons is a useful cross-check, but also allows to test for lepton flavor violation. It further makes it possible to determine separate branching ratios of the decays. Note that the reconstruction of charge conjugated decays is again always implied.

6.3.1. Charged Lepton Reconstruction

I further tighten the requirements for charged lepton reconstruction applied in the `xlnu-skim` to:

- $p_e > 0.3$ GeV and $p_\mu > 0.6$ GeV, where p denotes the magnitude of the reconstructed 3-momentum in the laboratory frame,
- and $17^\circ < \theta_e < 150^\circ$ and $25^\circ < \theta_\mu < 145^\circ$, where θ is the polar angle of the particle in the laboratory frame with respect to the z -axis.

Both requirements arise from the momentum range and detector area in which electrons and muons can be reasonably reconstructed. See reference [35] for details on electron- and reference [36] for details on muon identification capabilities at Belle.

In events with an electron on the signal side, I attempt to recover bremsstrahlung by searching for a photon within a 5° cone around the electron direction. If such a photon is found, it is merged with the electron for the rest of this analysis. If more than one photon satisfies the criterion, the photon closest to the electron direction is chosen.

6.3.2. D Meson Reconstruction

The D meson decays dominantly into hadronic products. I reconstruct charged D mesons in 10 different hadronic channels and neutral D mesons in 13 hadronic channels. These channels and their branching fractions are listed in Table 6.1. In total, they constitute to 28.93% of the charged D meson width and to 40.09% of the neutral D meson width [13].

³The charge of B_{sig} determines automatically the charge of B_{tag} : either both are charged or both are neutral. Note that for charged B mesons an opposite charge can be assumed while for neutral B mesons this is not the case: due to possible B^0 - \bar{B}^0 mixing one can not infer that B_{sig} is the anti-particle of B_{tag} .

D decay	Branching ratio in % [13]
$D^+ \rightarrow K^- \pi^+ \pi^+$	0.0913 ± 0.0019
$D^+ \rightarrow K^- \pi^+ \pi^+ \pi^0$	0.0599 ± 0.0018
$D^+ \rightarrow K_S^0 \pi^+$	0.0147 ± 0.0007
$D^+ \rightarrow K_S^0 \pi^+ \pi^0$	0.0699 ± 0.0027
$D^+ \rightarrow K^+ K^- \pi^+$	0.0095 ± 0.0003
$D^+ \rightarrow K_S^0 K^+$	0.0028 ± 0.0002
$D^+ \rightarrow K_S^0 \pi^+ \pi^+ \pi^-$	0.0312 ± 0.0011
$D^+ \rightarrow \pi^+ \pi^0$	0.0012 ± 0.00006
$D^+ \rightarrow \pi^+ \pi^+ \pi^-$	0.0032 ± 0.0002
$D^+ \rightarrow K^- \pi^+ \pi^+ \pi^+ \pi^-$	0.0056 ± 0.0005
$D^0 \rightarrow K^- \pi^+$	0.0388 ± 0.0005
$D^0 \rightarrow K^- \pi^+ \pi^0$	0.1390 ± 0.005
$D^0 \rightarrow K^- \pi^+ \pi^+ \pi^-$	0.0808 ± 0.002
$D^0 \rightarrow K_S^0 \pi^+ \pi^-$	0.0283 ± 0.002
$D^0 \rightarrow K_S^0 \pi^+ \pi^- \pi^0$	0.0520 ± 0.006
$D^0 \rightarrow K_S^0 \pi^0$	0.0119 ± 0.0004
$D^0 \rightarrow K^+ K^-$	0.0040 ± 0.00008
$D^0 \rightarrow \pi^+ \pi^-$	0.0014 ± 0.00003
$D^0 \rightarrow K_S^0 K_S^0$	0.0002 ± 0.00004
$D^0 \rightarrow \pi^0 \pi^0$	0.0008 ± 0.00004
$D^0 \rightarrow K_S^0 \pi^0 \pi^0$	0.0091 ± 0.0011
$D^0 \rightarrow K^- \pi^+ \pi^+ \pi^- \pi^0$	0.0420 ± 0.004
$D^0 \rightarrow \pi^+ \pi^- \pi^0$	0.0143 ± 0.0006

Table 6.1.: Branching ratios of the hadronic D meson decays used in this analysis.

These modes have been selected based on the amount of signal and background events they contribute to the overall analysis. Modes with high background and low signal could increase the statistical error of the measurement and would thus be detrimental. The criterion which a channel has to pass is based on the figure of merit (F.O.M.). The F.O.M. corresponds to the expected statistical significance and is defined as:

$$\text{F.O.M.} = \frac{S}{\sqrt{S+B}}, \quad (6.1)$$

where S is the number of signal events and B is the number of background events. Only modes that increase the overall F.O.M. have been selected for this analysis. A table of the impact on the F.O.M. of the single channels can be seen in appendix A.

The D mesons are assembled in their different modes from the charged particles and photons that remain in the event after the B_{tag} and charged lepton were reconstructed. All charged particle trajectories need to satisfy the impact parameter requirements $\Delta r < 0.5$ cm and $\Delta z < 2$ cm.

6. Experimental Procedure

Charged kaons are required to have a Belle kaon likelihood relative to pions of $L(K : \pi) \geq 0.1$, while no identification requirement is applied on charged pions.

Photons must have a minimum energy of 50 MeV in the barrel region ($32^\circ < \theta < 130^\circ$). In the forward region ($17^\circ < \theta < 32^\circ$) a higher energy of $E_\gamma > 100$ MeV is required, and in the backward region ($130^\circ < \theta < 150^\circ$) photons must satisfy $E_\gamma > 150$ MeV.

Neutral pions (π^0) are reconstructed from their decay to two photons. I require the invariant mass to be $|M_{\gamma\gamma} - M_{\pi^0}| < 15$ MeV. All π^0 candidates satisfying this condition are sorted according to the energy of their most energetic γ . In the case that two pions share the same higher energetic photon, the energy of the second photons is used for ordering. Genuine neutral pions have higher likelihoods of having one high energetic γ than their combinatorial background. Pions at the top of the list have thus higher probabilities of being genuine. It is desirable to reduce the possible π^0 candidates by a high degree since neutral pions are a big source of combinatorics in the channels that contain them. Alas, a hard requirement on the higher energetic γ leads to high efficiency losses. I thus perform a reduction to a maximal compatible set of pion candidates. Starting from the top of the list, the γ pairs of the candidates are checked for overlap. A π^0 candidate is removed if any of its photons has already been used by a candidate higher in the list.

K_S^0 mesons are reconstructed from their decay to two charged pions. I require the reconstructed invariant mass to lie within 0.482-0.514 GeV, corresponding to four times the experimental resolution. Further selection criteria are applied based on the momentum of the K_S^0 meson in the laboratory frame. Table 6.2 lists the requirements for the three considered momentum regions.

	$p_{\text{lab}} < 0.5 \text{ GeV}$	$0.5 \text{ GeV} \leq p_{\text{lab}} \leq 1.5 \text{ GeV}$	$p_{\text{lab}} > 1.5 \text{ GeV}$
Δr [cm]	> 0.05	> 0.03	> 0.02
$\Delta\phi$ [rad]	< 0.3	< 0.1	< 0.03
z_{dist} [cm]	< 0.8	< 1.8	< 2.4
flight length [cm]	–	> 0.08	> 0.22

Table 6.2.: K_S^0 momentum dependent requirements.

The first criterion is the smaller impact parameter of the two charged pions in the $R\phi$ -plane (Δr). K_S^0 mesons have a mean lifetime of $(8.954 \pm 0.004) \times 10^{-11}$ s and thus decay farther from the IP than most other particles resulting in higher Δr values of the charged pion tracks. The next criterion is the angle in the $R\phi$ -plane between the vector from the IP to the K_S^0 vertex and the reconstructed K_S^0 flight direction $\Delta\phi$. As a neutral particle, the K_S^0 meson moves in a straight path from the IP and $\Delta\phi$ should thus be small. Third, z_{dist} denotes the smallest distance in z -direction between the two pion trajectories. Since a genuine K_S^0 results in the pions coming from the same vertex, this value is supposed to be small and only nonzero due to reconstruction uncertainties. The last criterion is the flight length of the K_S^0 . For higher momenta one can expect an average minimum flight length before the decay.

Finally, I assemble the D meson from the π^+ , π^0 , K^+ and K_S^0 candidates. The invariant mass of the reconstructed D must lie within ± 3 standard deviations of the nominal D^0 or D^+ mass. The width of the mass peak is determined by fitting the mass distribution of genuinely reconstructed D candidates in the MC in each channel. See appendix B for details. Figure 6.2 depicts the mass distribution of the reconstructed D candidates before the restriction on the mass is applied.

6.3.3. Further Background Suppression

To remove background remaining after the selections applied so far, the following requirements are made:

- The missing mass squared is between⁴ -0.5 and 2 GeV^2 . The missing mass is defined by $M_{\text{miss}}^2 = (p_{\text{LER}} + p_{\text{HER}} - p_{B_{\text{tag}}} - p_D - p_\ell)^2$ and will be discussed in section 6.3.5.
- No charged particle tracks are allowed in the event beside the ones used for the reconstruction of B_{tag} , the charged lepton and the D meson candidate.
- The quality of the B_{tag} candidate has to be $o_{\text{tag}} > 0.001$.
- The reconstructed 4-momentum of the B_{tag} must satisfy the beam constrained mass criterion of $M_{\text{bc}} > 5.24 \text{ GeV}$, with $M_{\text{bc}} = \sqrt{E_{\text{beam}}^2 - \vec{p}_{B_{\text{tag}}}^2}$, where E_{beam} is the energy of one beam in the center of mass frame, and $\vec{p}_{B_{\text{tag}}}$ is the momentum of the B_{tag} candidate.
- $R_2 < 0.4$, where R_2 is the ratio of the second to the zeroth Fox-Wolfram moment [45]. This is an event-shape variable ranging from 0 to 1 with 0 corresponding to spherical events as is expected of $\Upsilon(4S) \rightarrow B\bar{B}$ decays. Background from hadronic events not containing the $\Upsilon(4S)$ resonance contain QCD jets and thus do not exhibit a spherical momentum distribution.
- $E_{\text{ECL}} < 1 \text{ GeV}$, where E_{ECL} is the energy remaining in the electro-magnetic calorimeter after excluding clusters associated to reconstructed tracks and photons used on the tag- and signal side.
- $\cos \psi > 0.5$, where ψ is the opening angle of the two photons in $\pi^0 \rightarrow \gamma\gamma$ in the center of mass frame. Note that this requirement only applies to channels with π^0 candidates.

6.3.4. Optimization of the Selection on Monte Carlo Data

While many of the required values mentioned so far come from long experience at the Belle collaboration or from detector restrictions (*e.g.* lepton momenta and angles), some of the selection criteria given in the previous section still leave room for optimization. The used values have been verified to maximize the figure of merit.

Therefore, I have varied the corresponding selection criteria and measured the F.O.M. as a function of the selection value using MC data. Assuming that the systematic uncertainty does not depend strongly on the selection under consideration, the optimal selection value corresponds to the maximum of the F.O.M. distribution.

⁴The purpose of this selection is not primarily background suppression, but to reduce the M_{miss}^2 distribution to a range that can reasonably well be fitted in the signal yield extraction. M_{miss}^2 can exhibit long tails to the left and right containing a very low number of events.

6. Experimental Procedure

For highest statistics the optimization is done for all D meson channels and all 4 samples combined. I have verified that an optimization channel-by-channel does not lead to significantly different results. In particular, I have varied the selections on the following four quantities (in the given order): o_{tag} of the B_{tag} candidate, R_2 , E_{ECL} and $\cos\psi$.

The optimization in o_{tag} is shown in Figure 6.3a. A broad maximum can be seen in the region $o_{\text{tag,cut}} < 0.001$, which confirms the choice of the selection criterion⁵ $o_{\text{tag}} > 0.001$. Next, the requirement on R_2 is varied (Figure 6.3b) and again a broad optimum is found in the region $R_{\text{cut}} > 0.4$. Similarly, the distributions for E_{ECL} is shown in Figure 6.3c. Finally, the optimization for $\cos\psi$ can be seen in Figure 6.3d. Note that the absolute value of the F.O.M. cannot be compared directly to the ones in the previous plots, as only a subset of the channels contains a π^0 candidate. Figs. 6.4a - 6.4e show the distributions of the residual charged tracks, $\log_{10}(o_{\text{tag}})$, R_2 , E_{ecl} and $\cos\psi$ right before their respective requirements are applied.

After the application of all requirements the multiplicity of reconstructed events is very low ($< 2\%$) and thus no best candidate selection is applied.

⁵As one can see in Figure 6.3 each of the selection criteria is a little bit tighter than the maximum. This results in higher purity and less efficiency. There are two main reasons for this choice. First, the F.O.M. does not take into account systematics, so it is better to be more strict. Second, the analysis relies on the calibration with the inclusive channel $B \rightarrow X\ell\nu_\ell$ which due to its inclusive nature favors much tighter criteria.

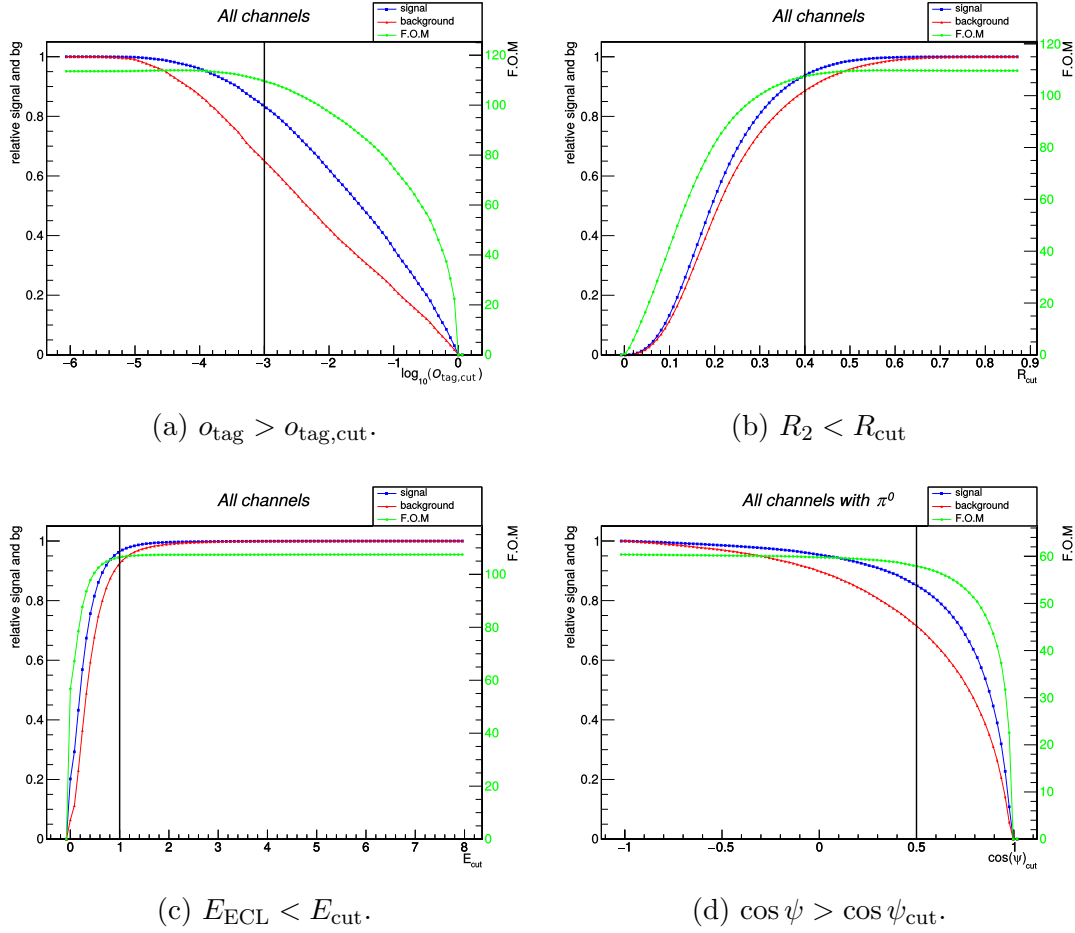


Figure 6.3.: Figure of merit of the $B \rightarrow D\ell\nu_\ell$ reconstruction for the optimized selection criteria. The requirements are applied sequentially, *i.e.* in (b) the criterion from (a) was already applied. The vertical bars mark the chosen requirement values.

6. Experimental Procedure

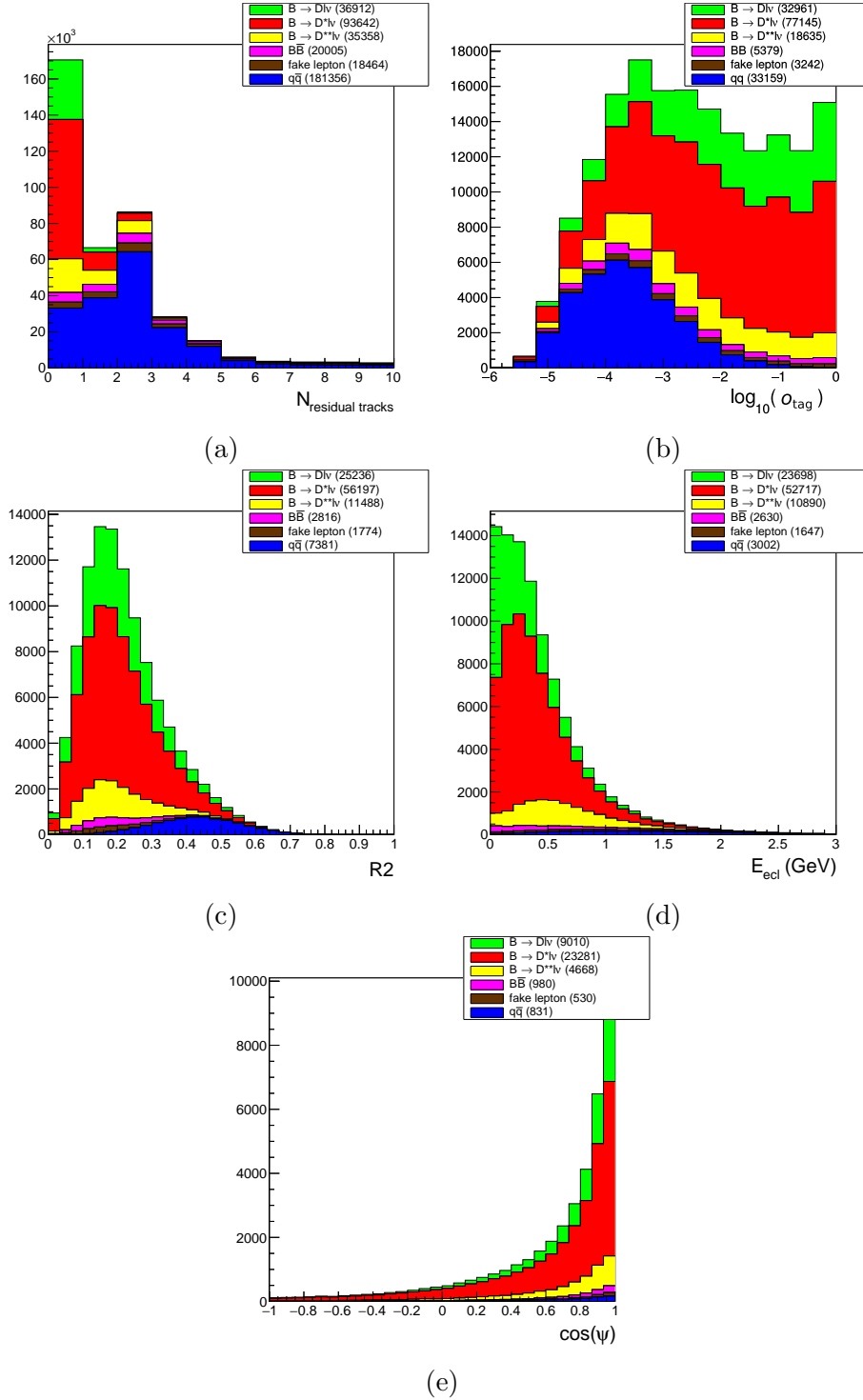


Figure 6.4.: Distribution of the requirement parameters in the Monte Carlo right before the respective selection criterion is applied. Numbers in the brackets denote the number of reconstructed events in the MC. The $B \rightarrow Dlv_\ell$ signal is the uppermost (green) component, the other background components are described in section 6.3.5.

6.3.5. Signal Yield Extraction

The full reconstruction of the event can be used to infer the neutrino and thus discriminate signal from background. The missing 4-momentum after the reconstruction of the B_{tag} candidate, the D meson and the lepton is calculated relative to the beam energies. Its square corresponds to the missing invariant mass squared of the event:

$$M_{\text{miss}}^2 = (p_{\text{LER}} + p_{\text{HER}} - p_{B_{\text{tag}}} - p_D - p_\ell)^2, \quad (6.2)$$

where p_{HER} and p_{LER} are the 4-momenta of the positron and electron beam, respectively and $p_{B_{\text{tag}}}$, p_D and p_ℓ are the momenta of B_{tag} , D meson and charged lepton candidates, respectively. In a genuine signal event the only particle that is missing in the reconstruction is the neutrino and the missing mass distribution thus exhibits a peak at zero.

By fitting the M_{miss}^2 distribution one can thus measure the number of $B \rightarrow D\ell\nu_\ell$ decays and background. In this analysis I consider the following components in the yield fits:

- $B \rightarrow D\ell\nu_\ell$ *signal (floating)*: Correctly reconstructed $B \rightarrow D\ell\nu_\ell$ events and $B \rightarrow D\ell\nu_\ell$ events where the D meson was wrongly reconstructed, but still comes from a $B \rightarrow D\ell\nu_\ell$ decay⁶.
- $B \rightarrow D^*\ell\nu$ *cross-feed (floating)*: D^* meson decays to either $D\pi$ or $D\gamma$.
- *Other backgrounds (fixed)*: This component contains $B \rightarrow X_u\ell\nu_\ell$ and D^{**} candidates, D -mesons from the tag side wrongly attributed to the signal side B , non-prompt (*i.e.* cascade) leptons, fake leptons, and $e^+e^- \rightarrow q\bar{q}$ continuum.

To better understand the contribution of the background components I further define the following 6 components, essentially splitting “other background” into its constituents. The following list also shows the procedure of determining the type of a reconstructed event. The categorization starts at the first item and if an event does not fall into its category the next item is considered:

1. $B \rightarrow D\ell\nu_\ell$ *signal*: As defined above.
2. $e^+e^- \rightarrow q\bar{q}$ *continuum*: Events without the $\Upsilon(4S)$ resonance.
3. *Fake lepton*: The lepton hypothesis is wrong (*e.g.* a pion identified as electron).
4. $B \rightarrow D^*\ell\nu_\ell$: As defined above.

⁶Including $B \rightarrow D\ell\nu_\ell$ events with wrong D meson reconstruction has a very minor broadening impact on the width of the signal peak, but the inclusion is necessary since this component scales with the decay width (and thus $|V_{cb}|$) and is much too small to be fitted separately.

6. Experimental Procedure

5. $B \rightarrow D^{**} \ell \nu_\ell$: D^{**} denotes D mesons with an orbital momentum of $L = 1$. As described in section 2.2.2 the charm quark acts almost as a static particle and the possible D^{**} states are thus grouped by the overall angular momentum of the light degrees of freedom: $\vec{j}_q = \vec{s}_q + \vec{L}$, where q denotes the light degrees of freedom and L is the orbital momentum. This results in two $j_q = 3/2^+$ states with $J^P = 2^+, 1^+$ and two $j_q = 1/2^+$ states with $J^P = 1^+, 0^+$. I will denote these states as D_2, D_1, D'_1 and D_0^* respectively.
6. $B\bar{B}$: Combinatorial $B\bar{B}$ background where either the lepton or the reconstructed D meson does not belong to the B meson according to MC truth; and $B \rightarrow X_u \ell \nu_\ell$ events.

Figure 6.5 shows the distribution of these components for all four sub-samples ($B^0 \rightarrow D^- e^+ \nu_e, B^0 \rightarrow D^- \mu^+ \nu_\mu, B^+ \rightarrow \bar{D}^0 e^+ \nu_e, B^+ \rightarrow \bar{D}^0 \mu^+ \nu_\mu$) used in the analysis after all requirements are applied.

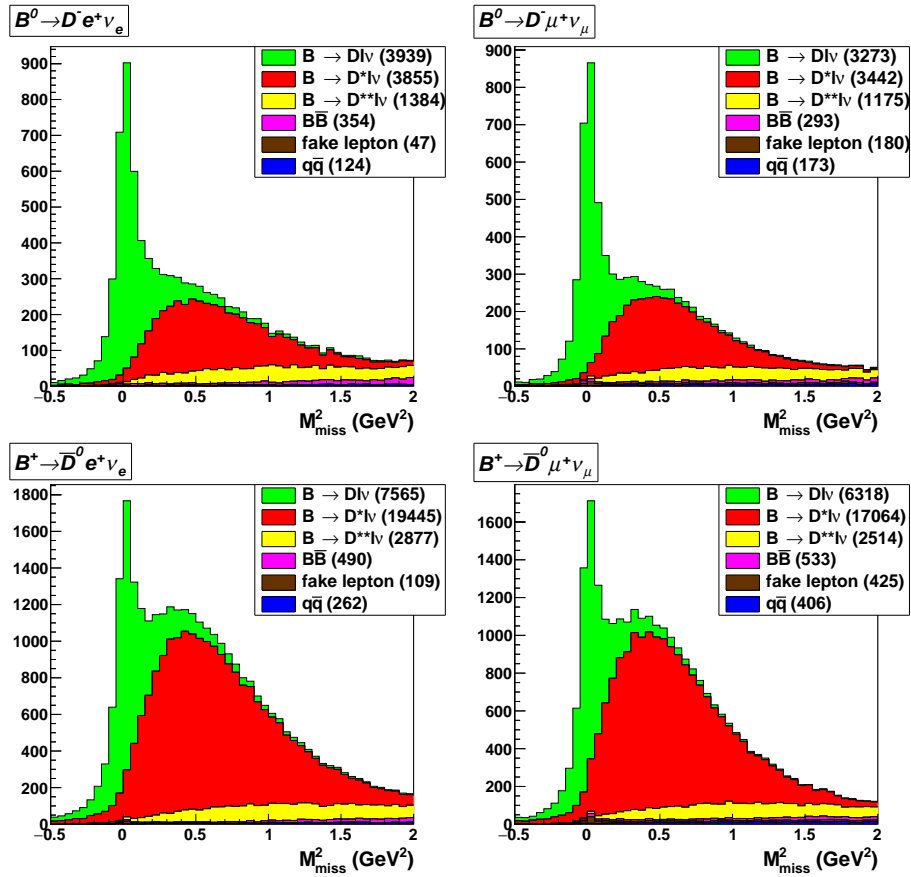


Figure 6.5.: The M_{miss}^2 distribution in the four samples ($B^0 \rightarrow D^- e^+ \nu_e, B^0 \rightarrow D^- \mu^+ \nu_\mu, B^+ \rightarrow \bar{D}^0 e^+ \nu_e, B^+ \rightarrow \bar{D}^0 \mu^+ \nu_\mu$) for MC simulated events. The entire w range is shown and all mentioned requirements are applied. The numbers in the brackets denote the numbers of events.

In order to measure signal yields as a function of the recoil variable w , I split the data into 10 w -bins in the range from $w = 1$ to $w = 1.6$. Note that the kinematic endpoint of the w distribution is ≈ 1.59 and is thus slightly below the upper boundary of the last bin. This results in a decrease of events in the last bin. In every bin, I fit the signal and D^* cross feed using the binned extended maximum likelihood algorithm by Barlow and Beeston [46]. The templates which model the shapes of the components are obtained from MC simulation. The virtue of the Barlow-Beeston algorithm is that it includes the limited statistics of the MC templates in the resulting statistical fit error. The component “other backgrounds” is small in every bin and its contribution is thus fixed to the MC expectation. $B \rightarrow D\ell\nu_\ell$ and the cross feed $B \rightarrow D^*\ell\nu_\ell$ yields are left floating in the fit except in the last bin ($1.54 < w < 1.6$), where I also fix $B \rightarrow D^*\ell\nu_\ell$. Its very low threshold at high w values would make the fit unstable otherwise. While this removes the contribution of $B \rightarrow D^*\ell\nu_\ell$ to the statistical error in the last bin this is compensated by a resulting higher systematic error. Figure 6.6 shows these fits in the $B^0 \rightarrow D^-e^+\nu_e$ sub-sample using MC stream 0 as simulated real data. MC streams 1 to 4 are used to obtain the MC templates. Results of fits with a different choice of pseudo-real data stream and for the different sub-samples are shown in section 7.3.

6. Experimental Procedure

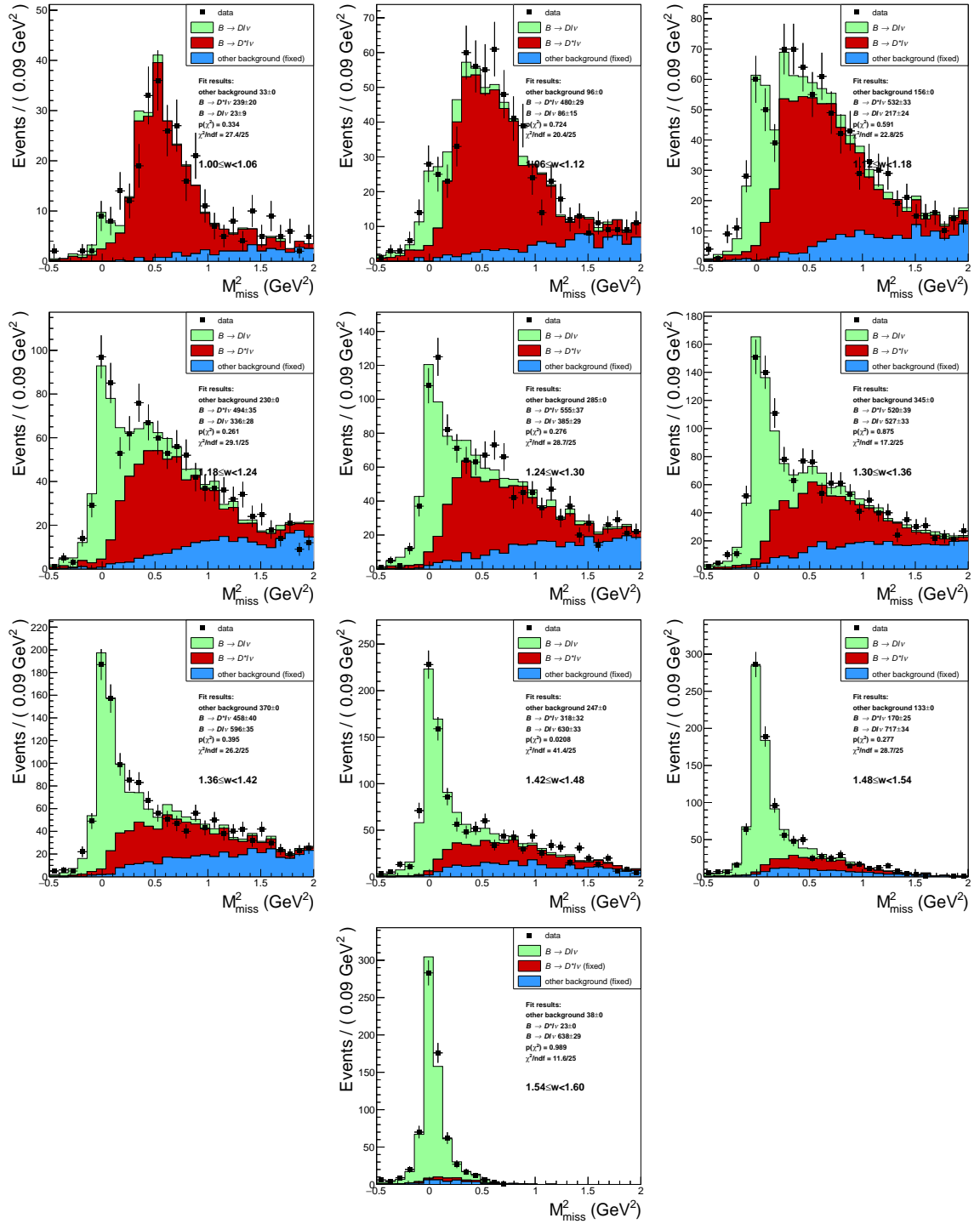


Figure 6.6.: Signal yield extraction in different bins of w in the $B^0 \rightarrow D^- e^+ \nu_e$ subsample. MC stream 0 is used as simulated real data while MC templates are obtained from streams 1 to 4. Shown are the pseudo real data and the yields that result from the fit.

7. Verification of the Procedure on Monte Carlo Data

This analysis followed a blinded approach as is typically required at Belle. Before one is permitted to analyze real data taken at the experiment (the so-called “box opening”), one has to show that the methods of the analysis work on MC simulated data as expected. In this chapter I will present multiple verifications performed to ensure that the analysis procedure is valid. Before complete box opening one has to further show that the background components are reasonably well described in the corrected MC within a signal-blinded region. This will be discussed in chapter 8.

7.1. Resolution of w

The number of signal events in the 10 w -bins only follows the distribution of the differential decay width if no significant bin-to-bin migration takes place which would effectively smear out the distribution. Bin-to-bin migration effects depend on the experimental resolution of the reconstructed w . Studying MC data, I verified that the resolution is below a tenth of the w -bin width (0.06), see Figure 7.1. Thus I do not take into account finite resolution effects in this analysis.

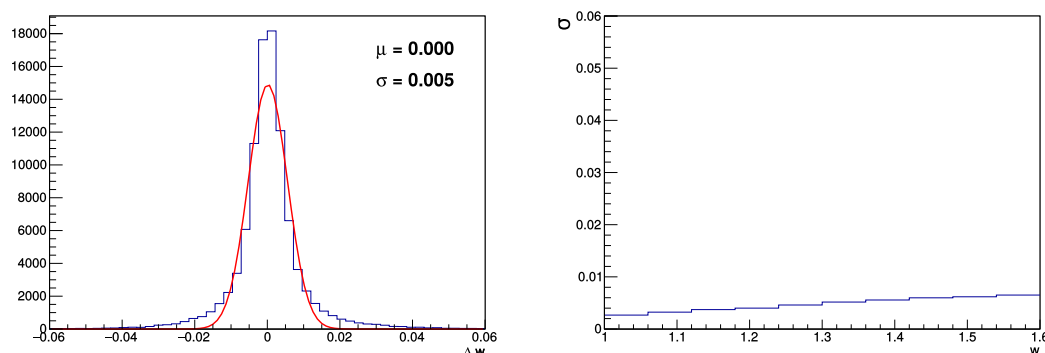


Figure 7.1.: Fit of the w resolution of all w -bins combined (left) and the results of such fits in the separate bins (right). The bin width is 0.06. The plot contains all reconstructed signal events from the MC after the final selection criteria. All 5 MC-streams are combined.

7.2. Validation of the Signal Yield Extraction with the Barlow-Beeston Fit

In order to verify that the extended binned maximum likelihood fit of the signal yield (see 6.3.5) is not biased and has a proper error estimation I perform a toy Monte Carlo test. The 5 MC streams are combined for maximum statistics and the resulting data sample is used both as template for the yield components and as the pseudo-real data. In 1000 iterations I vary the values of each M_{miss}^2 bin using the expected Poisson error. This is performed both for the pseudo-real data and for every component of the floating yields independently. In each iteration I then perform the fit and calculate a “pull” value of the measured signal yield:

$$\text{pull} = \frac{N_{\text{true}} - N_{\text{fit}}}{\sigma_{\text{fit}}} \quad (7.1)$$

For an unbiased fit with perfect error estimation the resulting pull value distribution is a Gaussian distribution with $\mu = 0$ and $\sigma = 1$. μ values significantly differing from zero indicate a bias and σ values above one indicate that the error is underestimated, while smaller values indicate overestimation. The results for the sub-sample $B^0 \rightarrow D^- e^+ \nu_e$ for each w -bin are shown in Figure 7.2, the other three sub-samples yield similar results. I applied Gaussian fits to determine μ and σ . One can see that μ is consistent with zero, *i.e.* the fit is not biased. The values of σ are smaller than one, *i.e.* the errors are overestimated a bit by the fitting procedure.

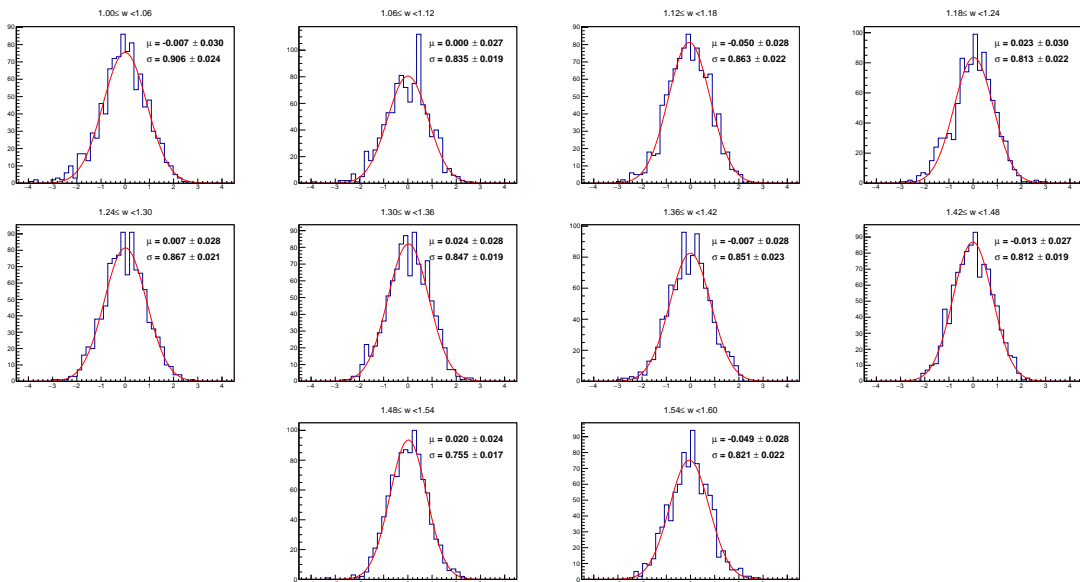


Figure 7.2.: Pull distributions of toy Monte Carlo simulations of the yield extraction fit in the sample $B^0 \rightarrow D^- e^+ \nu_e$.

7.3. Validation of the Fit Procedure

The differential decay width of $B \rightarrow D\ell\nu_\ell$ simulated in the generic Belle MC is based on the CLN form-factor parameterization described in section 2.2.3. The input parameters of the simulation are the ρ^2 value and the branching fraction. These two parameters then fix the $\eta_{\text{EW}}\mathcal{G}(1)|V_{cb}|$ value implicitly in the MC. I list the parameters for the four sub-samples in Table 7.1.

The correct working of the entire measurement chain can be verified in the MC by showing that a fit of the MC data yields the original values with which the MC was simulated, differing only by statistical¹ errors. The fitting procedure using the CLN parameterization will be outlined in chapter 10.

sub-sample	ρ^2	branching fraction [%]	$\eta_{\text{EW}}\mathcal{G}(1) V_{cb} [10^{-3}]$
$B^0 \rightarrow D^- e^+ \nu_e$	1.16	2.13	42.1367
$B^0 \rightarrow D^- \mu^+ \nu_\mu$	1.16	2.13	42.1367
$B^+ \rightarrow \bar{D}^0 e^+ \nu_e$	1.15	2.31	42.0476
$B^+ \rightarrow \bar{D}^0 \mu^+ \nu_\mu$	1.15	2.31	42.0476

Table 7.1.: Parameters used for the simulation of $B \rightarrow D\ell\nu_\ell$ decays in the generic MC.

I use one out of the 5 generic MC streams as pseudo-real data while the other 4 streams are used to obtain the templates for the M_{miss}^2 fits. By repeating this procedure with each of the 5 streams as pseudo-real data I obtain five values of $\eta_{\text{EW}}\mathcal{G}(1)|V_{cb}|$ and ρ^2 for each sub-sample. The results are shown in Figure 7.3 and in Table 7.2. As expected, the values vary around the parameters the MC was simulated with, within their statistical errors.

¹The MC may not be a perfect description of real data, but trivially it is a perfect description of itself and thus no systematic errors apply when working within the MC.

7. Verification of the Procedure on Monte Carlo Data

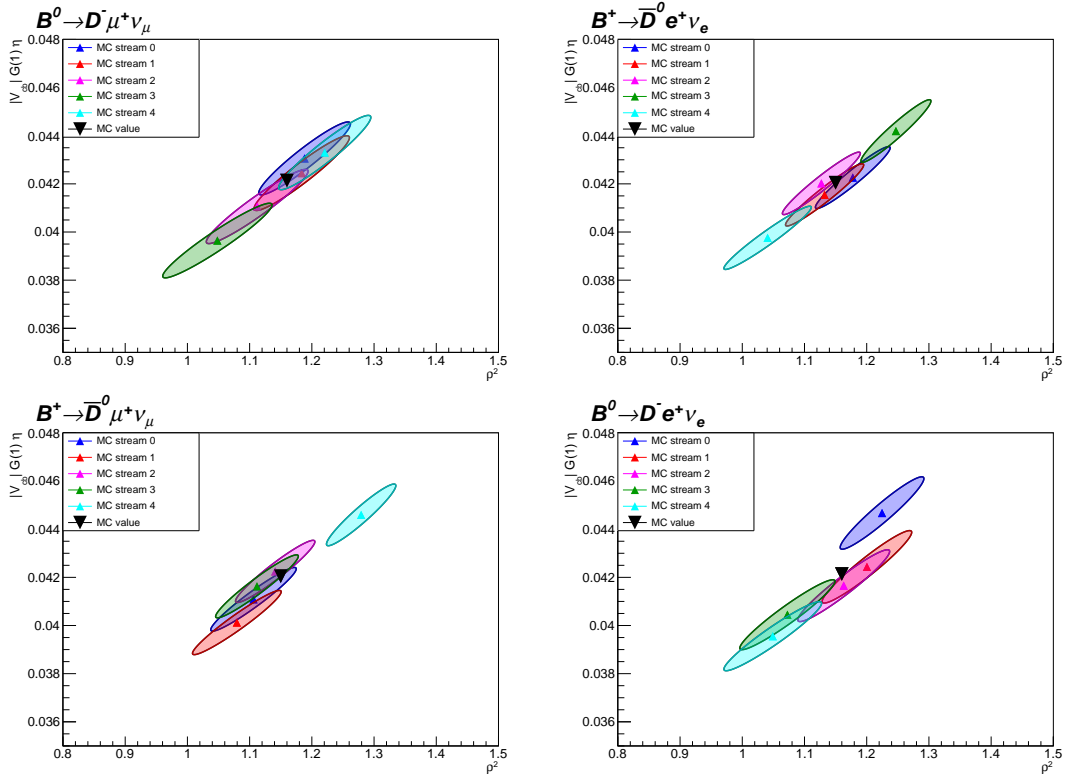


Figure 7.3.: MC test of the fit procedure in the different samples. The contours show 1σ of the statistical error, *i.e.* contain 39% of the confidence interval.

sample	stream	$\eta_{EW} \mathcal{G}(1) V_{cb} [10^{-3}]$	ρ^2	correlation	χ^2/n_{df}	$p(\chi^2)$
$B^+ \rightarrow D^0 e^+ \nu_e$	0	42.26 ± 1.29	1.178 ± 0.060	0.958	13.454/8	0.097
$B^+ \rightarrow \bar{D}^0 e^+ \nu_e$	1	41.54 ± 1.29	1.132 ± 0.063	0.960	5.298/8	0.725
$B^+ \rightarrow \bar{D}^0 e^+ \nu_e$	2	42.02 ± 1.30	1.127 ± 0.063	0.961	5.146/8	0.742
$B^+ \rightarrow \bar{D}^0 e^+ \nu_e$	3	44.19 ± 1.30	1.247 ± 0.056	0.956	5.956/8	0.652
$B^+ \rightarrow \bar{D}^0 e^+ \nu_e$	4	39.76 ± 1.31	1.041 ± 0.070	0.964	6.474/8	0.594
$B^+ \rightarrow \bar{D}^0 \mu^+ \nu_\mu$	0	41.09 ± 1.32	1.106 ± 0.069	0.956	1.816/8	0.986
$B^+ \rightarrow \bar{D}^0 \mu^+ \nu_\mu$	1	40.12 ± 1.33	1.079 ± 0.071	0.959	17.878/8	0.022
$B^+ \rightarrow \bar{D}^0 \mu^+ \nu_\mu$	2	42.25 ± 1.29	1.141 ± 0.064	0.954	6.036/8	0.643
$B^+ \rightarrow \bar{D}^0 \mu^+ \nu_\mu$	3	41.63 ± 1.31	1.112 ± 0.067	0.956	8.804/8	0.359
$B^+ \rightarrow \bar{D}^0 \mu^+ \nu_\mu$	4	44.59 ± 1.28	1.279 ± 0.056	0.947	4.383/8	0.821
$B^0 \rightarrow D^- e^+ \nu_e$	0	44.67 ± 1.51	1.225 ± 0.067	0.950	8.054/8	0.428
$B^0 \rightarrow D^- e^+ \nu_e$	1	42.44 ± 1.51	1.200 ± 0.072	0.952	11.449/8	0.178
$B^0 \rightarrow D^- e^+ \nu_e$	2	41.66 ± 1.49	1.163 ± 0.074	0.952	6.743/8	0.565
$B^0 \rightarrow D^- e^+ \nu_e$	3	40.45 ± 1.45	1.073 ± 0.077	0.953	6.595/8	0.581
$B^0 \rightarrow D^- e^+ \nu_e$	4	39.56 ± 1.44	1.049 ± 0.079	0.953	10.524/8	0.230
$B^0 \rightarrow D^- \mu^+ \nu_\mu$	0	43.06 ± 1.52	1.188 ± 0.074	0.944	11.042/8	0.199
$B^0 \rightarrow D^- \mu^+ \nu_\mu$	1	42.45 ± 1.55	1.184 ± 0.077	0.947	9.499/8	0.302
$B^0 \rightarrow D^- \mu^+ \nu_\mu$	2	41.06 ± 1.54	1.112 ± 0.082	0.950	8.977/8	0.344
$B^0 \rightarrow D^- \mu^+ \nu_\mu$	3	39.65 ± 1.55	1.048 ± 0.088	0.953	6.795/8	0.559
$B^0 \rightarrow D^- \mu^+ \nu_\mu$	4	43.30 ± 1.54	1.221 ± 0.074	0.945	7.265/8	0.508

Table 7.2.: Results of the fit applied on pseudo real data. The “stream” column denotes which stream was used as pseudo-real data, the other four streams were used as templates for the yield extraction.

7.4. Stability w.r.t. Binning

To verify that the fit procedure is stable for different choices of binning in both M_{miss}^2 and w , I perform the fit mentioned in the previous section using different bin widths. Figure 7.4 shows the dependence of the extracted $\eta_{\text{EW}}\mathcal{G}(1)|V_{cb}|$ and ρ^2 on the M_{miss}^2 bin width and Figure 7.5 shows the dependences on the w bin width. As before this is done for each different MC stream as pseudo real data and for each sub-sample. One can see that the fluctuations are well within the statistical errors. There are some rare outliers and configurations where a yield fit did not converge (seen as missing data point in the figures). I verified that the actual binning choice² of $n_{M_{\text{miss}}^2} = 28$ and $n_w = 10$ produces neither of these situations in both the MC-tests and in the application on real data.

²The general possibilities of binning are practically infinite. I restricted the binnings to equally spaced bins since this makes distributions in w and M_{miss}^2 immediately clear. The main motivation for choosing 10 bins for w is the BaBar analysis of $B \rightarrow D\ell\nu_\ell$ [22]. Choosing the same binning makes the distributions easy to compare and aids the averaging of the measurements. The choice of 28 bins for M_{miss}^2 has two motivations. First, the number of bins should be high enough to clearly see the underlying shapes, but not too high or otherwise statistical fluctuations between bins would become too present. Second, among the remaining available numbers, 28 has the advantage of placing one bin rather centrally on top of the peak center at $M_{\text{miss}}^2 = 0$.

7. Verification of the Procedure on Monte Carlo Data

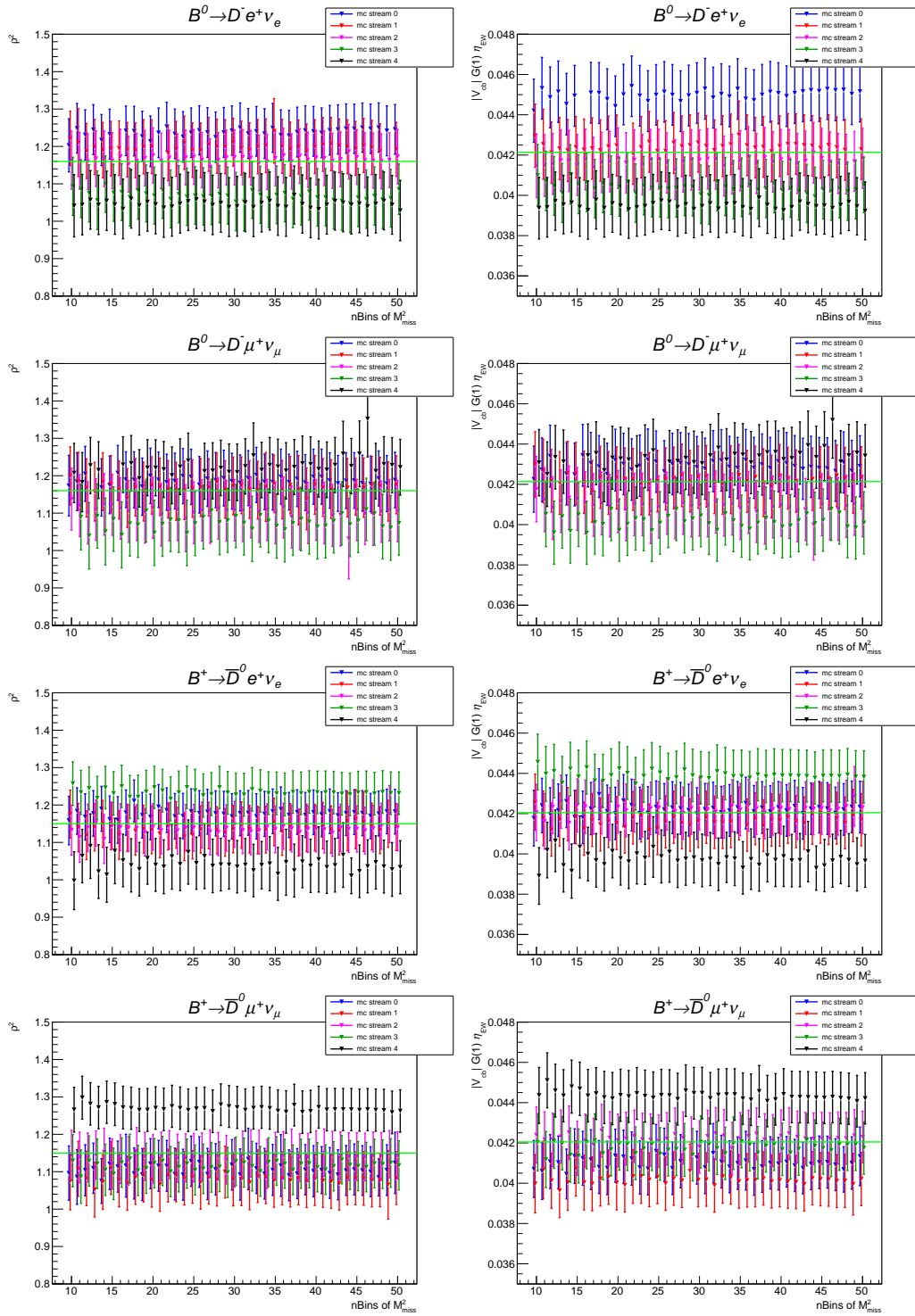


Figure 7.4.: $\eta_{\text{EW}} \mathcal{G}(1) |V_{cb}|$ and ρ^2 extracted from pseudo real data in dependence of the number of M_{miss}^2 bins for each sub-sample.

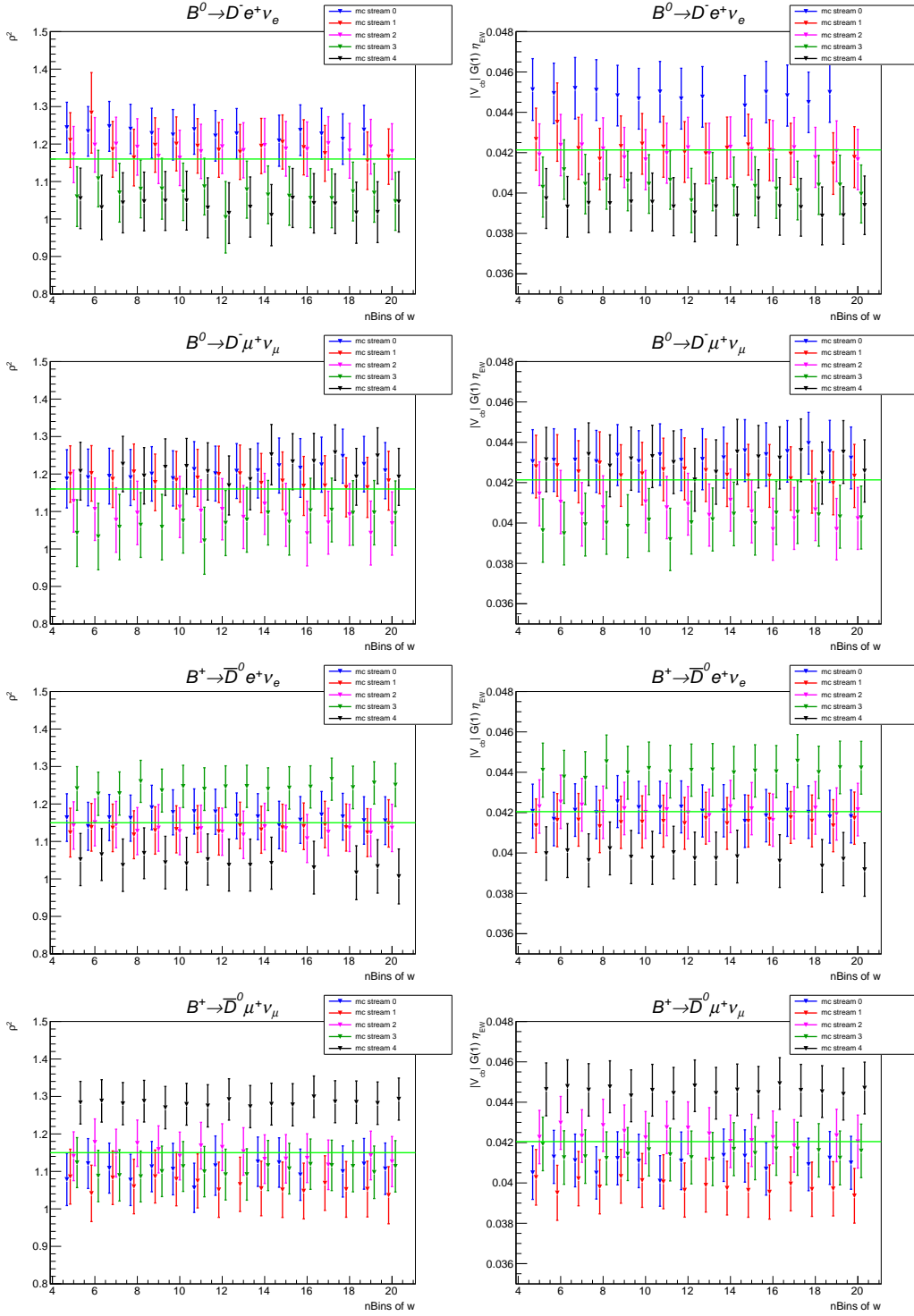


Figure 7.5.: $\eta_{EW} \mathcal{G}(1) |V_{cb}|$ and ρ^2 extracted from pseudo real data in dependence of the number of w bins for each sub-sample.

8. MC Corrections

The use of MC generated data has the advantage of realistically simulating the expected decay spectra, especially for well known decays such as $B \rightarrow D\ell\nu_\ell$. However, no MC simulation is perfect and it is thus necessary to calibrate it. The default approach at Belle is to perform all known applicable corrections to the MC and then to compare data reconstructed from the MC to real data in the sidebands (*i.e.* before full box opening) to verify a genuine description. In this chapter I will introduce the multiple calibrations applied to MC data, and later in section 9.1 I will present their respective systematic errors.

The calibration of the MC is done with eventwise weights. For each necessary correction the amount of real data and MC-simulated events is compared and a coefficient is calculated:

$$\text{weight} = \frac{N_{\text{data}}}{N_{\text{MC}}} \quad (8.1)$$

The source of these events depends on the studied calibration. For example, the calibration of the tagging efficiency is determined by studying the inclusive decay $B \rightarrow X\ell\nu_\ell$ with hadronic tags as I will outline in section 8.6. For many calibrations weights are determined separately in multiple different kinematic regions. For example particle identification is mostly dependent on the θ angle and the momentum of the identified particle. Thus particle identification weights are applied depending on these values. A single event is then weighted with a product of all the weights that apply to it:

$$\text{weight} = \text{weight}_1 \times \text{weight}_2 \times \text{weight}_3 \dots \quad (8.2)$$

In the following I discuss each correction applied in this analysis.

8.1. Correction of Hadronic D Branching Fractions

Both the signal decay $B \rightarrow D\ell\nu_\ell$ and the dominant background from $B \rightarrow D^*\ell\nu_\ell$ contain subsequent hadronic decays of the D meson. The relevant branching fractions thus need to be corrected to the most actual measured values which are taken from the data provided by the particle data group (PDG) [13]. These branching fractions are compared with the values used in the MC simulation to calculate the weights given in Table 8.1.

D decay	\mathcal{B} in Monte Carlo	\mathcal{B} in PDG[13]	weights
$D^+ \rightarrow K^- \pi^+ \pi^+$	0.0951	0.0913 ± 0.0019	0.9600 ± 0.0200
$D^+ \rightarrow K^- \pi^+ \pi^+ \pi^0$	0.0602	0.0599 ± 0.0018	0.9950 ± 0.0299
$D^+ \rightarrow K_S^0 \pi^+$	0.0147	0.0147 ± 0.0007	1.0000 ± 0.0476
$D^+ \rightarrow K_S^0 \pi^+ \pi^0$	0.0651	0.0699 ± 0.0027	1.0737 ± 0.0415
$D^+ \rightarrow K^+ K^- \pi^+$	0.0091	0.0095 ± 0.0003	1.0440 ± 0.0330
$D^+ \rightarrow K_S^0 K^+$	0.0030	0.0028 ± 0.0002	0.9333 ± 0.0667
$D^+ \rightarrow K_S^0 \pi^+ \pi^+ \pi^-$	0.0316	0.0312 ± 0.0011	0.9873 ± 0.0348
$D^+ \rightarrow \pi^+ \pi^0$	0.0026	0.0012 ± 0.00006	0.4615 ± 0.0231
$D^+ \rightarrow \pi^+ \pi^+ \pi^-$	0.0037	0.0032 ± 0.0002	0.8649 ± 0.0541
$D^+ \rightarrow K^- \pi^+ \pi^+ \pi^+ \pi^-$	0.0062	0.0056 ± 0.0005	0.9032 ± 0.0806
$D^0 \rightarrow K^- \pi^+$	0.0382	0.0388 ± 0.0005	1.0157 ± 0.0131
$D^0 \rightarrow K^- \pi^+ \pi^0$	0.1308	0.1390 ± 0.005	1.0627 ± 0.0382
$D^0 \rightarrow K^- \pi^+ \pi^+ \pi^-$	0.0709	0.0808 ± 0.002	1.1396 ± 0.0282
$D^0 \rightarrow K_S^0 \pi^+ \pi^-$	0.0284	0.0283 ± 0.002	0.9965 ± 0.0704
$D^0 \rightarrow K_S^0 \pi^+ \pi^- \pi^0$	0.0517	0.0520 ± 0.006	1.0058 ± 0.1161
$D^0 \rightarrow K_S^0 \pi^0$	0.0113	0.0119 ± 0.0004	1.0531 ± 0.0354
$D^0 \rightarrow K^+ K^-$	0.0039	0.0040 ± 0.00008	1.0256 ± 0.0205
$D^0 \rightarrow \pi^+ \pi^-$	0.0014	0.0014 ± 0.00003	1.0000 ± 0.0214
$D^0 \rightarrow K_S^0 K_S^0$	0.0004	0.0002 ± 0.00004	0.5000 ± 0.1000
$D^0 \rightarrow \pi^0 \pi^0$	0.0008	0.0008 ± 0.00004	1.0000 ± 0.0500
$D^0 \rightarrow K_S^0 \pi^0 \pi^0$	0.0093	0.0091 ± 0.0011	0.9785 ± 0.1183
$D^0 \rightarrow K^- \pi^+ \pi^+ \pi^- \pi^0$	0.0398	0.0420 ± 0.004	1.0553 ± 0.1005
$D^0 \rightarrow \pi^+ \pi^- \pi^0$	0.0140	0.0143 ± 0.0006	1.0214 ± 0.0429

Table 8.1.: Corrected branching ratios of the hadronic channels of the D meson and the resulting weights.

8.2. Correction of Semileptonic $B \rightarrow X_c \ell \nu_\ell$ Decays

Two exclusive $B \rightarrow X_c \ell \nu_\ell$ decays other than the signal $B \rightarrow D \ell \nu_\ell$ play an important role in this analysis: the main background $B \rightarrow D^* \ell \nu_\ell$ and the much smaller but less well known $B \rightarrow D^{**} \ell \nu_\ell$ background. Their branching fractions are corrected to recent values listed in Table 8.2 found in the PDG [13] (for $B \rightarrow D^* \ell \nu_\ell$) and based on values determined by HFAG [21] (for $B \rightarrow D^{**} \ell \nu_\ell$).

Decay	\mathcal{B} in MC	\mathcal{B} based on PDG/HFAG	weight
$B^+ \rightarrow D^{*0} \ell \nu$	0.0579	0.0569 ± 0.0019	0.9827 ± 0.0328
$\bar{B}^0 \rightarrow D^{*+} \ell \nu$	0.0533	0.0493 ± 0.0011	0.9250 ± 0.0206
$B^+ \rightarrow D_1^0 \ell \nu$	0.0074	0.0074 ± 0.0011	1.0000 ± 0.1486
$B^+ \rightarrow D_2^0 \ell \nu$	0.0036	0.0047 ± 0.0017	1.3056 ± 0.4722
$B^+ \rightarrow D_1^{\prime 0} \ell \nu$	0.0020	0.0026 ± 0.0009	1.3000 ± 0.4500
$B^+ \rightarrow D_0^{*0} \ell \nu$	0.0084	0.0052 ± 0.0022	0.6190 ± 0.2619
$\bar{B}^0 \rightarrow D_1^+ \ell \nu$	0.0074	0.0074 ± 0.0011	1.0000 ± 0.1486
$\bar{B}^0 \rightarrow D_2^+ \ell \nu$	0.0036	0.0047 ± 0.0017	1.3056 ± 0.4722
$\bar{B}^0 \rightarrow D_1^{\prime +} \ell \nu$	0.0020	0.0026 ± 0.0009	1.3000 ± 0.4500
$\bar{B}^0 \rightarrow D_0^{*+} \ell \nu$	0.0084	0.0052 ± 0.0022	0.6190 ± 0.2619

Table 8.2.: Branching ratio corrections of $\mathcal{B}(B \rightarrow D^{*(*)} \ell \nu)$.

$B \rightarrow D^* \ell \nu_\ell$ is simulated in the generic MC with the HQET2 model of `EvtGen` which is based on the CLN form-factor parameterization. The additional degrees of freedom relative to the $B \rightarrow D \ell \nu_\ell$ decay are due to the vector nature of D^* resulting in two additional form factor parameters R_1 and R_2 . Table 8.3 compares the values of the form factor constants with ones recently determined by HFAG [21].

Form factor parameter	MC	HFAG
ρ^2	1.300	1.207 ± 0.026
R_1	1.180	1.403 ± 0.033
R_2	0.719	0.854 ± 0.020

Table 8.3.: Parameters of the $B \rightarrow D^* \ell \nu_\ell$ form-factor description in the MC.

Unlike the branching ratio differences which immediately determine the weights, the impact of the form factors depends on the kinematics of the decay. Weights are thus calculated in 24 bins of lepton momentum from 0 to 2.4 GeV and in 12 bins in q^2 from 0 to 12 GeV² resulting in 288 distinct weights.

The decay $B \rightarrow D^{**} \ell \nu_\ell$ was modeled with the ISGW2 quark model of `EvtGen`. This model is meanwhile known to be insufficient and the whole decay is re-weighted to the model of Leibovich-Ligeti-Stewart-Wise (LLSW) [47] using the latest data from HFAG.

8.3. Correction of Semileptonic $B \rightarrow X_u \ell \nu_\ell$ Decays

The semileptonic decays of B mesons to charmless mesons is modeled in the MC by a mixture of the known semileptonic decays and an inclusive model which covers the difference between the sum of the exclusive branching fractions and the inclusive $B \rightarrow X_u \ell \nu_\ell$ branching ratio. I correct the semileptonic branching ratios that are well measured and can be found¹ in the PDG [13], see Table 8.4. I also scale the remaining inclusive part with an average of the inclusive ratio measured in [48] and [49].

Decay	\mathcal{B} in MC	\mathcal{B} from PDG	weight
$B^0 \rightarrow \pi^+ \ell \nu$	0.000136	0.000145 ± 0.000005	1.0662 ± 0.0368
$B^+ \rightarrow \pi^0 \ell \nu$	0.000073	0.000078 ± 0.0000027	1.0685 ± 0.0370
$\bar{B}^0 \rightarrow \rho^+ \ell \nu$	0.000277	0.000294 ± 0.000021	1.0614 ± 0.0758
$B^+ \rightarrow \rho^0 \ell \nu$	0.000149	0.000158 ± 0.000011	1.0604 ± 0.0738
$B^+ \rightarrow \eta \ell \nu$	0.000084	0.000038 ± 0.000006	0.4524 ± 0.0714
$B^+ \rightarrow \eta' \ell \nu$	0.000033	0.000023 ± 0.000008	0.6970 ± 0.2424
$B^+ \rightarrow \omega \ell \nu$	0.000115	0.000119 ± 0.000009	1.0348 ± 0.0783

Table 8.4.: Corrected exclusive branching ratios of $\mathcal{B}(B \rightarrow X_u \ell \nu)$.

8.4. Correction of Particle Identification Efficiencies

Particle identification is based on the Belle likelihood values L_{eid} , $L_{\mu\text{id}}$ and $L(K : \pi)$ as discussed in section 4.2.7, and the reconstruction of K_S^0 and π^0 mesons is based on their dominant decay modes. While the simulation of detection efficiencies through the MC is very elaborate, one can still expect deviations in real data which have to be accounted for. This not only concerns efficiencies, but also “fake rates” where particles are misidentified. The best way to estimate such correction factors is by analyzing decays which are available in abundance and in which particles can easily be identified via the decay structure.

For lepton efficiency corrections a study of $\gamma\gamma \rightarrow \ell^+ \ell^-$ decays is used. These come from events selected for their low multiplicity (*i.e.* the opposite of the criteria for hadronic events). The uncertainties resulting from a hadronic environment is then estimated by comparison to hadronic events with the decay $J/\Psi \rightarrow \ell^+ \ell^-$. The corresponding weights were calculated for multiple bins of θ and lepton momentum and were further determined separately for events with the SVD1 and SVD2 tracking setup.

¹Small modes such as $B^+ \rightarrow f_0 \ell \nu$ are not very well measured yet. Their simulation in the MC is based on theoretical assumptions. However, their contribution to background is extremely small and I thus leave them uncorrected and cover their systematic error by assuming a conservative value of half the predicted branching fraction as their uncertainty.

8. MC Corrections

For the determination of charged kaon and pion efficiencies, as well as for lepton fake rates the decay $D^{*+} \rightarrow D^0\pi^+$ is the preferred mode. The decay has a low available phase space and signal is thus very well separable from background. This manifests in the π^+ having a characteristic low momentum and it is usually referred to by the name “slow pion”. One then studies the further decay of $D^0 \rightarrow K^-\pi^+$, which is one of the cleanest D^0 decay channels, see for example Figure 6.2 of section 6.3.2. The charge of the slow pion is equal to the charge of the pion from the D^0 decay and opposite to the charge of the kaon. Thus one can easily identify the hadrons independently from the identification likelihoods. Fitting the resulting mass distributions for different particle identification requirements in real data and MC one can obtain correction factors. These are again available in multiple kinematic bins of θ and particle momentum.

The π^0 efficiency correction is based on events consisting of a $\tau^-\tau^+$ pair. Events where one τ decays in the channel $\tau^- \rightarrow \pi^-\pi^0\nu_\tau$ while the other decays as $\tau^+ \rightarrow \ell^+\nu_\ell\bar{\nu}_\tau$ are studied. This results in the clean signature of two charged tracks and two photons which can be attributed to the π^0 .

Finally, K_S^0 meson identification is – like kaon and pion efficiency – corrected with the $D^{*+} \rightarrow D^0\pi^+$ decay, but with the further decay of $D^0 \rightarrow K_S^0\pi^+\pi^-$.

8.5. Correction of Luminosity and $\Upsilon(4S)$ Decay Widths

The amount of $\Upsilon(4S) \rightarrow B\bar{B}$ events scales with the luminosity, the branching fractions of $\Upsilon(4S) \rightarrow B^+B^-$ and $\Upsilon(4S) \rightarrow B^0\bar{B}^0$, and the cross section. The two branching ratios are assumed to be each 50% in the MC and are corrected to the most up to date values of $\mathcal{B}(\Upsilon(4S) \rightarrow B^+B^-) = 0.514 \pm 0.006$ and $\mathcal{B}(\Upsilon(4S) \rightarrow B^0\bar{B}^0) = 0.486 \pm 0.486$ [13]. The cross sections and luminosities assumed in the MC are corrected on an experiment-wise basis to the values determined from the hadronic events in the real data.

8.6. Hadronic Tag Correction

The largest necessary correction is the calibration of the hadronic tag reconstruction. The efficiencies of the `ekpfullrecon` tag is not reliably predicted by MC simulation, mainly because the branching fractions of the different hadronic channels are not accurate in the simulation. Hence, the hadronic tag must be calibrated on real data before use in a measurement.

There exists a default Belle tag calibration [50] for this purpose. However, since the default calibration uses $B \rightarrow D\ell\nu_\ell$ decays to derive its weights, it cannot be used in this analysis without introducing bias. I therefore derive my own correction which is based on inclusive semileptonic decays $B \rightarrow X\ell\nu_\ell$. The inclusive decay is not only well known, it also has a large data sample and thus minimizes statistical errors on the calibration.

I reconstruct the decay $B \rightarrow X\ell\nu_\ell$ in events with a hadronic tag and group the tag side into into 32 classes of the primary B_{tag} decay (17 charged and 15 neutral B decay modes). I further determine the correction factors in 15 different regions of o_{tag} by splitting $\log_{10}(o_{\text{tag}})$ into 15 equally sized bins between -3 and 0 in order to take into account efficiency dependence on tag quality.

8.6.1. $B \rightarrow X\ell\nu_\ell$ Reconstruction

I reconstruct decays $B \rightarrow X\ell\nu_\ell$ in events of the `xlnu_skim` by applying the following selection criteria:

- B_{tag} must satisfy $M_{\text{bc}} > 5.24 \text{ GeV}$ and $o_{\text{tag}} > 0.001$,
- e/μ impact parameters: $\Delta r < 0.5 \text{ cm}$ and $\Delta z < 2 \text{ cm}$,
- Lepton identification: $L_{\text{eid}} > 0.5$, $L_{\mu\text{id}} > 0.9$,
- Lepton momentum: $p_e > 0.3 \text{ GeV}$ and $p_\mu > 0.6 \text{ GeV}$ in the lab frame,
- Lepton polar angle: $17^\circ < \theta_e < 150^\circ$, $25^\circ < \theta_\mu < 145^\circ$ in the laboratory frame,
- Ratio of the second to the zeroth Fox-Wolfram moment $R_2 < 0.4$.

These cuts are identical to those used in the $B \rightarrow D\ell\nu_\ell$ reconstruction to ensure an environment as similar as possible.

8.6.2. Calibration Coefficients

In the next step, I divide the sample according to the 32 different hadronic tagging modes and into 15 regions of o_{tag} to account for different regions of tagging quality. In each sub-sample, I count the events available in real data and in the MC and calculate the correction coefficients. Their one dimensional projections for the B decay channels and o_{tag} can be seen in Figures 8.1 and 8.2.

8. MC Corrections

The statistical errors are calculated assuming a Poisson error on both the number of MC and real data events. The systematic errors are estimated via a toy-MC method described in section 9.1.

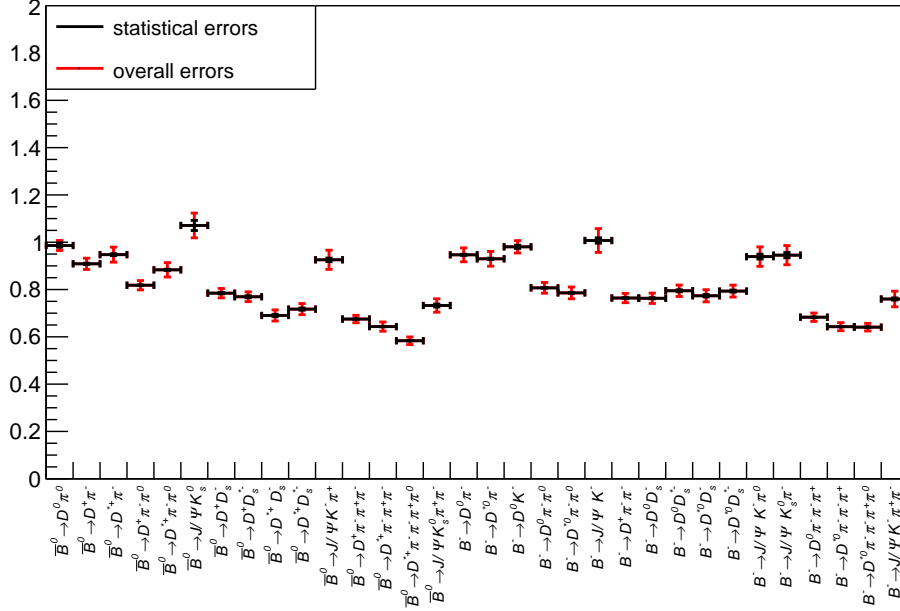


Figure 8.1.: Tag correction factors depending on the B_{tag} decay channel.

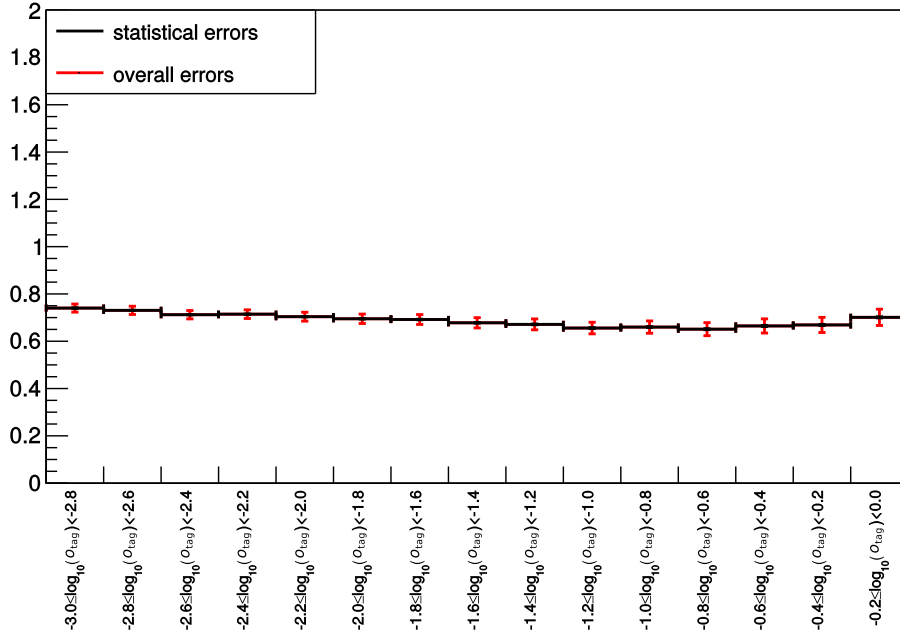


Figure 8.2.: Tag correction factors depending on o_{tag} .

8.6.3. Comparison of Real Data and MC for $B \rightarrow X\ell\nu_\ell$

In order to show the correct working of the tag calibration factors I compare the events reconstructed from real data and MC before and after the application of the resulting weights. Figure 8.3 shows the lepton momentum in the center of mass frame, the beam constrained mass of B_{tag} and $\log_{10}(\alpha_{\text{tag}})$ in the $B \rightarrow X\ell\nu_\ell$ sample. In the plots charged and neutral B meson events, and electron and muon events are combined.

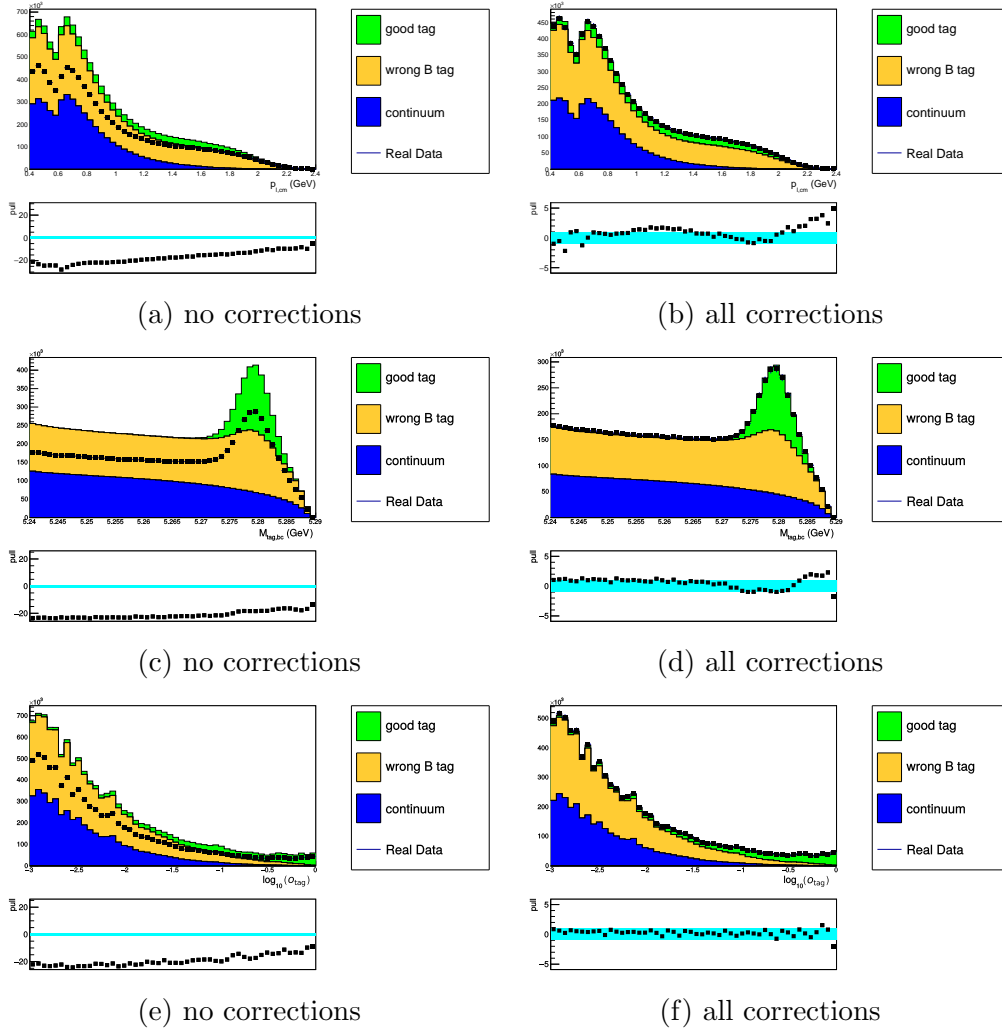


Figure 8.3.: MC and real data before (left) and after (right) applying all corrections used in this analysis on the $B \rightarrow X\ell\nu_\ell$ reconstruction. The given error includes the systematic error from the tag correction which is dominating. The lower sections of the plots show the pull values of the data points. The cyan band denotes $\pm 1\sigma$. The three components shown are (from top to bottom): genuinely reconstructed B_{tag} (good tag), wrongly assembled B_{tag} (wrong tag), and events without an $\Upsilon(4S)$ resonance (continuum).

8.7. Comparison of Real Data and MC

The correct working of the MC corrections mentioned so far can be verified by comparison with real data. This happened before complete box-opening and the signal region was thus excluded in the range $-0.3 \text{ GeV} < M_{\text{miss}}^2 < 0.5 \text{ GeV}$. Figure 8.4 shows the distributions of the parameters M_{miss}^2 , $p_{\ell, \text{lab}}$ and $\log_{10}(o_{\text{tag}})$ in the $B^+ \rightarrow \bar{D}^0 e^+ \nu_e$ sub-sample.

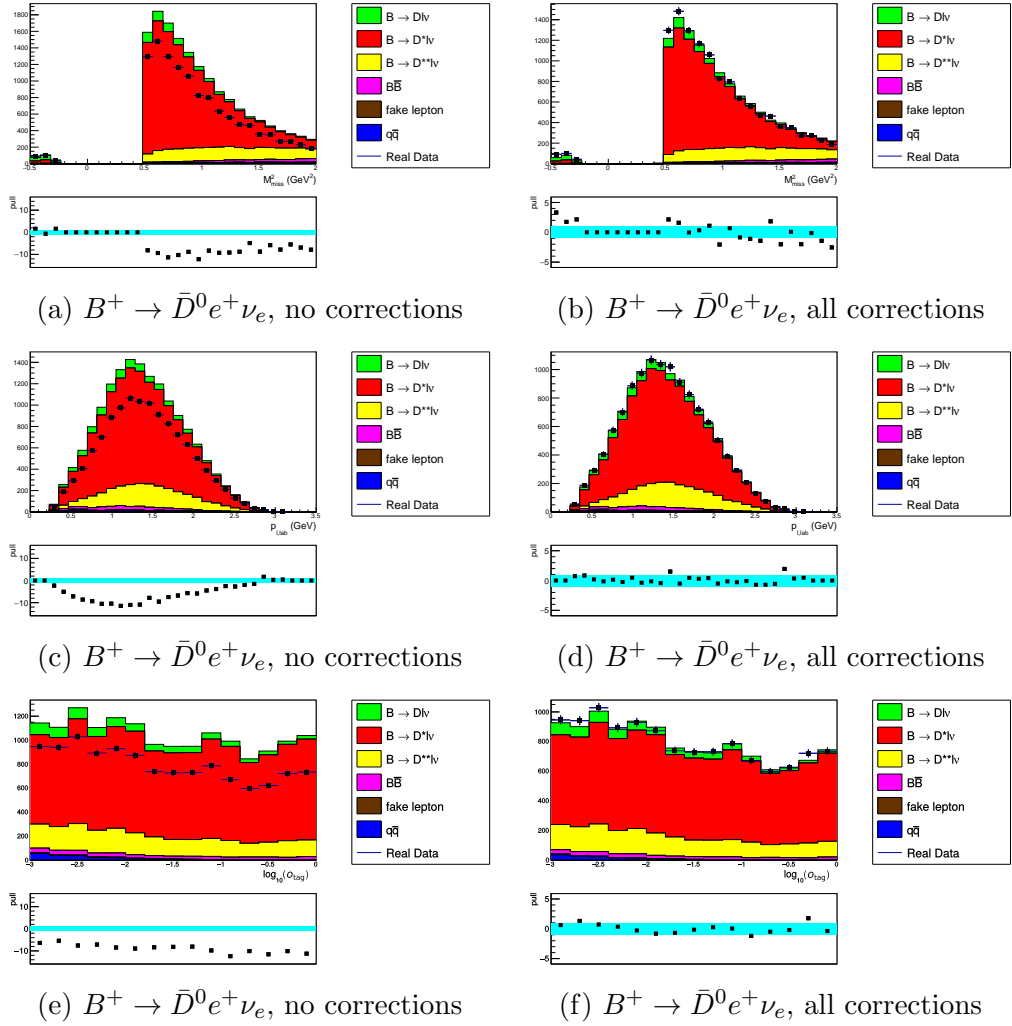


Figure 8.4.: MC and real data before (left) and after (right) application of corrections. Errors are statistical only. The lower sections of the plots show the pull values of the data points. The cyan band denotes $\pm 1\sigma$.

8.8. Signal Peak Resolution Correction

The $B \rightarrow D\ell\nu_\ell$ signal peak resolution in M_{miss}^2 as described by the MC is too narrow to describe the peak in real data². This can be seen for the sub-sample $B^0 \rightarrow D^-\mu^+\nu_\mu$ on the left side of Figure 8.5. The fit overestimates the signal yield in the bin at $M_{\text{miss}}^2 = 0$ and underestimates in the adjacent bins.

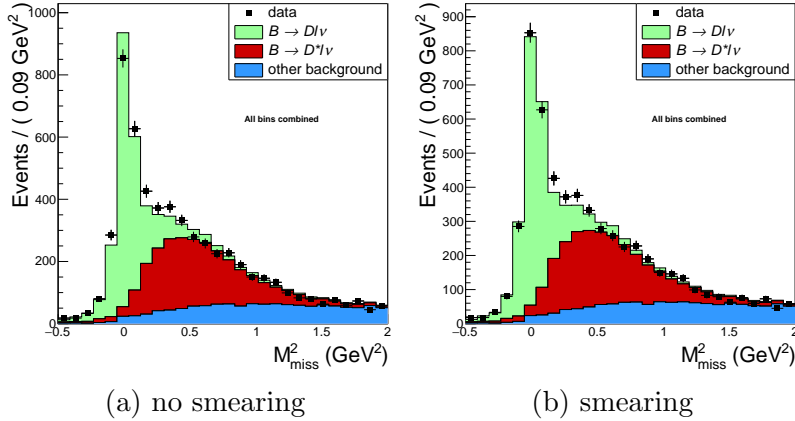


Figure 8.5.: Fitted yields combined over all w -bins for the sub-sample $B^0 \rightarrow D^-\mu^+\nu_\mu$. Figures on the left show the original fitted distribution if no smearing is applied and the right ones show the distributions when a Gaussian smearing is applied.

In order to correct the width of the signal peak I determine the signal-widths of MC and real data via the following procedure:

- I perform the signal yield fits in each w -bin using the original MC templates (without correction of the signal shape, but with all the other corrections mentioned throughout this chapter).
- The data from the 10 w -bins and the four sub-samples is added up to increase statistics³.
- The signal width in the MC can then be simply extracted by a Gaussian fit to the signal component.
- The signal component in the real data is deduced by subtracting the fitted background components from the measured real data. The resulting data is also fitted with a Gaussian curve.
- As the signal shape deviates from a Gaussian distribution in the tails only the core region of the signal components is fitted in the narrow region $-100 \text{ MeV}^2 \leq M_{\text{miss}}^2 \leq +100 \text{ MeV}^2$. The fit can be seen in Figure 8.6.

²Since this concerns the signal peak it is a correction that can only be determined after the box-opening.

³I verified that the results of separate fits yield compatible results within 1 standard deviation

8. MC Corrections

- The additional smearing needed to correct for the different widths in the MC is then $\sigma_{\text{add}} = \sqrt{\sigma_{\text{RD}}^2 - \sigma_{\text{MC}}^2}$.

The resulting necessary additional smearing is found to be $\sigma_{\text{add}} = 30 \pm 3.6 \text{ MeV}^2$. I apply this correction to the MC by drawing a random number for each measured M_{miss}^2 value from a Gaussian distribution with a mean value of the original M_{miss}^2 and a width of 30 MeV^2 . The result of applying this signal width correction can be seen on the right side of Figure 8.5. One can see that the shape description is improved with the additional smearing. As expected this also enhances the goodness of the signal yield extraction fits on real data.

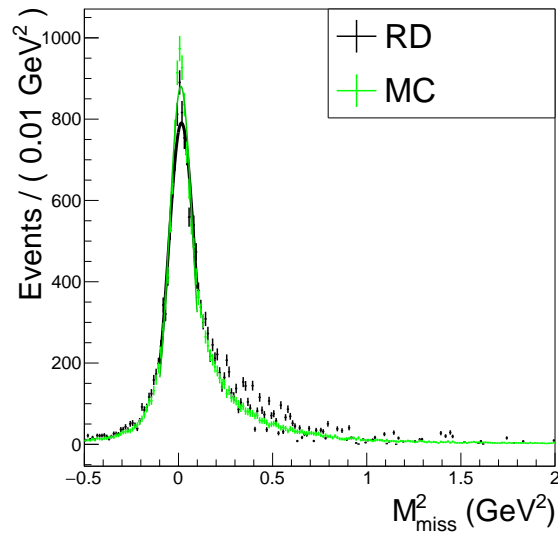


Figure 8.6.: Gaussian fits to the cores of the signal shape of MC and real data. Note that I use a finer binning of M_{miss}^2 than for the usual yield extraction fits to better resolve the shape.

9. Results

In this chapter I report the measured differential decay widths measured on real data and their systematic errors. The widths are presented separately from the $|V_{cb}|$ extraction to provide the basic data to averaging groups such as HFAG, which can then perform fits in combination with data from the BaBar experiment or with other theoretical assumptions such as different form factor parameterizations or electroweak corrections.

The signal yields are extracted with the method discussed in chapter 6. Selected fits in three w bins can be seen for the four sub-samples in Figures 9.1 - 9.4. The differential decay widths in the ten bins of each sample are then determined by:

$$\frac{\Delta\Gamma_i}{\Delta w} = \frac{\Delta\Gamma_{i,\text{MC}}}{\Delta w} \frac{\tau_{\text{MC}}}{\tau} \frac{N_i}{N_{i,\text{MC}}}, \quad i = 0, \dots, 9, \quad (9.1)$$

where $\Delta\Gamma_{i,\text{MC}}/\Delta w$ is the differential decay width of $B \rightarrow D\ell\nu_\ell$ in the i^{th} w -bin as simulated in the MC with the CLN form-factor parameterization:

$$\frac{\Delta\Gamma_{i,\text{MC}}}{\Delta w} = \frac{1}{\Delta w} \int_{w_{i,\text{min}}}^{w_{i,\text{max}}} \frac{d\Gamma_{\text{CLN}}}{dw} dw. \quad (9.2)$$

Here, $w_{i,\text{min}}$ and $w_{i,\text{max}}$ are the minimum and maximum boundary of the respective w -bin and $d\Gamma_{\text{CLN}}/dw$ is the differential width calculated with the MC form-factor parameters which I showed in Table 7.1 of section 7.3. The lifetime of B mesons as simulated in the MC is denoted as τ_{MC} and is $\tau_{\text{MC},B^+} = 1.654$ ps and $\tau_{\text{MC},B^0} = 1.534$ ps for B^+ and B^0 mesons respectively. τ denotes the corresponding lifetimes in real data determined most recently [13] as $\tau_{B^+} = 1.638$ ps and $\tau_{B^0} = 1.519$ ps. Finally, N_i is the measured $B \rightarrow D\ell\nu_\ell$ signal yield in the i^{th} bin of w , and $N_{i,\text{MC}}$ is the same quantity measured in the weighted MC simulation.

The resulting values of $\Delta\Gamma_i/\Delta w$ in the sub-samples ($B^+ \rightarrow \bar{D}^0 e^+ \nu_e$, $B^+ \rightarrow \bar{D}^0 \mu^+ \nu_\mu$, $B^0 \rightarrow D^- e^+ \nu_e$ and $B^0 \rightarrow D^- \mu^+ \nu_\mu$) are shown in Table 9.1 and show a good consistency across the sub-samples. The statistic errors result from the statistic uncertainties of the yield fits and the systematic errors and their correlations are calculated with the method described in section 9.1. The full systematic correlation matrix can be found in appendix C.

I calculate a weighted average of these differential rates for a combined sample with the generalized least squares method:

$$\Delta\Gamma_{\text{av}} = (\mathbf{X}^T \mathbf{C}_{\text{sub}}^{-1} \mathbf{X})^{-1} \mathbf{X}^T \mathbf{C}_{\text{sub}}^{-1} \Delta\Gamma_{\text{sub}}, \quad (9.3)$$

$$\mathbf{C}_{\text{av}} = (\mathbf{X}^T \mathbf{C}_{\text{sub}}^{-1} \mathbf{X})^{-1}. \quad (9.4)$$

9. Results

Here, $\Delta\Gamma_{\text{sub}}$ is a vector of 40 entries containing the decay widths of the subsamples and $\Delta\Gamma_{\text{av}}$ is the corresponding vector with 10 entries of the averaged sample. The full covariance matrices of the sub-samples and the average are denoted by \mathbf{C} and have size 40×40 and 10×10 respectively. Note, that due to the correlations of systematic errors the off-diagonal entries of the covariances are non-zero. Finally, \mathbf{X} is the 10×40 sized design matrix which basically consists of four 10×10 identity matrices. This average takes into account the full correlations and is unbiased and efficient. The resulting averages and their static and systematic errors including correlations are shown in Table 9.2.

i	$w_{i,\text{min}}$	$w_{i,\text{max}}$	$\Delta\Gamma_i/\Delta w$ [10^{-15}GeV]			
			$B^0 \rightarrow D^- e^+ \nu_e$	$B^0 \rightarrow D^- \mu^+ \nu_\mu$	$B^+ \rightarrow \bar{D}^0 e^+ \nu_e$	$B^+ \rightarrow \bar{D}^0 \mu^+ \nu_\mu$
0	1.00	1.06	$0.30 \pm 0.31 \pm 0.06$	$0.81 \pm 0.47 \pm 0.07$	$0.72 \pm 0.67 \pm 0.12$	$1.33 \pm 0.42 \pm 0.09$
1	1.06	1.12	$4.41 \pm 0.85 \pm 0.22$	$3.63 \pm 0.72 \pm 0.17$	$3.84 \pm 0.81 \pm 0.24$	$4.28 \pm 0.70 \pm 0.24$
2	1.12	1.18	$9.06 \pm 1.14 \pm 0.44$	$7.73 \pm 1.04 \pm 0.37$	$7.64 \pm 0.90 \pm 0.41$	$7.52 \pm 0.92 \pm 0.41$
3	1.18	1.24	$11.81 \pm 1.28 \pm 0.58$	$13.47 \pm 1.42 \pm 0.67$	$11.20 \pm 1.01 \pm 0.61$	$11.76 \pm 0.97 \pm 0.62$
4	1.24	1.30	$13.73 \pm 1.35 \pm 0.67$	$14.11 \pm 1.42 \pm 0.70$	$14.68 \pm 1.11 \pm 0.80$	$17.54 \pm 1.18 \pm 0.93$
5	1.30	1.36	$19.92 \pm 1.51 \pm 0.97$	$20.09 \pm 1.59 \pm 0.98$	$20.15 \pm 1.15 \pm 1.06$	$20.67 \pm 1.20 \pm 1.08$
6	1.36	1.42	$25.45 \pm 1.70 \pm 1.26$	$24.63 \pm 1.73 \pm 1.21$	$24.20 \pm 1.22 \pm 1.25$	$24.45 \pm 1.28 \pm 1.27$
7	1.42	1.48	$30.45 \pm 1.78 \pm 1.47$	$29.48 \pm 1.85 \pm 1.42$	$28.92 \pm 1.25 \pm 1.50$	$26.93 \pm 1.28 \pm 1.39$
8	1.48	1.54	$31.57 \pm 1.73 \pm 1.50$	$30.31 \pm 1.93 \pm 1.46$	$30.90 \pm 1.22 \pm 1.57$	$29.85 \pm 1.36 \pm 1.50$
9	1.54	w_{max}	$35.81 \pm 1.88 \pm 1.68$	$34.62 \pm 2.19 \pm 1.63$	$34.42 \pm 1.24 \pm 1.73$	$32.83 \pm 1.44 \pm 1.63$

Table 9.1.: $\Delta\Gamma_i/\Delta w$ measured in the four sub-samples with statistical and systematic uncertainties. The index i denotes the w -bin and $w_{i,\text{min}}$ and $w_{i,\text{max}}$ are the corresponding boundaries of the bin. I use $w_{\text{max}} = 1.59209$ for charged B meson decays and $w_{\text{max}} = 1.58901$ for neutral B meson channels. There is no correlation between the statistical errors. Correlations between the systematic errors can be seen in appendix C.

i	$w_{i,\text{min}}$	$w_{i,\text{max}}$	$\Delta\Gamma_i/\Delta w$ [10^{-15}GeV]	systematic correlations									
				0	1	2	3	4	5	6	7	8	9
0	1.00	1.06	$0.68 \pm 0.21 \pm 0.05$	1.000	0.682	0.677	0.663	0.654	0.656	0.664	0.648	0.608	0.560
1	1.06	1.12	$3.88 \pm 0.38 \pm 0.18$		1.000	0.976	0.974	0.969	0.972	0.972	0.961	0.933	0.900
2	1.12	1.18	$7.59 \pm 0.50 \pm 0.35$			1.000	0.991	0.987	0.990	0.989	0.980	0.959	0.929
3	1.18	1.24	$11.42 \pm 0.58 \pm 0.54$				1.000	0.993	0.993	0.990	0.980	0.961	0.934
4	1.24	1.30	$14.59 \pm 0.64 \pm 0.69$					1.000	0.996	0.992	0.985	0.972	0.952
5	1.30	1.36	$19.49 \pm 0.69 \pm 0.91$						1.000	0.996	0.991	0.979	0.956
6	1.36	1.42	$23.66 \pm 0.76 \pm 1.10$							1.000	0.995	0.981	0.952
7	1.42	1.48	$27.56 \pm 0.79 \pm 1.27$								1.000	0.992	0.968
8	1.48	1.54	$29.52 \pm 0.80 \pm 1.34$									1.000	0.985
9	1.54	w_{max}	$33.37 \pm 0.86 \pm 1.50$										1.000

Table 9.2.: The measured values of $\Delta\Gamma_i/\Delta w$ obtained by averaging the $B^+ \rightarrow \bar{D}^0 e^+ \nu_e$, $B^+ \rightarrow \bar{D}^0 \mu^+ \nu_\mu$, $B^0 \rightarrow D^- e^+ \nu_e$, and $B^0 \rightarrow D^- \mu^+ \nu_\mu$ sub-samples. From left to right the columns denote the w -bin number, the lower and upper boundary of the bin, the measured $\Delta\Gamma_i/\Delta w$ value with its statistical and systematic error. Finally, to the right the correlations between the systematic uncertainties are shown. The value of $w_{\text{max}} = 1.59055$ is obtained by averaging the respective values for charged and neutral B decays.

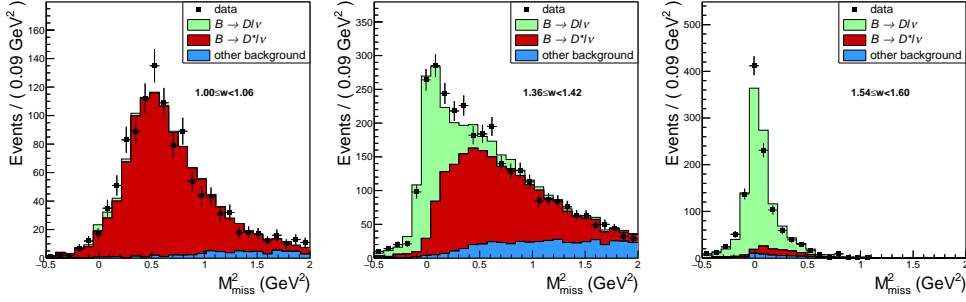


Figure 9.1.: Fit to the M_{miss}^2 distribution in three w bins for the $B^+ \rightarrow \bar{D}^0 e^+ \nu_e$ sub-sample. Points with error bars represent real data.

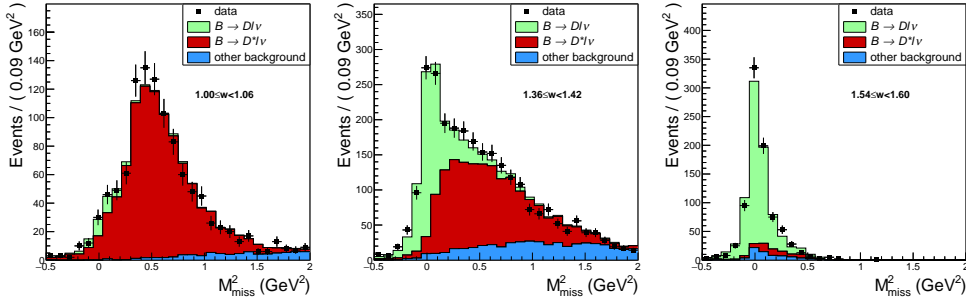


Figure 9.2.: Fit to the M_{miss}^2 distribution in three w bins for the $B^+ \rightarrow \bar{D}^0 \mu^+ \nu_\mu$ sub-sample. Points with error bars represent real data.

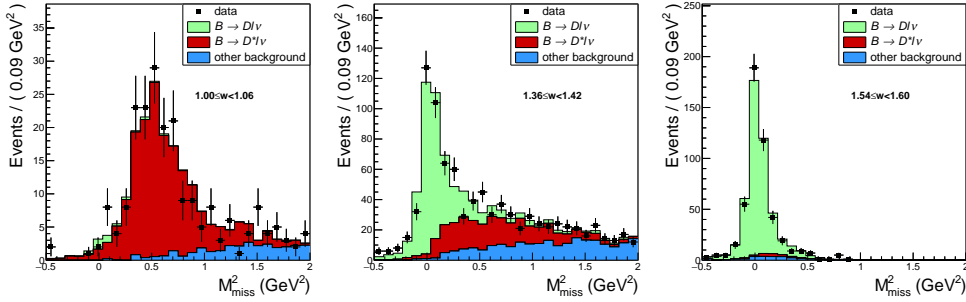


Figure 9.3.: Fit to the M_{miss}^2 distribution in three w bins for the $B^0 \rightarrow D^- e^+ \nu_e$ sub-sample. Points with error bars represent real data.

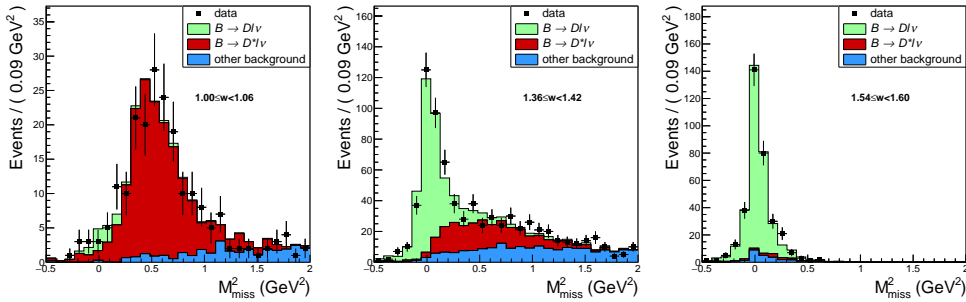


Figure 9.4.: Fit to the M_{miss}^2 distribution in three w bins for the $B^0 \rightarrow D^- \mu^+ \nu_\mu$ sub-sample. Points with error bars represent real data.

9. Results

The branching fractions corresponding to the measured differential decay widths can be calculated by summation and multiplication by the respective lifetimes:

$$\mathcal{B} = \tau_B \sum_i \Delta\Gamma_i . \quad (9.5)$$

where $\Delta\Gamma_i$ are the measured values of $\Delta\Gamma_i/\Delta w$ multiplied by the w width of the i^{th} bin. The results are shown in Table 9.3. There, I further present combined results based on the averaged differential decay widths. Note, that in order to present a combined branching fraction for charged and neutral B decays one has to select a specific lifetime and thus $\mathcal{B}(B \rightarrow D\ell\nu_\ell)$ is given in terms of the neutral B meson lifetime τ_{B^0} . The corresponding lifetime for charged B decays can be retrieved by multiplication with τ_{B^+}/τ_{B^0} .

Sample	Signal yield	\mathcal{B} [%]
$B^0 \rightarrow D^- e^+ \nu_e$	$2848 \pm 72 \pm 17$	$2.44 \pm 0.06 \pm 0.12$
$B^0 \rightarrow D^- \mu^+ \nu_\mu$	$2302 \pm 63 \pm 13$	$2.39 \pm 0.06 \pm 0.11$
$B^+ \rightarrow \bar{D}^0 e^+ \nu_e$	$6456 \pm 126 \pm 66$	$2.57 \pm 0.05 \pm 0.13$
$B^+ \rightarrow \bar{D}^0 \mu^+ \nu_\mu$	$5386 \pm 110 \pm 51$	$2.58 \pm 0.05 \pm 0.13$
$B^0 \rightarrow D^- \ell^+ \nu_\ell$	$5150 \pm 95 \pm 29$	$2.39 \pm 0.04 \pm 0.11$
$B^+ \rightarrow \bar{D}^0 \ell^+ \nu_\ell$	$11843 \pm 167 \pm 120$	$2.54 \pm 0.04 \pm 0.13$
$B \rightarrow D\ell\nu_\ell$	$16992 \pm 192 \pm 142$	$2.31 \pm 0.03 \pm 0.11$

Table 9.3.: Branching fractions of the decays $B^+ \rightarrow \bar{D}^0 e^+ \nu_e$, $B^+ \rightarrow \bar{D}^0 \mu^+ \nu_\mu$, $B^0 \rightarrow D^- e^+ \nu_e$, and $B^0 \rightarrow D^- \mu^+ \nu_\mu$. The branching fractions of $B^+ \rightarrow \bar{D}^0 \ell^+ \nu_\ell$ ($B^0 \rightarrow D^- \ell^+ \nu_\ell$) are the weighted averages of the $B^+ \rightarrow \bar{D}^0 e^+ \nu_e$ and $B^+ \rightarrow \bar{D}^0 \mu^+ \nu_\mu$ ($B^0 \rightarrow D^- e^+ \nu_e$ and $B^0 \rightarrow D^- \mu^+ \nu_\mu$) branching fraction results. The last row of the table corresponds to the branching fraction of all four sub-samples combined, expressed in terms of the neutral mode $B^0 \rightarrow D^- \ell^+ \nu_\ell$ assuming the lifetime $\tau_{B^0} = 1.519$ [13]. The first error on the yields and on the branching fractions is statistical. The second uncertainty is systematic.

9.1. Systematic Errors

There are multiple sources of systematic errors in this analysis, most come from the corrections mentioned in chapter 8. For example, hadronic D branching ratios are corrected to the latest measured values, but of course these values come with an experimental uncertainty. The precision of the hadronic tag correction on the other hand is both limited by the available data at Belle and by the other sources of systematic error impacting its measurement.

The propagation of those errors is non-trivial since they impact signal and background shapes in various ways and can depend on the kinematics and decay topologies. In order to realistically estimate the systematic errors, I therefore chose the approach of a toy Monte Carlo to determine both the magnitudes of the systematic uncertainties and their correlations. For every systematic error component I repeat the signal yield measurement procedure 1000 times. In each of those runs I vary the parameters in the MC simulation corresponding to the systematic error. *E.g.* when performing the toy-MC for the branching ratio corrections of the D mesons I vary each branching ratio within its experimental error. The run-dependent values are achieved by drawing a value from a Gaussian distribution with a mean of the measured value, and a standard deviation corresponding to the measurement error. This effect then propagates through the entire run until $\Delta\Gamma_i/\Delta w$ is measured. Over 1000 runs the measured $\Delta\Gamma_i/\Delta w$ values will thus scatter around a central value with a width σ_i corresponding to the systematic error caused by the component. The width can then be determined by a Gaussian fit.

The correlations $\rho_{i,j}$ between the $\Delta\Gamma_i/\Delta w$ values are then estimated as:

$$\rho_{i,j} = \frac{\langle (\frac{\Delta\Gamma_i}{\Delta w} - \langle \frac{\Delta\Gamma_i}{\Delta w} \rangle) (\frac{\Delta\Gamma_j}{\Delta w} - \langle \frac{\Delta\Gamma_j}{\Delta w} \rangle) \rangle}{\sqrt{\langle (\frac{\Delta\Gamma_i}{\Delta w} - \langle \frac{\Delta\Gamma_i}{\Delta w} \rangle)^2 \rangle} \sqrt{\langle (\frac{\Delta\Gamma_j}{\Delta w} - \langle \frac{\Delta\Gamma_j}{\Delta w} \rangle)^2 \rangle}}, \quad (9.6)$$

where the brackets denote averaging over the toy MC runs. In order to reduce the impact of outliers on the estimation of the correlation, I remove runs in which a $\Delta\Gamma_i/\Delta w$ value lies outside the range of three standard deviations around its fitted central value. The systematic covariance matrix for an error component is then given by:

$$C_{\text{syst}} = \rho_{i,j} \sigma_i \sigma_j \quad (9.7)$$

Finally, the full systematic error matrix combining all error sources is obtained by summing the respective single covariance matrices linearly, which is equivalent to quadratic error addition.

The systematic error components are:

- *Tag correction:* For all but the zeroth w bin the tag correction is the main source of systematic error. There are two components to the tagging error. First, the statistical error of the tag correction is due to the limited sample size of both MC and real data and is calculated based on the Poisson errors of the yields that enter into the weight calculations. Since these errors are statistically uncorrelated they are varied independently in the main toy MC. Second, the tag correction is subject to many of the systematic errors mentioned in the following. For this reason its systematic error is estimated by first performing a separate toy-MC for the tag correction following the same method just outlined, *i.e.* using 1000 toy-MC runs to determine the variation of the weights.

9. Results

While all discussed corrections are also applied to the $B \rightarrow X\ell\nu_\ell$ reconstruction (with the exception of the $B \rightarrow D\ell\nu_\ell$ signal peak width correction), only the following enter into its systematic error calculation: branching fractions, form factors and luminosities. Uncertainties concerning the signal side lepton (such as tracking and particle identification errors of the lepton) cancel with the respective error component in the $B \rightarrow D\ell\nu_\ell$ analysis. In the main toy-MC of $B \rightarrow D\ell\nu_\ell$ the thus determined systematic errors on the 480 correction weights are varied assuming a (conservative) correlation of 100 %.

- *Charged track reconstruction:* The track finding efficiency can be studied via $B \rightarrow D^*\ell\nu$ decays. As mentioned before, their signature is very clean. By studying partially (*i.e.* with a missing charged track) and fully reconstructed decay chains and comparing the resulting distributions in the MC and real data one can measure correction factors. The finding was, that the difference between real data and MC however, is much smaller than the error on those corrections which is in the order of 0.35 %. For this reason I do not apply a correction of charged track reconstruction efficiencies to the MC. In the toy-MC this results in weights with a central value of one, and an error of 0.35 % which is assumed as fully correlated between all charged tracks on the signal side with the exception of the lepton¹.
- *Branching fractions (\mathcal{B}) and form factors (FF):* As discussed in chapter 8 I correct the branching ratios of the decays $B \rightarrow D^*\ell\nu_\ell$, $B \rightarrow D^{**}\ell\nu_\ell$, $B \rightarrow X_u\ell\nu_\ell$, and of hadronic D meson decays. In the toy-MC the corresponding correction factors are varied independently by the experimental branching fraction errors. For the branching fractions of $B \rightarrow X_u\ell\nu_\ell$ I further vary the inclusive component, and for the $B \rightarrow X_u\ell\nu_\ell$ decays not well measured² I assume half the branching fraction used in the MC as uncertainty. The form factor corrections of $B \rightarrow D^*\ell\nu_\ell$ and $B \rightarrow D^{**}\ell\nu_\ell$ have both statistical errors which are varied independently and systematic errors which I again assume to be 100 % correlated.
- *Signal shape:* As discusses in section 8.8, I correct the shape of the $B \rightarrow D\ell\nu_\ell$ signal peak in the MC by smearing it by 30 MeV^2 . I vary this factor by the determined uncertainty of 3.6 MeV^2 . For most w bins the impact of this systematic component is minor. However, in the first bin the signal yield is so small that the impact on the shape contributes to a 5 % systematic error and is the dominating uncertainty there.

¹The errors on the charged track reconstruction of the lepton and of the tracks on the tag side cancel with the tag correction factors.

² $B \rightarrow X_u\ell\nu_\ell$ decays that are not well known but simulated in the MC include the decays with a a_0 , a_1 , a_2 , b_2 f_0 , f_1 , f_2 or h_1 meson.

- *B lifetime*: I use the lifetimes of the B^0 and B^+ meson in the extraction of the differential decay width as shown in equation. (9.1). The central values and uncertainties used in the toy-MC are $\tau(B^0) = 1.519 \pm 0.005$ ps and $\tau(B^+) = 1.638 \pm 0.004$ ps [13].
- *Particle identification*: The use of reconstructed $B \rightarrow X\ell\nu_\ell$ decays for tag calibration cancels the uncertainties in the identification of the charged lepton and on the tag side. The remaining particle identification errors come from the decay products of the D meson: charged kaons and pions, K_S^0 and π^0 particles. As described in section 8.4 the correction factors are determined by studying various clean decay channels and comparing mass distributions in real data and MC. The uncertainties on those fits are the source of this error component.
- *Luminosity*: This systematic error is due to the uncertainty on the Belle data luminosity which is estimated to be dominated by the errors on the luminosity measurement via Bhabha events and is estimated to be 1.4%. The further errors on the branching fractions of the $\Upsilon(4S)$ resonance are $\mathcal{B}(\Upsilon(4S) \rightarrow B^+B^-) = 0.514 \pm 0.006$ and $\mathcal{B}(\Upsilon(4S) \rightarrow B^0\bar{B}^0) = 0.486 \pm 0.486$ [13].

I list the determined relative systematic error contributions and the resulting total error for the combined data sample in Table 9.4, separately for the 10 w -bins. The suppression of the $B \rightarrow D\ell\nu_\ell$ signal at zero recoil results in the zeroth bin having the largest relative uncertainty.

	$\sigma(\Delta\Gamma_i/\Delta w)[\%]$									
	0	1	2	3	4	5	6	7	8	9
Tag correction	3.0	3.2	3.3	3.4	3.4	3.4	3.4	3.3	3.3	3.2
Charged tracks	1.7	1.6	1.6	1.6	1.6	1.6	1.6	1.6	1.6	1.6
$\mathcal{B}(D \rightarrow \text{hadronic})$	2.0	1.8	1.8	1.8	1.8	1.8	1.8	1.9	1.9	1.9
$\mathcal{B}(B \rightarrow D^{(*)}\ell\nu)$	1.3	0.8	0.8	0.9	0.8	0.7	0.5	0.2	0.2	0.4
$\mathcal{B}(B \rightarrow X_u\ell\nu)$	0.4	0.1	0.0	0.1	0.0	0.0	0.0	0.0	0.0	0.0
FF($B \rightarrow D^*\ell\nu$)	0.4	0.2	0.2	0.2	0.2	0.1	0.1	0.1	0.1	0.2
FF($B \rightarrow D^{**}\ell\nu$)	2.5	1.2	0.9	0.7	0.5	0.5	0.7	0.5	0.1	0.4
Signal shape	5.0	0.8	0.6	0.5	0.5	0.4	0.3	0.3	0.2	0.1
Lifetimes	0.2	0.2	0.2	0.2	0.2	0.2	0.2	0.2	0.2	0.2
π^0 efficiency	0.9	0.6	0.6	0.6	0.6	0.6	0.6	0.6	0.6	0.7
K/π efficiency	1.1	0.9	0.9	0.9	0.9	0.9	0.9	1.0	1.0	1.0
K_S^0 efficiency	0.4	0.2	0.2	0.2	0.2	0.2	0.2	0.2	0.2	0.2
Luminosity	1.4	1.4	1.5	1.4	1.4	1.4	1.4	1.4	1.4	1.4
Total	7.3	4.7	4.7	4.7	4.7	4.6	4.7	4.6	4.5	4.5

Table 9.4.: Components of the systematic uncertainty of the differential decay width in the different w -bins.

10. Discussion

In this chapter I will finally extract $|V_{cb}|$ from the differential decay widths presented in chapter 9. I use the two different form factor parameterizations CLN and BGL which I introduced in section 2.2.3. For the determination with CLN I further use the currently most precise measurement of $\mathcal{G}(1)$ by FNAL/MILC and for the BGL parameterization I use multiple form factor points derived in recent lattice QCD studies by the FNAL/MILC and HPQCD collaborations.

Both fits are based on the differential decay width formula derived in section 2.2:

$$\frac{d\Gamma}{dw} = \frac{G_F^2 m_D^3}{48\pi^3} (m_B + m_D)^2 (w^2 - 1)^{3/2} \eta_{EW}^2 |V_{cb}|^2 \mathcal{G}(w)^2 \quad (10.1)$$

10.1. CLN Parameterization Interpretation

The most common approach for measuring $|V_{cb}|$ from $B \rightarrow D\ell\nu_\ell$ in the literature is the CLN form-factor parameterization which I discussed in section 2.2.3. It parameterizes $\mathcal{G}(w)$ with the form factor at zero recoil $\mathcal{G}(1)$ and the so-called slope parameter ρ^2 :

$$z(w) = \frac{\sqrt{w+1} - \sqrt{2}}{\sqrt{w+1} + \sqrt{2}} \quad (10.2)$$

$$\mathcal{G}(z) = \mathcal{G}(w=1)(1 - 8\rho^2 z + (51\rho^2 - 10)z^2 - (252\rho^2 - 84)z^3). \quad (10.3)$$

Since $\mathcal{G}(1)$ is simply a multiplicative factor that normalizes the decay width, the fit of experimental data leaves it undetermined and instead measures $\eta_{EW}\mathcal{G}(1)|V_{cb}|$. This value is then divided by $\mathcal{G}(1)$ as determined by theoretical calculations.

To extract $\eta_{EW}\mathcal{G}(1)|V_{cb}|$ I perform a χ^2 fit, minimizing the function

$$\chi^2 = \sum_{i,j} \left(\frac{\Delta\Gamma_i}{\Delta w} - \frac{\Delta\Gamma_{i,CLN}}{\Delta w} \right) \mathbf{C}_{ij}^{-1} \left(\frac{\Delta\Gamma_j}{\Delta w} - \frac{\Delta\Gamma_{j,CLN}}{\Delta w} \right). \quad (10.4)$$

Here, $\Delta\Gamma_i/\Delta w$ is the measured differential decay width presented in Tables 9.1 (for the sub-samples) and 9.2 (for the combined sample). $\Delta\Gamma_{i,CLN}/\Delta w$ is the differential decay width calculated with the CLN form-factor parameterization of equation 10.3 and the general differential decay width formula of equation 10.1, as:

$$\frac{\Delta\Gamma_{i,CLN}}{\Delta w}(\eta_{EW}\mathcal{G}(1)|V_{cb}|, \rho^2) = \frac{1}{\Delta w} \int_{w_{i,\min}}^{w_{i,\max}} \frac{d\Gamma_{CLN}}{dw} dw. \quad (10.5)$$

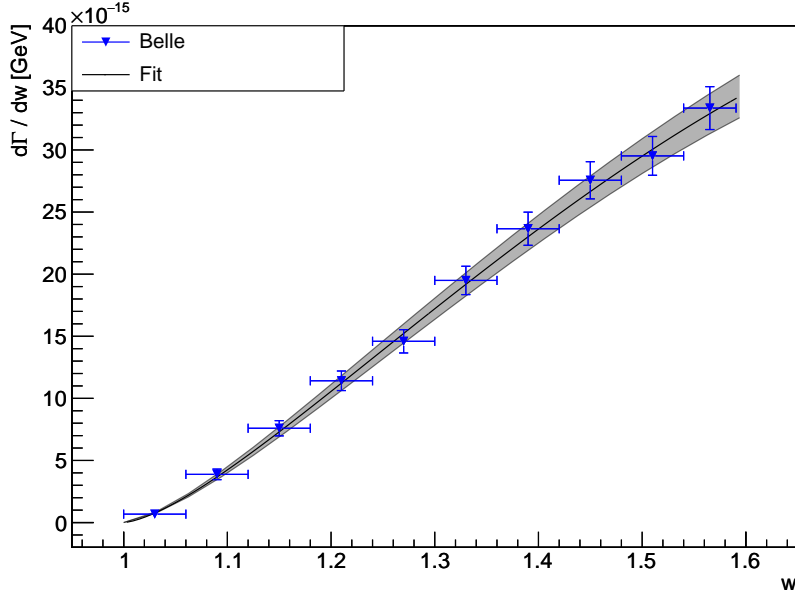


Figure 10.1.: Fit of the measured $\Delta\Gamma_i/\Delta w$ values of the decay $B \rightarrow D\ell\nu_\ell$ using the CLN form-factor parameterization. The blue points represent the measured decay widths and their vertical error bars correspond to their total uncertainties, while their horizontal error bars indicate the bin width. The result of the fit is shown as solid black curve with the shaded area corresponding to the uncertainty in the fit parameters.

The free parameters of the fit are $\eta_{EW}\mathcal{G}(1)|V_{cb}|$ and ρ^2 resulting in 8 degrees of freedom (n_{df}). \mathbf{C} denotes the total covariance matrix and is the sum of the diagonal statistical covariance matrix and the (in general not diagonal) systematic covariance matrix. Additional to the fit on the combined sample I also fit the single sub-samples. In the single fits I use the nominal B and D meson mass values $m_B^+ = 5.27926$ GeV, $m_B^0 = 5.27958$ GeV, $m_D^+ = 1.86961$ GeV and $m_D^0 = 1.86484$ GeV, and in the combined fit I use the averages $m_B = 5.27942$ GeV and $m_D = 1.86725$ GeV.

Figure 10.1 shows the result of the fit on the combined sample. The resulting values of $\eta_{EW}\mathcal{G}(1)|V_{cb}|$ and ρ^2 can be seen in Table 10.1 and Figure 10.2, separately for the combined sample and the four sub-samples. Using the currently most precise form-factor at zero recoil found in reference [16]

$$\mathcal{G}(1) = 1.0541 \pm 0.0083, \quad (10.6)$$

results thus in a value of $\eta_{EW}|V_{cb}| = (40.12 \pm 1.34) \times 10^{-3}$. Using the Sirlin factor for electroweak correction of $\eta_{EW} = 1.0066 \pm 0.0016$ [17] this leads to $|V_{cb}| = 39.86 \pm 1.33$.

10. Discussion

	$B^+ \rightarrow D^0 e^+ \nu_e$	$B^+ \rightarrow D^0 \mu^+ \nu_\mu$	$B^0 \rightarrow D^- e^+ \nu_e$	$B^0 \rightarrow D^- \mu^+ \nu_\mu$	$B \rightarrow D \ell \nu_\ell$
$\eta_{\text{EW}} \mathcal{G}(1) V_{cb} [10^{-3}]$	42.31 ± 1.94	45.48 ± 1.96	41.84 ± 2.14	42.99 ± 2.18	42.29 ± 1.37
ρ^2	1.05 ± 0.08	1.22 ± 0.07	1.01 ± 0.10	1.08 ± 0.10	1.09 ± 0.05
Correlation	0.81	0.77	0.85	0.84	0.69
$\eta_{\text{EW}} V_{cb} [10^{-3}]$	40.14 ± 1.86	43.15 ± 1.89	39.69 ± 2.05	40.78 ± 2.09	40.12 ± 1.34
χ^2/n_{df}	2.19/8	2.71/8	9.65/8	4.36/8	4.57/8
Prob.	0.97	0.95	0.29	0.82	0.80

Table 10.1.: The results of the CLN form-factor fit to the measured differential decay width. “Correlation” is the measured correlation between the total uncertainties of $\eta_{\text{EW}} \mathcal{G}(1) |V_{cb}|$ and ρ^2 .

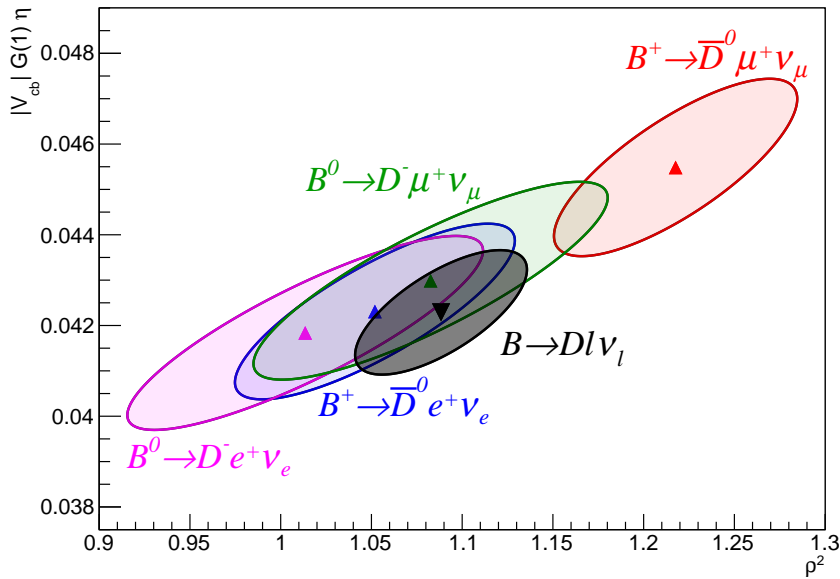


Figure 10.2.: Values for $\eta_{\text{EW}} \mathcal{G}(1) |V_{cb}|$ and ρ^2 measured with CLN form-factor fits for the four sub-samples and the combined sample. The ellipses show the area of one standard deviation.

10.2. Model-Independent BGL Fit

As discussed in section 2.2.3 the BGL parameterization is a model-independent parameterization not relying on HQET constraints and is thus more general than CLN and has subsequently more free parameters. Recently two papers have been published by FNAL/MILC [16] and HPQCD [26] that include form factors at points other than zero recoil. Together with the large amount of $B \rightarrow D\ell\nu_\ell$ decays in this analysis this makes a combined fit of the averaged data sample and the lattice data feasible.

With the choice of outer function from reference [16] the relevant formulae are:

$$f_i(z) = \frac{1}{\phi_i(z)} \sum_{n=0}^N a_{i,n} z^n, \quad i = +, 0 \quad (10.7)$$

$$f_+(w)^2 = \frac{\left(1 + \frac{m_D}{m_B}\right)^2}{4 \frac{m_D}{m_B}} \mathcal{G}(w)^2 \quad (10.8)$$

$$\phi_+(z) = 1.1213(1+z)^2(1-z)^{1/2}[(1+r)(1-z) + 2\sqrt{r}(1+z)]^{-5} \quad (10.9)$$

$$\phi_0(z) = 0.5299(1+z)(1-z)^{3/2}[(1+r)(1-z) + 2\sqrt{r}(1+z)]^{-4} \quad (10.10)$$

$$\sum_{n=0}^N |a_{i,n}|^2 \leq 1 \quad (10.11)$$

$$f_0(w_{\max}) = f_+(w_{\max}). \quad (10.12)$$

Note, that the kinematic constraint (equation 10.12) links both form factors and thus allows an inclusion of f_0 data from lattice QCD to enter the combined fit¹. I implement the kinematic constraint by expressing the parameter $a_{0,0}$ with the other coefficients:

$$f_0(w_{\max}) = f_+(w_{\max}) \quad (10.13)$$

$$\frac{1}{\phi_0(z_{\max})} \sum_{n=0}^N a_{0,n} z_{\max}^n = \frac{1}{\phi_+(z_{\max})} \sum_{n=0}^N a_{+,n} z_{\max}^n \quad (10.14)$$

$$a_{0,0} = \phi_0(z_{\max}) \left[\frac{1}{\phi_+(z_{\max})} \sum_{n=0}^N a_{+,n} z_{\max}^n - \frac{1}{\phi_0(z_{\max})} \sum_{n=1}^N a_{0,n} z_{\max}^n \right]. \quad (10.15)$$

¹The resulting improvement of the precision however, is rather small and only fitting f_+ would yield almost similar errors. The main reason to include f_0 data is the ease of comparison with similar fits on BaBar data performed in reference [16].

10. Discussion

As in the previous section I perform a fit by minimizing the χ^2 value:

$$\begin{aligned} \chi^2 = & \sum_{i,j} \left(\frac{\Delta\Gamma_i}{\Delta w} - \frac{\Delta\Gamma_{i,\text{BGL}}}{\Delta w} \right) \mathbf{C}_{ij}^{-1} \left(\frac{\Delta\Gamma_j}{\Delta w} - \frac{\Delta\Gamma_{j,\text{BGL}}}{\Delta w} \right) \\ & + \sum_{k,l} \left(f_{+,0}^{\text{LQCD}}(w_k) - f_{+,0}^{\text{BGL}}(w_k) \right) \mathbf{D}_{kl}^{-1} \left(f_{+,0}^{\text{LQCD}}(w_l) - f_{+,0}^{\text{BGL}}(w_l) \right). \end{aligned} \quad (10.16)$$

The differential decay width values $\Delta\Gamma_i/\Delta w$ are taken from the combined sample presented in Table 9.2 and $\Delta\Gamma_{i,\text{BGL}}/\Delta w$ is the corresponding differential decay width calculated with the BGL parameterization:

$$\frac{\Delta\Gamma_{i,\text{BGL}}}{\Delta w}(\eta_{\text{EW}}|V_{cb}|, a_{+,n}) = \frac{1}{\Delta w} \int_{w_{i,\text{min}}}^{w_{i,\text{max}}} \frac{d\Gamma_{\text{BGL}}}{dw} dw. \quad (10.17)$$

The covariance matrix \mathbf{C} is again the sum of the statistical and systematic error matrices of the measured differential decay widths. The second sum contains the LQCD data included in the fit and \mathbf{D} is the corresponding total covariance matrix. Note that the second sum implicitly runs over both f_+ and f_0 and over the different lattice QCD measurements which I will discuss in the following.

The lattice data used in the fit stems from recent measurement by the FNAL/MILC [16] and HPQCD [26] collaborations. The errors on their form factors are dominated by systematics. Both collaborations use different methods of describing heavy quarks on the lattice: lattice non relativistic QCD [51] for the HPQCD measurement, and the Fermilab method [52] for the FNAL/MILC measurement. Their systematic errors can thus be considered mostly uncorrelated and I will assume no correlations between the two measurements in the combined fit.

The values obtained by FNAL/MILC consist of f_+ and f_0 form factors each at $w = 1, 1.08, 1.16$ (in total six data points). These values and the corresponding covariance matrix can be found in Table VII of reference [16].

HPQCD presented their form factors in a parameterization that I have not mentioned so far. The Bourrely, Caprini and Lellouch (BCL) [53] parameterization is – like the BGL parameterization – model independent, but is based on a different expansion in a conformal mapping variable and aims at offering perturbative QCD scaling at higher q^2 values. The values measured by HPQCD in the BCL parametrization together with the used equations and pole choices can be found in appendix A of reference [26]. They provide six coefficients of the parametrization $a_0^{(0)}$, $a_1^{(0)}$, $a_2^{(0)}$, $a_0^{(+)}$, $a_1^{(+)}$, and $a_2^{(+)}$, and a corresponding covariance matrix.

In order to perform a combined fit in the BGL parameterization I transform these values into 6 form factor measurements at the same w values used by FNAL/MILC:

$$\begin{pmatrix} f_0(1) \\ f_0(1.08) \\ f_0(1.16) \\ f_+(1) \\ f_+(1.08) \\ f_+(1.16) \end{pmatrix} = \mathbf{M} \begin{pmatrix} a_0^{(0)} \\ a_1^{(0)} \\ a_2^{(0)} \\ a_0^{(+)} \\ a_1^{(+)} \\ a_2^{(+)} \end{pmatrix}. \quad (10.18)$$

Here, \mathbf{M} is a 6×6 matrix which performs the linear transformation from the parameters to the form factors. The resulting covariance matrix $\mathbf{D}_{\text{HPQCD},f}$ is then

$$\mathbf{D}_{\text{HPQCD},f} = \mathbf{M} \mathbf{D}_{\text{HPQCD},a} \mathbf{M}^T. \quad (10.19)$$

I present the resulting form factor values and their correlations in Table 10.2.

	Central value	Correlations					
		$f_+(1)$	$f_+(1.08)$	$f_+(1.16)$	$f_0(1)$	$f_0(1.08)$	$f_0(1.16)$
$f_+(1)$	1.178 ± 0.046	1.000	0.989	0.954	0.507	0.518	0.525
$f_+(1.08)$	1.082 ± 0.041		1.000	0.988	0.582	0.600	0.615
$f_+(1.16)$	0.996 ± 0.037			1.000	0.650	0.676	0.698
$f_0(1)$	0.902 ± 0.041				1.000	0.995	0.980
$f_0(1.08)$	0.860 ± 0.038					1.000	0.995
$f_0(1.16)$	0.821 ± 0.036						1.000

Table 10.2.: Form factor values calculated from the parameters of the BCL parameterization measured by HPQCD [26].

The result of the combined fit can be seen for different truncation orders N in Table 10.3. While the quadratic fit automatically respects the unitarity bound from equation 10.11, higher order parameters need to be constrained. I implement this requirement by following the method of [16] and constrain higher order coefficients by adding the measurement points $a_{i,n \geq 3} = 0 \pm 1$ to the χ^2 function. This results in a constant number of degrees of freedom as can be seen in Table 10.3.

For the quadratic truncation order the fit is not stable, *i.e.* repetition with small changes yield widely different results. The reason for this are the high correlations between the lattice QCD data points. One way of circumventing the problem is to remove one of the form factor points from each collaboration resulting in a more stable fit. The fit also stabilizes for higher truncation orders, which is the method chosen here. Already at $N \geq 3$, the goodness of fit values become reasonable and tests with slightly different input parameters have not lead to significant deviations. Since higher truncation orders have no further impact² on the measured coefficients or $\eta_{\text{EW}}|V_{cb}|$, I choose $N = 3$ as the preferred fit.

²I verified that this is indeed the case for up to $N = 7$.

10. Discussion

The fit for $N = 3$ shown for the differential decay width can be seen in Figure 10.3. Figure 10.4 shows the fit in terms of the form factors. The final result for $\eta_{EW}|V_{cb}|$ based on the combined fit to Belle data and lattice QCD values from HPQCD and FNAL/MILC is thus $(41.10 \pm 1.14) \times 10^{-3}$. With the Sirlin factor as electroweak correction this leads to $|V_{cb}| = (40.83 \pm 1.13) \times 10^{-3}$. Comparing this value to the one derived with the CLN parameterization one sees an improvement in the precision from 3.3% to 2.8%. This improvement is the result of the additional input from further lattice points. Note however, that due to the high correlations among the lattice points only two form factor values from each collaboration would achieve similar precisions. It seems, that without a reduction of the correlations between lattice points, any number exceeding two has only minor benefits.

I have verified the stability of the resulting $\eta_{EW}|V_{cb}|$ value by repeating the combined fit with only subsets of the lattice data. Table 10.4 shows the comparison of including only a single collaboration. The differences are well below one standard deviation.

	$N = 2$	$N = 3$	$N = 4$
$a_{+,0}$	0.0127 ± 0.0001	0.0126 ± 0.0001	0.0126 ± 0.0001
$a_{+,1}$	-0.091 ± 0.002	-0.094 ± 0.003	-0.094 ± 0.003
$a_{+,2}$	0.34 ± 0.03	0.34 ± 0.04	0.34 ± 0.04
$a_{+,3}$	–	-0.1 ± 0.6	-0.1 ± 0.6
$a_{+,4}$	–	–	0.0 ± 1.0
$a_{0,0}$	0.0115 ± 0.0001	0.0115 ± 0.0001	0.0115 ± 0.0001
$a_{0,1}$	-0.058 ± 0.002	-0.057 ± 0.002	-0.057 ± 0.002
$a_{0,2}$	0.22 ± 0.02	0.12 ± 0.04	0.12 ± 0.04
$a_{0,3}$	–	0.4 ± 0.7	0.4 ± 0.7
$a_{0,4}$	–	–	0.0 ± 1.0
$\eta_{EW} V_{cb} $	40.01 ± 1.08	41.10 ± 1.14	41.10 ± 1.14
χ^2/n_{df}	24.7/16	11.4/16	11.3/16
Prob.	0.075	0.787	0.787

Table 10.3.: Results of the fit of combined data in the BGL parameterization. Shown are the truncation orders $N = 2, 3, 4$. The value presented for $a_{0,0}$ does not result directly from the fit but is determined from the other parameters via the kinematic constraint.

Lattice data	$\eta_{EW} V_{cb} [10^{-3}]$	χ^2/n_{df}	Prob.
FNAL/MILC [16]	40.96 ± 1.23	6.01/10	0.81
HPQCD [26]	41.14 ± 1.88	4.83/10	0.90
FNAL/MILC & HPQCD [26, 16]	41.10 ± 1.14	11.35/16	0.79

Table 10.4.: Comparison of combined fits with different sets of lattice data. The BGL parameterization was truncated at $N = 3$.

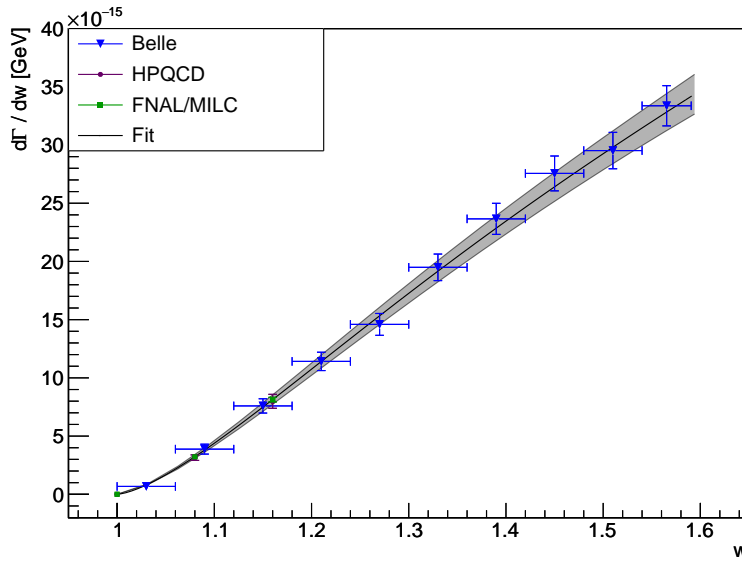


Figure 10.3.: Result of the combined fit for the differential decay width. The BGL parameterization was truncated at $N = 3$. Belle and LQCD data are shown as points with error bars. Vertical bars indicate uncertainties and horizontal bars indicate the bin width. The fit result is shown as solid curve, the shaded area shows the uncertainty in the fit parameters.

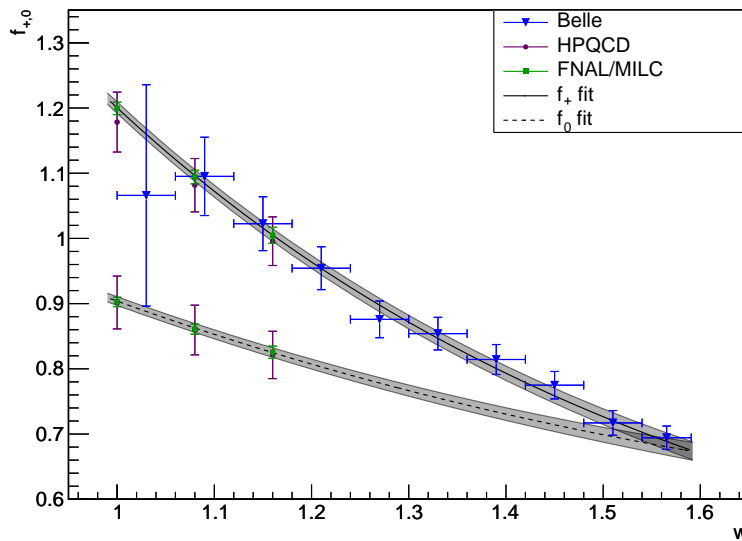


Figure 10.4.: Result of the combined fit for the form factors f_0 and f_+ . The BGL parameterization was truncated at $N = 3$. Belle and LQCD data are shown as points with error bars. Vertical bars indicate uncertainties and horizontal bars indicate the bin width. The f_+ form factor fit result is shown as solid curve, the shaded area shows the uncertainty in the fit parameters. The f_0 form factor is shown as dashed curve.

11. Summary

I presented a study of the decay $B \rightarrow D\ell\nu_\ell$ with the full Belle data sample at the $\Upsilon(4S)$ resonance, containing 772 million $B\bar{B}$ events. The differential decay widths were measured in the four sub-samples $B^+ \rightarrow \bar{D}^0 e^+ \nu_e$, $B^+ \rightarrow \bar{D}^0 \mu^+ \nu_\mu$, $B^0 \rightarrow D^- e^+ \nu_e$, and $B^0 \rightarrow D^- \mu^+ \nu_\mu$, in ten different bins of the kinematic variable $w = v_{B\mu} v_D^\mu$. Averaged values were calculated taking into account the full correlations between bins and sub-samples. The branching ratios were determined in each of the 4 sub-samples and the combined branching fraction (in terms of neutral B mesons) was found to be $\mathcal{B}(B^0 \rightarrow D^- \ell^+ \nu_\ell) = (2.31 \pm 0.03(\text{stat}) \pm 0.11(\text{syst}))\%$.

I interpreted the measured combined differential decay width spectrum with two different methods. First, I used the CLN form-factor parameterization which utilizes HQET constraints, and the measurement of the form factor at zero recoil from the FNAL/MILC collaboration [16] to extract a value of $\eta_{\text{EW}}|V_{cb}| = (40.12 \pm 1.34) \times 10^{-3}$. Second, I used the model independent BGL form-factor parameterization, and multiple form-factor data points from the FNAL/MILC [16] and HPQCD [26] collaborations to find $\eta_{\text{EW}}|V_{cb}| = (41.10 \pm 1.14) \times 10^{-3}$. The dominant reason for the shifted central value and the increased precision comes from the addition of lattice data points at non-zero recoil.

These results supersede the previous $B \rightarrow D\ell\nu_\ell$ measurement at Belle [23] and are currently the most precise values for the differential decay width and $|V_{cb}|$ from the decay $B \rightarrow D\ell\nu_\ell$. I reconstructed about five times the amount of $B \rightarrow D\ell\nu_\ell$ decays as measured by BaBar [22] resulting in an improved precision of $|V_{cb}|$ from $B \rightarrow D\ell\nu_\ell$ to 2.8%. Compared with the values found by BaBar, $|V_{cb}|$ is very compatible, while the branching fractions derived here are higher, yet still compatible. In terms of the inclusive-exclusive discrepancy between $|V_{cb}|$ from $B \rightarrow X_c \ell \nu_\ell$ [28] and $B \rightarrow D^* \ell \nu_\ell$ [19, 20], the $|V_{cb}|$ values found here fall into the middle, not clearly favoring either of the two values.

Future developments on the theoretical side will include improved lattice QCD calculations and more measurements with form-factor values at non-zero recoil further reducing the respective uncertainty in the $|V_{cb}|$ determination.

The results shown in this thesis will be included in the next world averages of $|V_{cb}|$ and the increasing role of combined fits of experimental and lattice data might lead to the next averages being based on such a fit combining data from from BaBar, Belle and lattice groups.

With the increased precision, it becomes increasingly important for the averaging groups to decide on a common electroweak correction factor which takes into account terms higher than those provided by the Sirlin correction. The future might also see $|V_{cb}|$ determinations from non B Factory experiments such as LHCb, although with limited precision.

With the completion of this analysis the data samples at B Factories for $|V_{cb}|$ measurements are mostly exhausted and further precise studies will only be possible once the Belle II experiment has collected data. Then, studies of $B \rightarrow D^* \ell \nu_\ell$ and $B \rightarrow D \ell \nu_\ell$ for the determination of $|V_{cb}|$ can be expected. Belle II will increase the data sample by a factor of 50 and thus greatly reduce the statistical error in the measurement. One can also expect smaller systematics in those measurements, since numerous sources of systematics depend on the size of the available data sample. Further, external uncertainties such as branching ratios and lifetimes will have been measured with higher precision, further reducing systematic errors. However, for the foreseeable future Belle II will be the only B Factory experiment and thus a confirmation by a second experiment will be challenging. This raises the question, how the particle physics community will deal with precision B -physics and CKM element measurements in the future.

A. Figure of Merit of D Decay Channels

In order to show that the D decay channels used in this analysis have a positive impact on the figure of merit I exclude each channel at a time from the reconstruction and determine the resulting F.O.M. in the signal region in the respective sub-sample. The results can be seen in Table A.1. One can see that removal of each of the channels would cause a reduction in the F.O.M, and that the best contributions come from only a few channels: $D^+ \rightarrow K^- \pi^+ \pi^+$, $D^0 \rightarrow K^- \pi^+$, $D^0 \rightarrow K^- \pi^+ \pi^0$ and $D^0 \rightarrow K^- \pi^+ \pi^+ \pi^-$.

sub-sample / excluded channel	entire range		signal region		Δ F.O.M.
	signal	background	signal	background	
in sub-sample $B^+ \rightarrow \bar{D}^0 e^+ \nu_e$:	7567	23166	6144	4272	
$D^0 \rightarrow K^- \pi^+$	5796	17836	4635	3316	-13.7%
$D^0 \rightarrow K^- \pi^+ \pi^0$	5588	17092	4545	3126	-13.8%
$D^0 \rightarrow K^- \pi^+ \pi^+ \pi^-$	5676	17667	4571	3269	-14.3%
$D^0 \rightarrow K_s^0 \pi^+ \pi^-$	7080	21795	5738	4026	-3.5%
$D^0 \rightarrow K_s^0 \pi^+ \pi^- \pi^0$	7291	22343	5928	4120	-1.8%
$D^0 \rightarrow K_s^0 \pi^0$	7409	22709	6017	4189	-1.1%
$D^0 \rightarrow K^+ K^-$	7370	22613	5991	4165	-1.3%
$D^0 \rightarrow \pi^+ \pi^-$	7495	22907	6084	4219	-0.4%
$D^0 \rightarrow K_s^0 K^0$	7563	23157	6140	4270	-0.0%
$D^0 \rightarrow \pi^0 \pi^0$	7548	23111	6131	4262	-0.1%
$D^0 \rightarrow K_s^0 \pi^0 \pi^0$	7524	23019	6113	4243	-0.2%
$D^0 \rightarrow K^- \pi^+ \pi^+ \pi^- \pi^0$	7319	22301	5965	4083	-1.2%
$D^0 \rightarrow \pi^+ \pi^- \pi^0$	7146	21522	5864	3970	-1.8%
in sub-sample $B^+ \rightarrow \bar{D}^0 \mu^+ \nu_\mu$:	6319	20935	5443	4479	
$D^0 \rightarrow K^- \pi^+$	4832	16215	4108	3481	-13.7%
$D^0 \rightarrow K^- \pi^+ \pi^0$	4640	15457	4012	3271	-14.0%
$D^0 \rightarrow K^- \pi^+ \pi^+ \pi^-$	4772	16109	4076	3439	-13.9%
$D^0 \rightarrow K_s^0 \pi^+ \pi^-$	5904	19705	5075	4224	-3.7%
$D^0 \rightarrow K_s^0 \pi^+ \pi^- \pi^0$	6083	20160	5250	4315	-1.8%
$D^0 \rightarrow K_s^0 \pi^0$	6190	20542	5328	4395	-1.1%
$D^0 \rightarrow K^+ K^-$	6174	20432	5319	4367	-1.1%
$D^0 \rightarrow \pi^+ \pi^-$	6253	20684	5385	4424	-0.5%
$D^0 \rightarrow K_s^0 K^0$	6314	20925	5438	4477	-0.1%
$D^0 \rightarrow \pi^0 \pi^0$	6307	20882	5435	4470	-0.1%
$D^0 \rightarrow K_s^0 \pi^0 \pi^0$	6280	20785	5414	4447	-0.2%
$D^0 \rightarrow K^- \pi^+ \pi^+ \pi^- \pi^0$	6096	20132	5270	4297	-1.4%
$D^0 \rightarrow \pi^+ \pi^- \pi^0$	5983	19261	5204	4146	-1.5%
in sub-sample $B^0 \rightarrow D^- e^+ \nu_e$:	3939	5765	3304	899	
$D^+ \rightarrow K^- \pi^+ \pi^+$	1832	3347	1477	537	-35.4%
$D^+ \rightarrow K^- \pi^+ \pi^+ \pi^0$	3464	4756	2942	732	-4.8%
$D^+ \rightarrow K_s^0 \pi^+$	3724	5520	3115	860	-3.1%
$D^+ \rightarrow K_s^0 \pi^+ \pi^0$	3610	5355	3034	834	-4.3%
$D^+ \rightarrow K^+ K^- \pi^+$	3740	5494	3145	853	-2.4%
$D^+ \rightarrow K_s^0 K^+$	3894	5716	3267	893	-0.6%
$D^+ \rightarrow K_s^0 \pi^+ \pi^+ \pi^-$	3690	5454	3096	855	-3.4%
$D^+ \rightarrow p i^+ \pi^0$	3890	5617	3265	877	-0.5%
$D^+ \rightarrow p i^+ \pi^+ \pi^-$	3756	5072	3160	786	-1.3%
$D^+ \rightarrow K^- \pi^+ \pi^+ \pi^+ \pi^-$	3850	5549	3236	861	-0.8%
in sub-sample $B^0 \rightarrow D^- \mu^+ \nu_\mu$:	3273	5264	2869	965	
$D^+ \rightarrow K^- \pi^+ \pi^+$	1518	3075	1277	573	-35.9%
$D^+ \rightarrow K^- \pi^+ \pi^+ \pi^0$	2885	4358	2552	810	-5.0%
$D^+ \rightarrow K_s^0 \pi^+$	3084	5046	2696	927	-3.3%
$D^+ \rightarrow K_s^0 \pi^+ \pi^0$	3013	4902	2649	895	-4.0%
$D^+ \rightarrow K^+ K^- \pi^+$	3107	5009	2730	915	-2.4%
$D^+ \rightarrow K_s^0 K^+$	3236	5220	2838	957	-0.6%
$D^+ \rightarrow K_s^0 \pi^+ \pi^+ \pi^-$	3073	4972	2693	904	-3.1%
$D^+ \rightarrow p i^+ \pi^0$	3224	5144	2833	948	-0.6%
$D^+ \rightarrow p i^+ \pi^+ \pi^-$	3116	4584	2748	831	-0.9%
$D^+ \rightarrow K^- \pi^+ \pi^+ \pi^+ \pi^-$	3197	5063	2807	927	-0.9%

Table A.1.: Relative changes of the F.O.M. on exclusion of single D decay channels.

B. D -Mass Fits

Table B.1 and Figures B.1 and B.2 show the results of the Gaussian fits to the D meson candidate invariant mass distributions in the generic MC.

sub-sample	D decay channel	μ	σ
$B^0 \rightarrow D^- e^+ \nu_e$	$D^+ \rightarrow K^- \pi^+ \pi^+$	1.869	0.005
$B^0 \rightarrow D^- e^+ \nu_e$	$D^+ \rightarrow K^- \pi^+ \pi^+ \pi^0$	1.868	0.010
$B^0 \rightarrow D^- e^+ \nu_e$	$D^+ \rightarrow K^- \pi^+ \pi^+ \pi^+ \pi^-$	1.869	0.005
$B^0 \rightarrow D^- e^+ \nu_e$	$D^+ \rightarrow K^+ K^- \pi^+$	1.869	0.004
$B^0 \rightarrow D^- e^+ \nu_e$	$D^+ \rightarrow K_s^0 K^+$	1.870	0.005
$B^0 \rightarrow D^- e^+ \nu_e$	$D^+ \rightarrow K_s^0 \pi^+$	1.870	0.005
$B^0 \rightarrow D^- e^+ \nu_e$	$D^+ \rightarrow K_s^0 \pi^+ \pi^0$	1.868	0.013
$B^0 \rightarrow D^- e^+ \nu_e$	$D^+ \rightarrow K_s^0 \pi^+ \pi^+ \pi^-$	1.869	0.005
$B^0 \rightarrow D^- e^+ \nu_e$	$D^+ \rightarrow p i^+ \pi^0$	1.867	0.019
$B^0 \rightarrow D^- e^+ \nu_e$	$D^+ \rightarrow p i^+ \pi^+ \pi^-$	1.869	0.005
$B^0 \rightarrow D^- \mu^+ \nu_\mu$	$D^+ \rightarrow K^- \pi^+ \pi^+$	1.869	0.005
$B^0 \rightarrow D^- \mu^+ \nu_\mu$	$D^+ \rightarrow K^- \pi^+ \pi^+ \pi^0$	1.868	0.009
$B^0 \rightarrow D^- \mu^+ \nu_\mu$	$D^+ \rightarrow K^- \pi^+ \pi^+ \pi^+ \pi^-$	1.868	0.005
$B^0 \rightarrow D^- \mu^+ \nu_\mu$	$D^+ \rightarrow K^+ K^- \pi^+$	1.870	0.004
$B^0 \rightarrow D^- \mu^+ \nu_\mu$	$D^+ \rightarrow K_s^0 K^+$	1.870	0.004
$B^0 \rightarrow D^- \mu^+ \nu_\mu$	$D^+ \rightarrow K_s^0 \pi^+$	1.870	0.005
$B^0 \rightarrow D^- \mu^+ \nu_\mu$	$D^+ \rightarrow K_s^0 \pi^+ \pi^0$	1.868	0.012
$B^0 \rightarrow D^- \mu^+ \nu_\mu$	$D^+ \rightarrow K_s^0 \pi^+ \pi^+ \pi^-$	1.869	0.005
$B^0 \rightarrow D^- \mu^+ \nu_\mu$	$D^+ \rightarrow p i^+ \pi^0$	1.867	0.016
$B^0 \rightarrow D^- \mu^+ \nu_\mu$	$D^+ \rightarrow p i^+ \pi^+ \pi^-$	1.870	0.006
$B^+ \rightarrow \bar{D}^0 e^+ \nu_e$	$D^0 \rightarrow K^- \pi^+$	1.865	0.005
$B^+ \rightarrow \bar{D}^0 e^+ \nu_e$	$D^0 \rightarrow K^- \pi^+ \pi^0$	1.863	0.012
$B^+ \rightarrow \bar{D}^0 e^+ \nu_e$	$D^0 \rightarrow K^- \pi^+ \pi^+ \pi^-$	1.864	0.005
$B^+ \rightarrow \bar{D}^0 e^+ \nu_e$	$D^0 \rightarrow K^- \pi^+ \pi^+ \pi^- \pi^0$	1.864	0.008
$B^+ \rightarrow \bar{D}^0 e^+ \nu_e$	$D^0 \rightarrow K^+ K^-$	1.864	0.004
$B^+ \rightarrow \bar{D}^0 e^+ \nu_e$	$D^0 \rightarrow K_s^0 K_s^0$	1.865	0.004
$B^+ \rightarrow \bar{D}^0 e^+ \nu_e$	$D^0 \rightarrow K_s^0 \pi^0$	1.862	0.017
$B^+ \rightarrow \bar{D}^0 e^+ \nu_e$	$D^0 \rightarrow K_s^0 \pi^0 \pi^0$	1.862	0.016
$B^+ \rightarrow \bar{D}^0 e^+ \nu_e$	$D^0 \rightarrow K_s^0 \pi^+ \pi^-$	1.864	0.005
$B^+ \rightarrow \bar{D}^0 e^+ \nu_e$	$D^0 \rightarrow K_s^0 \pi^+ \pi^- \pi^0$	1.863	0.010
$B^+ \rightarrow \bar{D}^0 e^+ \nu_e$	$D^0 \rightarrow \pi^0 \pi^0$	1.856	0.044
$B^+ \rightarrow \bar{D}^0 e^+ \nu_e$	$D^0 \rightarrow \pi^+ \pi^-$	1.865	0.005
$B^+ \rightarrow \bar{D}^0 e^+ \nu_e$	$D^0 \rightarrow \pi^+ \pi^- \pi^0$	1.862	0.014
$B^+ \rightarrow \bar{D}^0 \mu^+ \nu_\mu$	$D^0 \rightarrow K^- \pi^+$	1.865	0.005
$B^+ \rightarrow \bar{D}^0 \mu^+ \nu_\mu$	$D^0 \rightarrow K^- \pi^+ \pi^0$	1.863	0.012
$B^+ \rightarrow \bar{D}^0 \mu^+ \nu_\mu$	$D^0 \rightarrow K^- \pi^+ \pi^+ \pi^-$	1.864	0.005
$B^+ \rightarrow \bar{D}^0 \mu^+ \nu_\mu$	$D^0 \rightarrow K^- \pi^+ \pi^+ \pi^- \pi^0$	1.863	0.008
$B^+ \rightarrow \bar{D}^0 \mu^+ \nu_\mu$	$D^0 \rightarrow K^+ K^-$	1.864	0.005
$B^+ \rightarrow \bar{D}^0 \mu^+ \nu_\mu$	$D^0 \rightarrow K_s^0 K_s^0$	1.863	0.007
$B^+ \rightarrow \bar{D}^0 \mu^+ \nu_\mu$	$D^0 \rightarrow K_s^0 \pi^0$	1.862	0.019
$B^+ \rightarrow \bar{D}^0 \mu^+ \nu_\mu$	$D^0 \rightarrow K_s^0 \pi^0 \pi^0$	1.862	0.020
$B^+ \rightarrow \bar{D}^0 \mu^+ \nu_\mu$	$D^0 \rightarrow K_s^0 \pi^+ \pi^-$	1.865	0.005
$B^+ \rightarrow \bar{D}^0 \mu^+ \nu_\mu$	$D^0 \rightarrow K_s^0 \pi^+ \pi^- \pi^0$	1.863	0.011
$B^+ \rightarrow \bar{D}^0 \mu^+ \nu_\mu$	$D^0 \rightarrow \pi^0 \pi^0$	1.867	0.103
$B^+ \rightarrow \bar{D}^0 \mu^+ \nu_\mu$	$D^0 \rightarrow \pi^+ \pi^-$	1.865	0.005
$B^+ \rightarrow \bar{D}^0 \mu^+ \nu_\mu$	$D^0 \rightarrow \pi^+ \pi^- \pi^0$	1.863	0.014

Table B.1.: Results (Gaussian mean and sigma) of the D invariant mass fits.

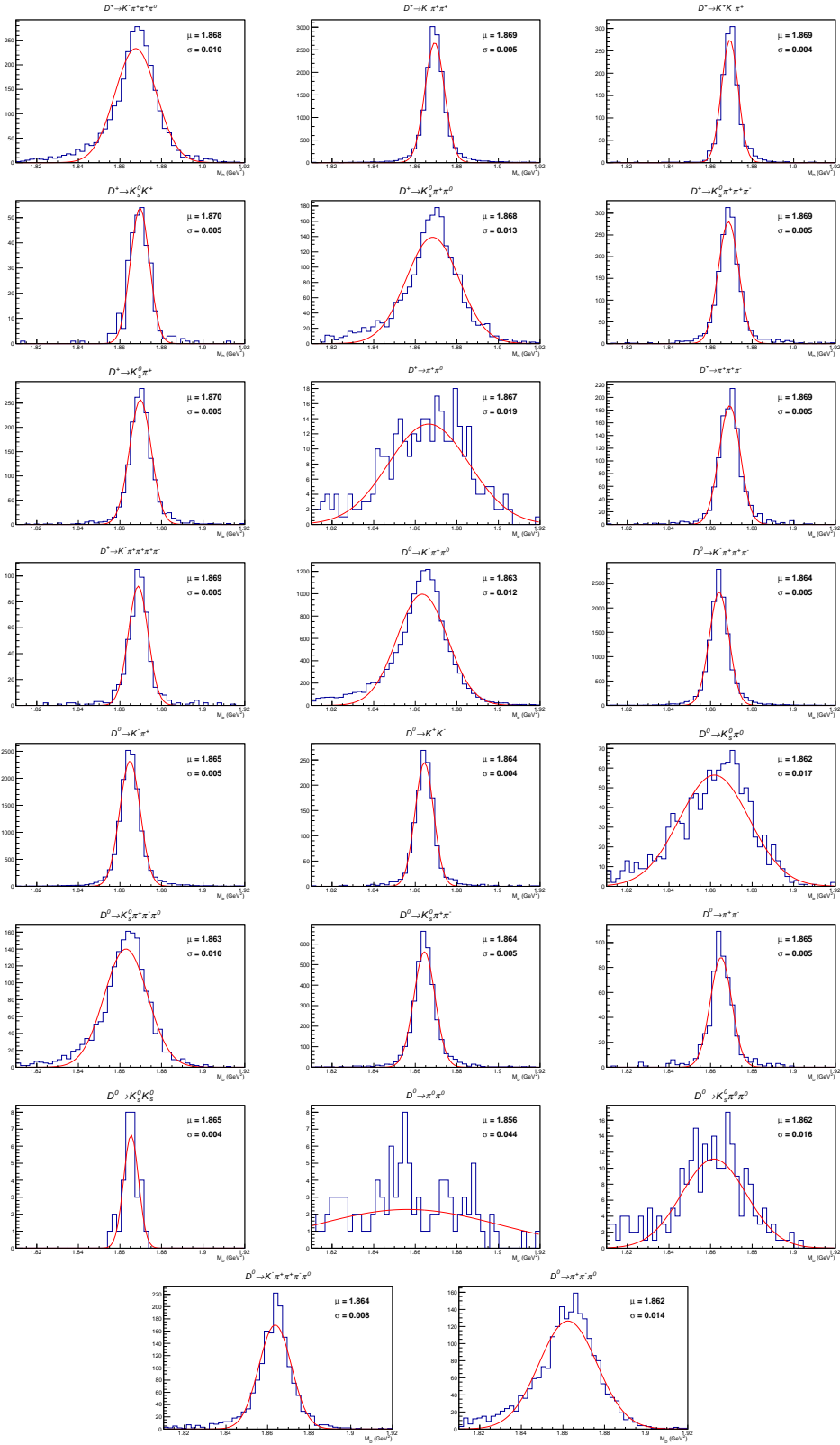


Figure B.1.: The fits of the reconstructed D mass in the electron channels. Source are all genuinely reconstructed D mesons in the five generic MC streams.

B. D -Mass Fits

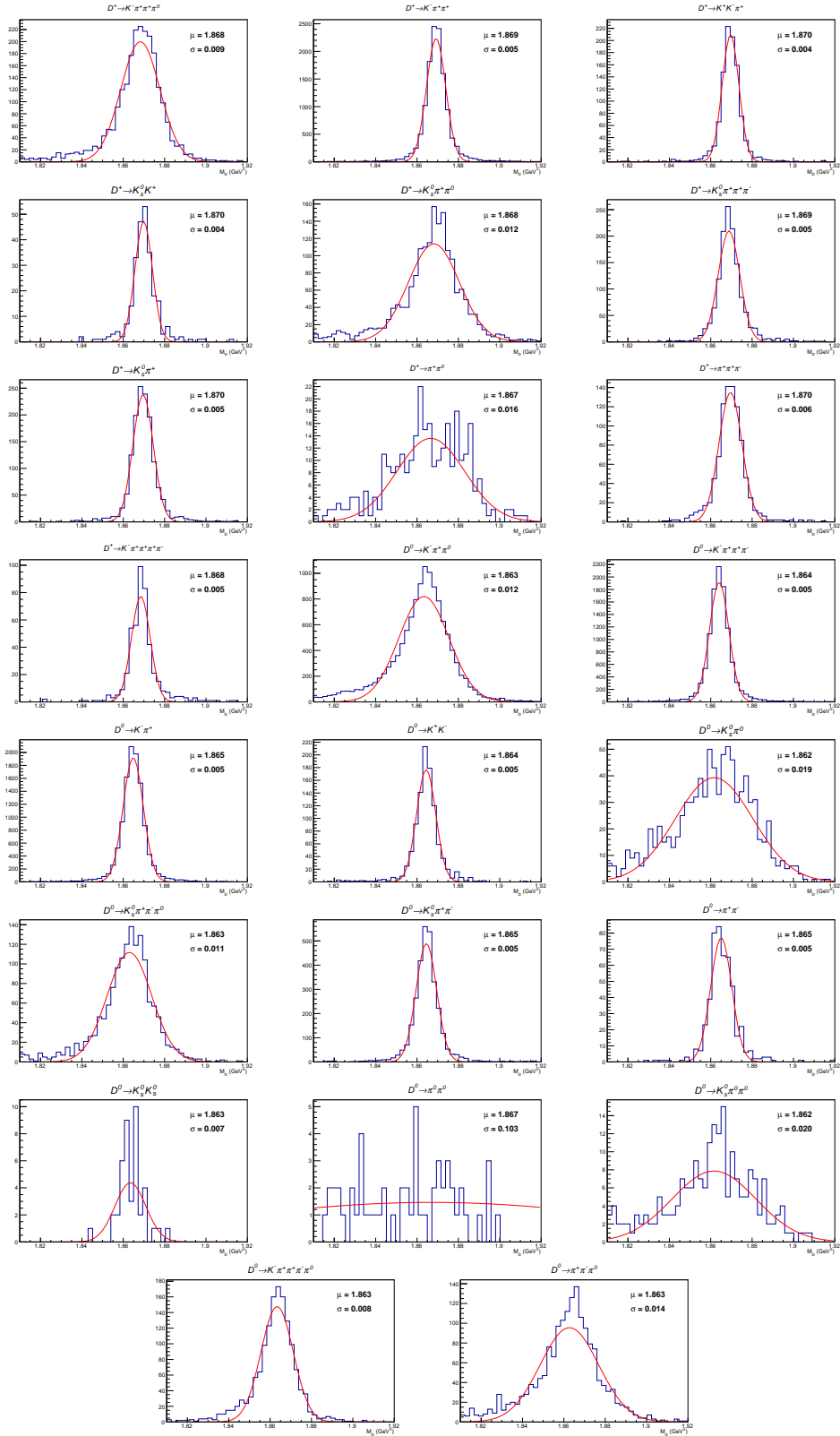


Figure B.2.: The fits of the reconstructed D mass in the muon channels. Source are all genuinely reconstructed D mesons in the five generic MC streams.

C. Full Systematic Correlation Matrix

The full systematic correlations corresponding to Table 9.1 in chapter 9 between the four sub-samples and their w -bins are shown in Tables C.1 - C.4.

		Systematic correlation with sub-sample $B^0 \rightarrow D^- e^+ \nu_e$									
sub-sample	i	0	1	2	3	4	5	6	7	8	9
$B^0 \rightarrow D^- e^+ \nu_e$	0	1.00000	0.19201	0.20767	0.20427	0.20016	0.21969	0.22870	0.21233	0.18255	0.14484
$B^0 \rightarrow D^- e^+ \nu_e$	1	0.19201	1.00000	0.91858	0.91639	0.92366	0.92819	0.92807	0.94187	0.94109	0.92839
$B^0 \rightarrow D^- e^+ \nu_e$	2	0.20767	0.91858	1.00000	0.96354	0.96287	0.97458	0.97171	0.97166	0.95646	0.93777
$B^0 \rightarrow D^- e^+ \nu_e$	3	0.20427	0.91639	0.96354	1.00000	0.97258	0.98080	0.97651	0.97688	0.96272	0.94914
$B^0 \rightarrow D^- e^+ \nu_e$	4	0.20016	0.92366	0.96287	0.97258	1.00000	0.98146	0.97642	0.97835	0.96712	0.95576
$B^0 \rightarrow D^- e^+ \nu_e$	5	0.21969	0.92819	0.97458	0.98080	0.98146	1.00000	0.98979	0.99007	0.97934	0.96270
$B^0 \rightarrow D^- e^+ \nu_e$	6	0.22870	0.92807	0.97171	0.97651	0.97642	0.98979	1.00000	0.99160	0.97524	0.95343
$B^0 \rightarrow D^- e^+ \nu_e$	7	0.21233	0.94187	0.97166	0.97688	0.97835	0.99007	0.99160	1.00000	0.98917	0.97062
$B^0 \rightarrow D^- e^+ \nu_e$	8	0.18255	0.94109	0.95646	0.96272	0.96712	0.97934	0.97524	0.98917	1.00000	0.98895
$B^0 \rightarrow D^- e^+ \nu_e$	9	0.14484	0.92839	0.93777	0.94914	0.95576	0.96270	0.95343	0.97062	0.98895	1.00000
$B^0 \rightarrow D^- \mu^+ \nu_\mu$	0	0.13220	0.44202	0.49062	0.47805	0.47546	0.48364	0.50048	0.48695	0.45457	0.42617
$B^0 \rightarrow D^- \mu^+ \nu_\mu$	1	0.22258	0.88784	0.92492	0.92919	0.93168	0.94180	0.94144	0.94305	0.92924	0.90759
$B^0 \rightarrow D^- \mu^+ \nu_\mu$	2	0.21582	0.91691	0.95427	0.95837	0.96368	0.97199	0.96721	0.97295	0.96607	0.94508
$B^0 \rightarrow D^- \mu^+ \nu_\mu$	3	0.19854	0.92761	0.96719	0.97176	0.97593	0.98164	0.97896	0.98078	0.96619	0.95265
$B^0 \rightarrow D^- \mu^+ \nu_\mu$	4	0.18602	0.93248	0.95766	0.96467	0.97417	0.97388	0.96715	0.97522	0.97200	0.96563
$B^0 \rightarrow D^- \mu^+ \nu_\mu$	5	0.20081	0.93691	0.97038	0.97846	0.97886	0.99059	0.98828	0.99126	0.98390	0.97135
$B^0 \rightarrow D^- \mu^+ \nu_\mu$	6	0.20867	0.93727	0.97267	0.97957	0.98019	0.99174	0.98990	0.99476	0.98640	0.96976
$B^0 \rightarrow D^- \mu^+ \nu_\mu$	7	0.21549	0.93982	0.96974	0.97404	0.97572	0.98885	0.99024	0.99605	0.98966	0.97204
$B^0 \rightarrow D^- \mu^+ \nu_\mu$	8	0.18084	0.94352	0.96105	0.96621	0.97023	0.97964	0.97652	0.98799	0.99387	0.98323
$B^0 \rightarrow D^- \mu^+ \nu_\mu$	9	0.13747	0.92830	0.93568	0.94755	0.95512	0.96010	0.95105	0.96797	0.98640	0.99808
$B^+ \rightarrow \bar{D}^0 e^+ \nu_e$	0	0.07870	0.23632	0.27008	0.25376	0.24194	0.25459	0.26881	0.25752	0.25766	0.24320
$B^+ \rightarrow \bar{D}^0 e^+ \nu_e$	1	0.26398	0.54786	0.60631	0.59030	0.56855	0.60551	0.61602	0.59278	0.57310	0.53134
$B^+ \rightarrow \bar{D}^0 e^+ \nu_e$	2	0.23277	0.64117	0.69192	0.67205	0.66357	0.68879	0.69005	0.67825	0.67618	0.64624
$B^+ \rightarrow \bar{D}^0 e^+ \nu_e$	3	0.22166	0.63910	0.69341	0.67431	0.66155	0.68976	0.68932	0.67424	0.67334	0.64637
$B^+ \rightarrow \bar{D}^0 e^+ \nu_e$	4	0.21036	0.64820	0.69717	0.67892	0.67038	0.69621	0.69421	0.68121	0.68396	0.66158
$B^+ \rightarrow \bar{D}^0 e^+ \nu_e$	5	0.20621	0.66856	0.71607	0.69842	0.69410	0.71387	0.71122	0.70314	0.70804	0.68693
$B^+ \rightarrow \bar{D}^0 e^+ \nu_e$	6	0.20651	0.68184	0.72630	0.71142	0.70720	0.72482	0.72342	0.71659	0.71946	0.69723
$B^+ \rightarrow \bar{D}^0 e^+ \nu_e$	7	0.18478	0.67625	0.71444	0.69931	0.70000	0.71389	0.71099	0.70981	0.71941	0.70172
$B^+ \rightarrow \bar{D}^0 e^+ \nu_e$	8	0.15375	0.67913	0.70680	0.69591	0.70103	0.70821	0.70046	0.70692	0.72713	0.71930
$B^+ \rightarrow \bar{D}^0 e^+ \nu_e$	9	0.13304	0.66964	0.68300	0.67297	0.68158	0.68553	0.67310	0.68420	0.71521	0.72015
$B^+ \rightarrow \bar{D}^0 \mu^+ \nu_\mu$	0	0.18631	0.52617	0.57017	0.55555	0.55815	0.57258	0.57710	0.56749	0.56162	0.53230
$B^+ \rightarrow \bar{D}^0 \mu^+ \nu_\mu$	1	0.23146	0.63002	0.68294	0.65894	0.65012	0.67533	0.68016	0.66642	0.65597	0.62269
$B^+ \rightarrow \bar{D}^0 \mu^+ \nu_\mu$	2	0.21522	0.64180	0.69404	0.67438	0.66045	0.68783	0.69147	0.67927	0.67757	0.65041
$B^+ \rightarrow \bar{D}^0 \mu^+ \nu_\mu$	3	0.19981	0.65909	0.70792	0.69360	0.68381	0.70642	0.70400	0.69531	0.69973	0.67886
$B^+ \rightarrow \bar{D}^0 \mu^+ \nu_\mu$	4	0.19548	0.67160	0.71099	0.69695	0.69295	0.71132	0.70629	0.69986	0.70955	0.69249
$B^+ \rightarrow \bar{D}^0 \mu^+ \nu_\mu$	5	0.19041	0.66961	0.71080	0.69690	0.69121	0.70983	0.70476	0.69944	0.70848	0.69162
$B^+ \rightarrow \bar{D}^0 \mu^+ \nu_\mu$	6	0.20040	0.67387	0.71662	0.70149	0.69919	0.71584	0.71446	0.70846	0.71427	0.69354
$B^+ \rightarrow \bar{D}^0 \mu^+ \nu_\mu$	7	0.18085	0.67701	0.71411	0.70027	0.70152	0.71311	0.71002	0.70973	0.72050	0.70444
$B^+ \rightarrow \bar{D}^0 \mu^+ \nu_\mu$	8	0.15361	0.68050	0.70884	0.69797	0.70334	0.71053	0.70319	0.70871	0.72870	0.71968
$B^+ \rightarrow \bar{D}^0 \mu^+ \nu_\mu$	9	0.13154	0.67746	0.69212	0.68329	0.69174	0.69519	0.68220	0.69371	0.72474	0.73095

Table C.1.: Systematic correlations with the $B^0 \rightarrow D^- e^+ \nu_e$ sub-sample.

C. Full Systematic Correlation Matrix

sub-sample	i	Systematic correlation with sub-sample $B^0 \rightarrow D^- \mu^+ \nu_\mu$									
		0	1	2	3	4	5	6	7	8	9
$B^0 \rightarrow D^- e^+ \nu_e$	0	0.13220	0.22258	0.21582	0.19854	0.18602	0.20081	0.20867	0.21549	0.18084	0.13747
$B^0 \rightarrow D^- e^+ \nu_e$	1	0.44202	0.88784	0.91691	0.92761	0.93248	0.93691	0.93727	0.93982	0.94352	0.92830
$B^0 \rightarrow D^- e^+ \nu_e$	2	0.49062	0.92492	0.95427	0.96719	0.95766	0.97038	0.97267	0.96974	0.96105	0.93568
$B^0 \rightarrow D^- e^+ \nu_e$	3	0.47805	0.92919	0.95837	0.97176	0.96467	0.97846	0.97957	0.97404	0.96621	0.94755
$B^0 \rightarrow D^- e^+ \nu_e$	4	0.47546	0.93168	0.96368	0.97593	0.97417	0.97886	0.98019	0.97572	0.97023	0.95512
$B^0 \rightarrow D^- e^+ \nu_e$	5	0.48364	0.94180	0.97199	0.98164	0.97388	0.99059	0.99174	0.98885	0.97964	0.96010
$B^0 \rightarrow D^- e^+ \nu_e$	6	0.50048	0.94144	0.96721	0.97896	0.96715	0.98828	0.98990	0.99024	0.97652	0.95105
$B^0 \rightarrow D^- e^+ \nu_e$	7	0.48695	0.94305	0.97295	0.98078	0.97522	0.99126	0.99476	0.99605	0.98799	0.96797
$B^0 \rightarrow D^- e^+ \nu_e$	8	0.45457	0.92924	0.96607	0.96619	0.97200	0.98390	0.98640	0.98966	0.99387	0.98640
$B^0 \rightarrow D^- e^+ \nu_e$	9	0.42617	0.90759	0.94508	0.95265	0.96563	0.97135	0.96976	0.97204	0.98323	0.99808
$B^0 \rightarrow D^- \mu^+ \nu_\mu$	0	1.00000	0.48274	0.48146	0.49533	0.48102	0.48389	0.48558	0.48604	0.45973	0.42283
$B^0 \rightarrow D^- \mu^+ \nu_\mu$	1	0.48274	1.00000	0.92447	0.93058	0.92410	0.94081	0.94065	0.94157	0.93285	0.90442
$B^0 \rightarrow D^- \mu^+ \nu_\mu$	2	0.48146	0.92447	1.00000	0.96129	0.95773	0.96589	0.97367	0.97107	0.96478	0.94081
$B^0 \rightarrow D^- \mu^+ \nu_\mu$	3	0.49533	0.93058	0.96129	1.00000	0.97189	0.97866	0.98275	0.97842	0.96750	0.95137
$B^0 \rightarrow D^- \mu^+ \nu_\mu$	4	0.48102	0.92410	0.95773	0.97189	1.00000	0.97671	0.97659	0.97181	0.97359	0.96453
$B^0 \rightarrow D^- \mu^+ \nu_\mu$	5	0.48389	0.94081	0.96589	0.97866	0.97671	1.00000	0.99112	0.98956	0.98439	0.96909
$B^0 \rightarrow D^- \mu^+ \nu_\mu$	6	0.48558	0.94065	0.97367	0.98275	0.97659	0.99112	1.00000	0.99330	0.98566	0.96693
$B^0 \rightarrow D^- \mu^+ \nu_\mu$	7	0.48604	0.94157	0.97107	0.97842	0.97181	0.98956	0.99330	1.00000	0.98861	0.96965
$B^0 \rightarrow D^- \mu^+ \nu_\mu$	8	0.45973	0.93285	0.96478	0.96750	0.97359	0.98439	0.98566	0.98861	1.00000	0.98131
$B^0 \rightarrow D^- \mu^+ \nu_\mu$	9	0.42283	0.90442	0.94081	0.95137	0.96453	0.96909	0.96693	0.96965	0.98131	1.00000
$B^+ \rightarrow \bar{D}^0 e^+ \nu_e$	0	0.20420	0.23871	0.23453	0.25247	0.26322	0.25208	0.25178	0.26541	0.26307	0.24394
$B^+ \rightarrow \bar{D}^0 e^+ \nu_e$	1	0.41117	0.61266	0.59799	0.58524	0.55759	0.59274	0.58985	0.59994	0.57908	0.52253
$B^+ \rightarrow \bar{D}^0 e^+ \nu_e$	2	0.41187	0.68186	0.67979	0.66771	0.66063	0.67977	0.67268	0.68587	0.68238	0.64100
$B^+ \rightarrow \bar{D}^0 e^+ \nu_e$	3	0.40888	0.67566	0.67895	0.66836	0.65988	0.68008	0.67248	0.68320	0.68102	0.64064
$B^+ \rightarrow \bar{D}^0 e^+ \nu_e$	4	0.40317	0.68343	0.68443	0.67454	0.67144	0.68994	0.67983	0.68974	0.69173	0.65635
$B^+ \rightarrow \bar{D}^0 e^+ \nu_e$	5	0.40618	0.69945	0.70455	0.69260	0.69579	0.70840	0.69942	0.71021	0.71572	0.68330
$B^+ \rightarrow \bar{D}^0 e^+ \nu_e$	6	0.41277	0.70974	0.71459	0.70336	0.70705	0.72013	0.71125	0.72370	0.72759	0.69458
$B^+ \rightarrow \bar{D}^0 e^+ \nu_e$	7	0.39624	0.69640	0.70556	0.69155	0.70083	0.71157	0.70199	0.71646	0.72542	0.70026
$B^+ \rightarrow \bar{D}^0 e^+ \nu_e$	8	0.37251	0.68845	0.70167	0.68632	0.70702	0.71039	0.69909	0.71243	0.73148	0.71912
$B^+ \rightarrow \bar{D}^0 e^+ \nu_e$	9	0.34213	0.66743	0.68414	0.66492	0.69390	0.69076	0.67755	0.68981	0.71685	0.72140
$B^+ \rightarrow \bar{D}^0 \mu^+ \nu_\mu$	0	0.39191	0.57808	0.56387	0.55470	0.54544	0.56277	0.55720	0.57097	0.56342	0.52732
$B^+ \rightarrow \bar{D}^0 \mu^+ \nu_\mu$	1	0.41840	0.66864	0.66603	0.65376	0.64162	0.66541	0.65877	0.67569	0.66697	0.62085
$B^+ \rightarrow \bar{D}^0 \mu^+ \nu_\mu$	2	0.41886	0.67583	0.67728	0.67008	0.66465	0.68186	0.67367	0.68771	0.68478	0.64567
$B^+ \rightarrow \bar{D}^0 \mu^+ \nu_\mu$	3	0.40160	0.69551	0.69636	0.68697	0.68788	0.70210	0.69117	0.70289	0.70821	0.67459
$B^+ \rightarrow \bar{D}^0 \mu^+ \nu_\mu$	4	0.40042	0.69815	0.70215	0.68962	0.69698	0.70851	0.69697	0.70771	0.71795	0.68904
$B^+ \rightarrow \bar{D}^0 \mu^+ \nu_\mu$	5	0.39628	0.69487	0.69961	0.68855	0.69572	0.70616	0.69615	0.70715	0.71561	0.68850
$B^+ \rightarrow \bar{D}^0 \mu^+ \nu_\mu$	6	0.40945	0.70171	0.70665	0.69469	0.70045	0.71234	0.70287	0.71554	0.72187	0.69090
$B^+ \rightarrow \bar{D}^0 \mu^+ \nu_\mu$	7	0.39504	0.69745	0.70461	0.69183	0.70267	0.71201	0.70198	0.71620	0.72695	0.70376
$B^+ \rightarrow \bar{D}^0 \mu^+ \nu_\mu$	8	0.37215	0.69069	0.70362	0.68812	0.70878	0.71293	0.70174	0.71457	0.73353	0.71932
$B^+ \rightarrow \bar{D}^0 \mu^+ \nu_\mu$	9	0.34345	0.67539	0.69268	0.67499	0.70365	0.70114	0.68768	0.69913	0.72644	0.73181

Table C.2.: Systematic correlations with the $B^0 \rightarrow D^- \mu^+ \nu_\mu$ sub-sample.

sub-sample	i	Systematic correlation with sub-sample $B^+ \rightarrow \bar{D}^0 e^+ \nu_e$									
		0	1	2	3	4	5	6	7	8	9
$B^0 \rightarrow D^- e^+ \nu_e$	0	0.07870	0.26398	0.23277	0.22166	0.21036	0.20621	0.20651	0.18478	0.15375	0.13304
$B^0 \rightarrow D^- e^+ \nu_e$	1	0.23632	0.54786	0.64117	0.63910	0.64820	0.66856	0.68184	0.67625	0.67913	0.66964
$B^0 \rightarrow D^- e^+ \nu_e$	2	0.27008	0.60631	0.69192	0.69341	0.69717	0.71607	0.72630	0.71444	0.70680	0.68300
$B^0 \rightarrow D^- e^+ \nu_e$	3	0.25376	0.59030	0.67205	0.67431	0.67892	0.69842	0.71142	0.69931	0.69591	0.67297
$B^0 \rightarrow D^- e^+ \nu_e$	4	0.24194	0.56855	0.66357	0.66155	0.67038	0.69410	0.70720	0.70000	0.70103	0.68158
$B^0 \rightarrow D^- e^+ \nu_e$	5	0.25459	0.60551	0.68879	0.68976	0.69621	0.71387	0.72482	0.71389	0.70821	0.68553
$B^0 \rightarrow D^- e^+ \nu_e$	6	0.26881	0.61602	0.69005	0.68932	0.69421	0.71122	0.72342	0.71099	0.70046	0.67310
$B^0 \rightarrow D^- e^+ \nu_e$	7	0.25752	0.59278	0.67825	0.67424	0.68121	0.70314	0.71659	0.70981	0.70692	0.68420
$B^0 \rightarrow D^- e^+ \nu_e$	8	0.25766	0.57310	0.67618	0.67334	0.68396	0.70804	0.71946	0.71941	0.72713	0.71521
$B^0 \rightarrow D^- e^+ \nu_e$	9	0.24320	0.53134	0.64624	0.64637	0.66158	0.68693	0.69723	0.70172	0.71930	0.72015
$B^0 \rightarrow D^- \mu^+ \nu_\mu$	0	0.20420	0.41117	0.41187	0.40888	0.40317	0.40618	0.41277	0.39624	0.37251	0.34213
$B^0 \rightarrow D^- \mu^+ \nu_\mu$	1	0.23871	0.61266	0.68186	0.67566	0.68343	0.69945	0.70974	0.69640	0.68845	0.66743
$B^0 \rightarrow D^- \mu^+ \nu_\mu$	2	0.23453	0.59799	0.67979	0.67895	0.68443	0.70455	0.71459	0.70556	0.70167	0.68414
$B^0 \rightarrow D^- \mu^+ \nu_\mu$	3	0.25247	0.58524	0.66771	0.66836	0.67454	0.69260	0.70336	0.69155	0.68632	0.66492
$B^0 \rightarrow D^- \mu^+ \nu_\mu$	4	0.26322	0.55759	0.66063	0.65988	0.67144	0.69579	0.70705	0.70083	0.70702	0.69390
$B^0 \rightarrow D^- \mu^+ \nu_\mu$	5	0.25208	0.59274	0.67977	0.68008	0.68994	0.70840	0.72013	0.71157	0.71039	0.69076
$B^0 \rightarrow D^- \mu^+ \nu_\mu$	6	0.25178	0.58985	0.67268	0.67248	0.67983	0.69942	0.71125	0.70199	0.69909	0.67755
$B^0 \rightarrow D^- \mu^+ \nu_\mu$	7	0.26541	0.59994	0.68587	0.68320	0.68974	0.71021	0.72370	0.71646	0.71243	0.68981
$B^0 \rightarrow D^- \mu^+ \nu_\mu$	8	0.26307	0.57908	0.68238	0.68102	0.69173	0.71572	0.72759	0.72542	0.73148	0.71685
$B^0 \rightarrow D^- \mu^+ \nu_\mu$	9	0.24394	0.52253	0.64100	0.64064	0.65635	0.68330	0.69458	0.70026	0.71912	0.72140
$B^+ \rightarrow \bar{D}^0 e^+ \nu_e$	0	1.00000	0.32536	0.36568	0.35536	0.35332	0.36344	0.36446	0.36466	0.35188	0.32808
$B^+ \rightarrow \bar{D}^0 e^+ \nu_e$	1	0.32536	1.00000	0.90899	0.90913	0.90436	0.88440	0.87468	0.84456	0.79363	0.76292
$B^+ \rightarrow \bar{D}^0 e^+ \nu_e$	2	0.36568	0.90899	1.00000	0.98267	0.98179	0.98209	0.97647	0.96403	0.93583	0.91261
$B^+ \rightarrow \bar{D}^0 e^+ \nu_e$	3	0.35536	0.90913	0.98267	1.00000	0.98759	0.98164	0.97345	0.95712	0.92644	0.90311
$B^+ \rightarrow \bar{D}^0 e^+ \nu_e$	4	0.35332	0.90436	0.98179	0.98759	1.00000	0.98812	0.97938	0.96509	0.93873	0.92003
$B^+ \rightarrow \bar{D}^0 e^+ \nu_e$	5	0.36344	0.88440	0.98209	0.98164	0.98812	1.00000	0.99217	0.98651	0.96861	0.94768
$B^+ \rightarrow \bar{D}^0 e^+ \nu_e$	6	0.36446	0.87468	0.97647	0.97345	0.97938	0.99217	1.00000	0.99126	0.97466	0.94942
$B^+ \rightarrow \bar{D}^0 e^+ \nu_e$	7	0.36466	0.84456	0.96403	0.95712	0.96509	0.98651	0.99126	1.00000	0.99145	0.96896
$B^+ \rightarrow \bar{D}^0 e^+ \nu_e$	8	0.35188	0.79363	0.93583	0.92644	0.93873	0.96861	0.97466	0.99145	1.00000	0.98416
$B^+ \rightarrow \bar{D}^0 e^+ \nu_e$	9	0.32808	0.76292	0.91261	0.90311	0.92003	0.94768	0.94942	0.96896	0.98416	1.00000
$B^+ \rightarrow \bar{D}^0 \mu^+ \nu_\mu$	0	0.29997	0.73760	0.80686	0.79571	0.79895	0.80491	0.79535	0.79294	0.77171	0.74298
$B^+ \rightarrow \bar{D}^0 \mu^+ \nu_\mu$	1	0.35705	0.89623	0.96577	0.96394	0.96036	0.96337	0.96425	0.95107	0.91821	0.89096
$B^+ \rightarrow \bar{D}^0 \mu^+ \nu_\mu$	2	0.38590	0.89410	0.97443	0.97456	0.97484	0.97677	0.97076	0.96066	0.93345	0.90716
$B^+ \rightarrow \bar{D}^0 \mu^+ \nu_\mu$	3	0.36396	0.88902	0.98122	0.98275	0.98713	0.99006	0.98626	0.97701	0.95810	0.93735
$B^+ \rightarrow \bar{D}^0 \mu^+ \nu_\mu$	4	0.35657	0.87529	0.97640	0.97933	0.98631	0.99208	0.98722	0.98211	0.96742	0.95146
$B^+ \rightarrow \bar{D}^0 \mu^+ \nu_\mu$	5	0.36692	0.87531	0.97806	0.97834	0.98533	0.99430	0.99200	0.98769	0.97377	0.95639
$B^+ \rightarrow \bar{D}^0 \mu^+ \nu_\mu$	6	0.36309	0.86903	0.97578	0.97195	0.97965	0.99360	0.99481	0.99384	0.98067	0.95579
$B^+ \rightarrow \bar{D}^0 \mu^+ \nu_\mu$	7	0.36323	0.83614	0.96004	0.95188	0.96072	0.98418	0.98903	0.99759	0.99339	0.97170
$B^+ \rightarrow \bar{D}^0 \mu^+ \nu_\mu$	8	0.35410	0.79365	0.93529	0.92680	0.93969	0.96897	0.97531	0.99082	0.99772	0.97927
$B^+ \rightarrow \bar{D}^0 \mu^+ \nu_\mu$	9	0.32849	0.75944	0.91033	0.90177	0.91923	0.94770	0.95015	0.96941	0.98586	0.99892

Table C.3.: Systematic correlations with the $B^+ \rightarrow \bar{D}^0 e^+ \nu_e$ sub-sample.

C. Full Systematic Correlation Matrix

		Systematic correlation with sub-sample $B^+ \rightarrow \bar{D}^0 \mu^+ \nu_\mu$									
sub-sample	i	0	1	2	3	4	5	6	7	8	9
$B^0 \rightarrow D^- e^+ \nu_e$	0	0.18631	0.23146	0.21522	0.19981	0.19548	0.19041	0.20040	0.18085	0.15361	0.13154
$B^0 \rightarrow D^- e^+ \nu_e$	1	0.52617	0.63002	0.64180	0.65909	0.67160	0.66961	0.67387	0.67701	0.68050	0.67746
$B^0 \rightarrow D^- e^+ \nu_e$	2	0.57017	0.68294	0.69404	0.70792	0.71099	0.71080	0.71662	0.71411	0.70884	0.69212
$B^0 \rightarrow D^- e^+ \nu_e$	3	0.55555	0.65894	0.67438	0.69360	0.69695	0.69690	0.70149	0.70027	0.69797	0.68329
$B^0 \rightarrow D^- e^+ \nu_e$	4	0.55815	0.65012	0.66045	0.68381	0.69295	0.69121	0.69919	0.70152	0.70334	0.69174
$B^0 \rightarrow D^- e^+ \nu_e$	5	0.57258	0.67533	0.68783	0.70642	0.71132	0.70983	0.71584	0.71311	0.71053	0.69519
$B^0 \rightarrow D^- e^+ \nu_e$	6	0.57710	0.68016	0.69147	0.70400	0.70629	0.70476	0.71446	0.71002	0.70319	0.68220
$B^0 \rightarrow D^- e^+ \nu_e$	7	0.56749	0.66642	0.67927	0.69531	0.69986	0.69944	0.70846	0.70973	0.70871	0.69371
$B^0 \rightarrow D^- e^+ \nu_e$	8	0.56162	0.65597	0.67757	0.69973	0.70955	0.70848	0.71427	0.72050	0.72870	0.72474
$B^0 \rightarrow D^- e^+ \nu_e$	9	0.53230	0.62269	0.65041	0.67886	0.69249	0.69162	0.69354	0.70444	0.71968	0.73095
$B^0 \rightarrow D^- \mu^+ \nu_\mu$	0	0.39191	0.41840	0.41886	0.40160	0.40042	0.39628	0.40945	0.39504	0.37215	0.34345
$B^0 \rightarrow D^- \mu^+ \nu_\mu$	1	0.57808	0.66864	0.67583	0.69551	0.69815	0.69487	0.70171	0.69745	0.69069	0.67539
$B^0 \rightarrow D^- \mu^+ \nu_\mu$	2	0.56387	0.66603	0.67728	0.69636	0.70215	0.69961	0.70665	0.70461	0.70362	0.69268
$B^0 \rightarrow D^- \mu^+ \nu_\mu$	3	0.55470	0.65376	0.67008	0.68697	0.68962	0.68855	0.69469	0.69183	0.68812	0.67499
$B^0 \rightarrow D^- \mu^+ \nu_\mu$	4	0.54544	0.64162	0.66465	0.68788	0.69698	0.69572	0.70045	0.70267	0.70878	0.70365
$B^0 \rightarrow D^- \mu^+ \nu_\mu$	5	0.56277	0.66541	0.68186	0.70210	0.70851	0.70616	0.71234	0.71201	0.71293	0.70114
$B^0 \rightarrow D^- \mu^+ \nu_\mu$	6	0.55720	0.65877	0.67367	0.69117	0.69697	0.69615	0.70287	0.70198	0.70174	0.68768
$B^0 \rightarrow D^- \mu^+ \nu_\mu$	7	0.57097	0.67569	0.68771	0.70289	0.70771	0.70715	0.71554	0.71620	0.71457	0.69913
$B^0 \rightarrow D^- \mu^+ \nu_\mu$	8	0.56342	0.66697	0.68478	0.70821	0.71795	0.71561	0.72187	0.72695	0.73353	0.72644
$B^0 \rightarrow D^- \mu^+ \nu_\mu$	9	0.52732	0.62085	0.64567	0.67459	0.68904	0.68850	0.69090	0.70376	0.71932	0.73181
$B^+ \rightarrow \bar{D}^0 e^+ \nu_e$	0	0.29997	0.35705	0.38590	0.36396	0.35657	0.36692	0.36309	0.36323	0.35410	0.32849
$B^+ \rightarrow \bar{D}^0 e^+ \nu_e$	1	0.73760	0.89623	0.89410	0.88902	0.87529	0.87531	0.86903	0.83614	0.79365	0.75944
$B^+ \rightarrow \bar{D}^0 e^+ \nu_e$	2	0.80686	0.96577	0.97443	0.98122	0.97640	0.97806	0.97578	0.96004	0.93529	0.91033
$B^+ \rightarrow \bar{D}^0 e^+ \nu_e$	3	0.79571	0.96394	0.97456	0.98275	0.97933	0.97834	0.97195	0.95188	0.92680	0.90177
$B^+ \rightarrow \bar{D}^0 e^+ \nu_e$	4	0.79895	0.96036	0.97484	0.98713	0.98631	0.98533	0.97965	0.96072	0.93969	0.91923
$B^+ \rightarrow \bar{D}^0 e^+ \nu_e$	5	0.80491	0.96337	0.97677	0.99006	0.99208	0.99430	0.99360	0.98418	0.96897	0.94770
$B^+ \rightarrow \bar{D}^0 e^+ \nu_e$	6	0.79535	0.96425	0.97076	0.98626	0.98722	0.99200	0.99481	0.98903	0.97531	0.95015
$B^+ \rightarrow \bar{D}^0 e^+ \nu_e$	7	0.79294	0.95107	0.96066	0.97701	0.98211	0.98769	0.99384	0.99759	0.99082	0.96941
$B^+ \rightarrow \bar{D}^0 e^+ \nu_e$	8	0.77171	0.91821	0.93345	0.95810	0.96742	0.97377	0.98067	0.99339	0.99772	0.98586
$B^+ \rightarrow \bar{D}^0 e^+ \nu_e$	9	0.74298	0.89096	0.90716	0.93735	0.95146	0.95639	0.95579	0.97170	0.97927	0.99892
$B^+ \rightarrow \bar{D}^0 \mu^+ \nu_\mu$	0	1.00000	0.78642	0.79572	0.80042	0.79708	0.79548	0.80330	0.79144	0.77078	0.74260
$B^+ \rightarrow \bar{D}^0 \mu^+ \nu_\mu$	1	0.78642	1.00000	0.95460	0.95816	0.95420	0.95924	0.95944	0.94812	0.91678	0.88765
$B^+ \rightarrow \bar{D}^0 \mu^+ \nu_\mu$	2	0.79572	0.95460	1.00000	0.97581	0.97269	0.97288	0.97216	0.95650	0.93346	0.90579
$B^+ \rightarrow \bar{D}^0 \mu^+ \nu_\mu$	3	0.80042	0.95816	0.97581	1.00000	0.98933	0.98951	0.98728	0.97535	0.95835	0.93704
$B^+ \rightarrow \bar{D}^0 \mu^+ \nu_\mu$	4	0.79708	0.95420	0.97269	0.98933	1.00000	0.99264	0.99040	0.98032	0.96832	0.95146
$B^+ \rightarrow \bar{D}^0 \mu^+ \nu_\mu$	5	0.79548	0.95924	0.97288	0.98951	0.99264	1.00000	0.99340	0.98642	0.97402	0.95630
$B^+ \rightarrow \bar{D}^0 \mu^+ \nu_\mu$	6	0.80330	0.95944	0.97216	0.98728	0.99040	0.99340	1.00000	0.99277	0.98151	0.95648
$B^+ \rightarrow \bar{D}^0 \mu^+ \nu_\mu$	7	0.79144	0.94812	0.95650	0.97535	0.98032	0.98642	0.99277	1.00000	0.99271	0.97240
$B^+ \rightarrow \bar{D}^0 \mu^+ \nu_\mu$	8	0.77078	0.91678	0.93346	0.95835	0.96832	0.97402	0.98151	0.99271	1.00000	0.98177
$B^+ \rightarrow \bar{D}^0 \mu^+ \nu_\mu$	9	0.74260	0.88765	0.90579	0.93704	0.95146	0.95630	0.95648	0.97240	0.98177	1.00000

Table C.4.: Systematic correlations with the $B^+ \rightarrow \bar{D}^0 \mu^+ \nu_\mu$ sub-sample.

Bibliography

- [1] M. Srednicki. *Quantum field theory*. Cambridge University Press, 2007.
- [2] M. E. Peskin and D. V. Schroeder. *An Introduction to Quantum Field Theory*. Westview Press, 1995.
- [3] D. Griffiths. *Introduction to elementary particles*. John Wiley & Sons, 2008.
- [4] E. Noether. “Invariant variation problems”. In: *Transport Theory and Statistical Physics* 1.3 (1971), pp. 186–207.
- [5] G. Lüders. *On the equivalence of invariance under time reversal and under particle-antiparticle conjugation for relativistic field theories*. Munksgaard, 1954.
- [6] C.-S. Wu, E. Ambler, et al. “Experimental test of parity conservation in beta decay”. In: *Physical Review* 105.4 (1957), p. 1413.
- [7] I. I. Bigi and A. I. Sanda. *CP violation*. Vol. 28. Cambridge university press, 2009.
- [8] A. Bevan et al. (BaBar Collaboration, Belle Collaboration). “The Physics of the B Factories”. In: *European Physical Journal C* 74.11 (2014), p. 3026. DOI: 10.1140/epjc/s10052-014-3026-9. arXiv: 1406.6311 [hep-ex].
- [9] A. Höcker et al. “A new approach to a global fit of the CKM matrix”. In: *The European Physical Journal C - Particles and Fields* 21.2 (), pp. 225–259. DOI: 10.1007/s100520100729. arXiv: hep-ph/0104062 [hep-ph].
- [10] A. Garmash et al. (Belle Collaboration). “Evidence for Large Direct CP Violation in $B^\pm \rightarrow \rho(770)^0 K^\pm$ from Analysis of Three-Body Charmless $B^\pm \rightarrow K^\pm \pi^\pm \pi^\pm$ Decays”. In: *Physical Review Letters* 96 (25 June 2006), p. 251803. DOI: 10.1103/PhysRevLett.96.251803. arXiv: hep-ex/0512066 [hep-ex].
- [11] K. Abe et al. (Belle Collaboration). “Observation of Large CP Violation in the Neutral B Meson System”. In: *Physical Review Letters* 87 (9 Aug. 2001), p. 091802. DOI: 10.1103/PhysRevLett.87.091802. arXiv: hep-ex/0107061 [hep-ex].
- [12] H. B. Nielsen and M. Ninomiya. “A no-go theorem for regularizing chiral fermions”. In: *Physics Letters B* 105.2 (1981), pp. 219–223.
- [13] K. Olive et al. (Particle Data Group). “Review of Particle Physics”. In: *Chinese Physics C* 38 (2014), p. 090001. DOI: 10.1088/1674-1137/38/9/090001.

- [14] C. G. Boyd, B. Grinstein, and R. F. Lebed. “Model-independent determinations of $B \rightarrow D\ell\nu, D^*\ell\nu$ form factors”. In: *Nuclear Physics B* 461.3 (1996), pp. 493–511. DOI: 10.1016/0550-3213(95)00653-2.
- [15] I. Caprini, L. Lellouch, and M. Neubert. “Dispersive bounds on the shape of $B \rightarrow D^{(*)}\ell\nu$ form factors”. In: *Nuclear Physics B* 530.1 (1998), pp. 153–181. DOI: 10.1016/S0550-3213(98)00350-2. arXiv: 9712417 [hep-ph].
- [16] J. A. Bailey et al. (Fermilab Lattice). “ $B \rightarrow D\ell\nu$ form factors at nonzero recoil and $|V_{cb}|$ from 2 + 1-flavor lattice QCD”. In: *Physical Review D* 92 (3 Aug. 2015), p. 034506. DOI: 10.1103/PhysRevD.92.034506. arXiv: 1503.07237.
- [17] A. Sirlin. “Large m_W, m_Z behaviour of the $O(\alpha)$ corrections to semileptonic processes mediated by W”. In: *Nuclear Physics B* 196.1 (1982), pp. 83–92. DOI: 10.1016/0550-3213(82)90303-0.
- [18] LHCb Collaboration. “Determination of the quark coupling strength $|V_{ub}|$ using baryonic decays”. In: *Nature Physics* 11.9 (2015), pp. 743–747. DOI: 10.1038/nphys3415.
- [19] W. Dungel et al. (Belle Collaboration). “Measurement of the form factors of the decay $B^0 \rightarrow D^{*-}\ell^+\nu$ and determination of the CKM matrix element $|V_{cb}|$ ”. In: *Physical Review D* 82 (2010), p. 112007. DOI: 10.1103/PhysRevD.82.112007. arXiv: 1010.5620 [hep-ex].
- [20] B. Aubert et al. (BaBar Collaboration). “Determination of the form-factors for the decay $B^0 \rightarrow D^{*-}\ell^+\nu_\ell$ and of the CKM matrix element $|V_{cb}|$ ”. In: *Physical Review D* 77 (2008), p. 032002. DOI: 10.1103/PhysRevD.77.032002. arXiv: 0705.4008 [hep-ex].
- [21] Y. Amhis et al. (Heavy Flavor Averaging Group (HFAG)). “Averages of b -hadron, c -hadron, and τ -lepton properties as of summer 2014”. In: (2014). arXiv: 1412.7515 [hep-ex].
- [22] B. Aubert et al. (BaBar Collaboration). “Measurement of $|V_{cb}|$ and the Form-Factor Slope in $\bar{B} \rightarrow D\ell^-\bar{\nu}$ Decays in Events Tagged by a Fully Reconstructed B Meson”. In: *Physical Review Letters* 104 (2010), p. 011802. DOI: 10.1103/PhysRevLett.104.011802. arXiv: 0904.4063 [hep-ex].
- [23] K. Abe et al. (Belle Collaboration). “Measurement of $\mathcal{B}(\bar{B}^0 \rightarrow D^+\ell^-\bar{\nu})$ and determination of $|V_{cb}|$ ”. In: *Physics Letters B* 526.3–4 (2002), pp. 258–268. DOI: 10.1016/S0370-2693(01)01483-6.
- [24] J. A. Bailey et al. (Fermilab Lattice, MILC). “Update of $|V_{cb}|$ from the $\bar{B} \rightarrow D^*\ell\bar{\nu}$ form factor at zero recoil with three-flavor lattice QCD”. In: *Physical Review D* 89.11 (2014), p. 114504. DOI: 10.1103/PhysRevD.89.114504. arXiv: 1403.0635 [hep-lat].
- [25] P. Gambino, T. Mannel, and N. Uraltsev. “ $B \rightarrow D^*$ at zero recoil revisited”. In: *Physical Review D* 81 (2010), p. 113002. DOI: 10.1103/PhysRevD.81.113002. arXiv: 1004.2859 [hep-ph].

- [26] H. Na et al. (HPQCD). “ $B \rightarrow D\ell\nu$ form factors at nonzero recoil and extraction $|V_{cb}|$ ”. In: *Physical Review D* 92.5 (2015), p. 054510. DOI: 10.1103/PhysRevD.92.054510. arXiv: 1505.03925 [hep-lat].
- [27] N. Uraltsev. “A ‘BPS’ expansion for B and D mesons”. In: *Physics Letters B* 585 (2004), pp. 253–262. DOI: 10.1016/j.physletb.2004.01.053. arXiv: 0312001 [hep-ph].
- [28] P. Gambino and C. Schwanda. “Inclusive semileptonic fits, heavy quark masses, and V_{cb} ”. In: *Physical Review D* 89 (2014), p. 014022. DOI: 10.1103/PhysRevD.89.014022. arXiv: 1307.4551 [hep-ph].
- [29] J. H. Christenson et al. “Evidence for the 2π Decay of the K_2^0 Meson”. In: *Physical Review Letters* 13 (4 July 1964), pp. 138–140. DOI: 10.1103/PhysRevLett.13.138.
- [30] S. W. Herb et al. “Observation of a Dimuon Resonance at 9.5 GeV in 400-GeV Proton-Nucleus Collisions”. In: *Physical Review Letters* 39 (5 Aug. 1977), pp. 252–255. DOI: 10.1103/PhysRevLett.39.252.
- [31] J. Brodzicka et al. “Physics achievements from the Belle experiment”. In: *Progress of Theoretical and Experimental Physics* 2012.1 (2012). DOI: 10.1093/ptep/pts072. eprint: <http://ptep.oxfordjournals.org/content/2012/1/04D001.full.pdf>.
- [32] S. Kurokawa and E. Kikutani. “Overview of the KEKB accelerators”. In: *Nuclear Instruments and Methods in Physics Research Section A: Accelerators, Spectrometers, Detectors and Associated Equipment* 499.1 (2003), pp. 1–7. DOI: 10.1016/S0168-9002(02)01771-0.
- [33] The Belle Collaboration. *Web center*. <http://belle.kek.jp>.
- [34] E. Nakano. “Belle pid”. In: *Nuclear Instruments and Methods in Physics Research Section A: Accelerators, Spectrometers, Detectors and Associated Equipment* 494.1 (2002), pp. 402–408. DOI: 10.1016/S0168-9002(02)01510-3.
- [35] K. Hanagaki et al. “Electron identification in Belle”. In: *Nuclear Instruments and Methods in Physics Research Section A: Accelerators, Spectrometers, Detectors and Associated Equipment* 485.3 (2002), pp. 490–503. DOI: 10.1016/S0168-9002(01)02113-1. arXiv: 0108044 [hep-ex].
- [36] A. Abashian et al. “Muon identification in the Belle experiment at KEKB”. In: *Nuclear Instruments and Methods in Physics Research Section A: Accelerators, Spectrometers, Detectors and Associated Equipment* 491.1 (2002), pp. 69–82. DOI: 10.1016/S0168-9002(02)01164-6.
- [37] A. Putzer. “Data structures and data-base systems used in high energy physics: Modelling and implementation”. In: *Computer Physics Communications* 57.1 (1989), pp. 156–163. DOI: 10.1016/0010-4655(89)90205-1.

- [38] R. Brun and D. Lienart. “HBOOK User Guide—Version 4”. In: *CERN program library Y 250* (1988), p. 1988.
- [39] R. Brun and F. Rademakers. “ROOT—an object oriented data analysis framework”. In: *Nuclear Instruments and Methods in Physics Research Section A: Accelerators, Spectrometers, Detectors and Associated Equipment* 389.1 (1997), pp. 81–86. DOI: [http://dx.doi.org/10.1016/S0168-9002\(97\)00048-X](http://dx.doi.org/10.1016/S0168-9002(97)00048-X).
- [40] D. J. Lange. “The EvtGen particle decay simulation package”. In: *Nuclear Instruments and Methods in Physics Research Section A: Accelerators, Spectrometers, Detectors and Associated Equipment* 462.1 (2001), pp. 152–155. DOI: [10.1016/S0168-9002\(01\)00089-4](https://doi.org/10.1016/S0168-9002(01)00089-4).
- [41] E. Barberio and Z. Was. “PHOTOS—a universal Monte Carlo for QED radiative corrections: version 2.0”. In: *Computer Physics Communications* 79.2 (1994), pp. 291–308. DOI: [10.1016/0010-4655\(94\)90074-4](https://doi.org/10.1016/0010-4655(94)90074-4).
- [42] R. Brun et al. *GEANT 3.21, Report No.* Tech. rep. CERN DD/EE/84-1, 1984.
- [43] M. Feindt et al. “A hierarchical NeuroBayes-based algorithm for full reconstruction of B mesons at B factories”. In: *Nuclear Instruments and Methods in Physics Research Section A: Accelerators, Spectrometers, Detectors and Associated Equipment* 654.1 (2011), pp. 432–440. DOI: [10.1016/j.nima.2011.06.008](https://doi.org/10.1016/j.nima.2011.06.008). arXiv: [1102.3876](https://arxiv.org/abs/1102.3876) [hep-ex].
- [44] M. Feindt and U. Kerzel. “The NeuroBayes neural network package”. In: *Nuclear Instruments and Methods in Physics Research Section A: Accelerators, Spectrometers, Detectors and Associated Equipment* 559.1 (2006), pp. 190–194. DOI: [10.1016/j.nima.2005.11.166](https://doi.org/10.1016/j.nima.2005.11.166).
- [45] G. C. Fox and S. Wolfram. “Observables for the Analysis of Event Shapes in $e^+ e^-$ Annihilation and Other Processes”. In: *Physical Review Letters* 41 (1978), p. 1581. DOI: [10.1103/PhysRevLett.41.1581](https://doi.org/10.1103/PhysRevLett.41.1581).
- [46] R. Barlow and C. Beeston. “Fitting using finite Monte Carlo samples”. In: *Computer Physics Communications* 77.2 (1993), pp. 219–228. DOI: [10.1016/0010-4655\(93\)90005-W](https://doi.org/10.1016/0010-4655(93)90005-W).
- [47] A. K. Leibovich et al. “Semileptonic B decays to excited charmed mesons”. In: *Physical Review D* 57.1 (Jan. 1998), pp. 308–330. DOI: [10.1103/PhysRevD.57.308](https://doi.org/10.1103/PhysRevD.57.308).
- [48] J. Lees et al. (BaBar). “Study of $\bar{B} \rightarrow X_u \ell \bar{\nu}$ decays in $B\bar{B}$ events tagged by a fully reconstructed B -meson decay and determination of $|V_{ub}|$ ”. In: *Physical Review D* 86 (2012), p. 032004. DOI: [10.1103/PhysRevD.86.032004](https://doi.org/10.1103/PhysRevD.86.032004). arXiv: [1112.0702](https://arxiv.org/abs/1112.0702) [hep-ex].
- [49] P. Urquijo et al. (Belle Collaboration). “Measurement of $|V_{ub}|$ from Inclusive Charmless Semileptonic B Decays”. In: *Physical Review Letters* 104 (2 Jan. 2010), p. 021801. DOI: [10.1103/PhysRevLett.104.021801](https://doi.org/10.1103/PhysRevLett.104.021801).

- [50] A. Sibidanov et al. (Belle Collaboration). “Study of exclusive $B \rightarrow X_u \ell \nu$ decays and extraction of $|V_{ub}|$ using full reconstruction tagging at the Belle experiment”. In: *Physical Review D* 88 (3 Aug. 2013), p. 032005. DOI: 10.1103/PhysRevD.88.032005. arXiv: 1306.2781 [hep-ex].
- [51] G. P. Lepage et al. “Improved nonrelativistic QCD for heavy-quark physics”. In: *Physical Review D* 46 (9 Nov. 1992), pp. 4052–4067. DOI: 10.1103/PhysRevD.46.4052.
- [52] A. X. El-Khadra, A. S. Kronfeld, and P. B. Mackenzie. “Massive fermions in lattice gauge theory”. In: *Physical Review D* 55 (7 Apr. 1997), pp. 3933–3957. DOI: 10.1103/PhysRevD.55.3933.
- [53] C. Bourrely, L. Lellouch, and I. Caprini. “Model-independent description of $B \rightarrow \pi \ell \nu$ decays and a determination of $|V_{ub}|$ ”. In: *Physical Review D* 79 (1 Jan. 2009), p. 013008. DOI: 10.1103/PhysRevD.79.013008.

Acknowledgements

First of all I want to thank my supervisor *Christoph Schwanda*. He supported my work in all possible ways and there was never a moment where I couldn't count on his help and insights. His office was always open for me, and if he wasn't there we would talk at the coffee machine, over Skype or send e-mails back and forth between Japan and Austria. It means a lot that in a field as large and complex as ours I never felt truly lost.

I am grateful for the financing which was provided by the Austrian Science Fund and the JENNIFER project of the European Union in a time where scientists fight hard to find the necessary monetary support.

I am deeply thankful for the scientific and human environment I found at the Institute of High Energy Physics, in which work was always interesting and fun. Especially the people I shared a room with had a huge impact on me: *Felicitas Breibeck*, my fellow physics analyst with whom I could discuss so many concepts of the field, and *Jakob Lettenbichler* who is the person with whom I have talked more about coding than any other person so far. I imagine that all our works improved by helping each other out so much and discussing vital ideas.

I want to thank *Helmut Eberl* for explaining theoretical aspects to me when I had the feeling to be stuck.

It was an honor to be allowed to work for the Belle collaboration and to dive into the complex world of particle physics. All those who contributed, from the people who built this incredible machine to those that manage the daily organization: thank you! Most of all: my internal referees *Jochen Dingfelder*, *Vikas Bansal* and *Ariane Frey* for asking all the questions and suggesting all the improvements that helped to build this analysis.

Finally, I want to thank all those that supported me on a personal level, my family and friends - without you none of this would have been possible. My biggest thanks go to my spouse *Simone*, who always believed in me and had my back. I would not want to face the challenges of the present or the wonders of the future with any other person.

Robin Glattauer

Curriculum Vitae

Hardeggasse 67/32/4

1220 Vienna

✉ robin.glattauer@gmail.com

Education

- since 2013 **Doctorate Studies in the Technical Sciences**, Vienna University of Technology.
- 2005–2012 **Studies in Technical Physics**, Vienna University of Technology, passed with distinction.
- 2004–2005 **Military service**.
- 1996–2004 **Bundesrealgymnasium Gröhrmühlgasse**, Wiener Neustadt.

Work Experience

- since 2013 **Research Assistant for Belle Data Analysis**, Institute of High Energy Physics, Vienna.
- 2011–2012 **Contract for Services: Development of Tracking Software for the Future ILD Experiment**, Institute of High Energy Physics, Vienna.
- 2011 **Tutor**, Laborübungen I für TPH, Vienna University of Technology.
- 2010 **Tutor**, Datenverarbeitung für TPH I, Vienna University of Technology.

Most important publications

- R. Glattauer *et al.* (Belle Collaboration). Measurement of the decay $B \rightarrow D\ell\nu_\ell$ in fully reconstructed events and determination of the Cabibbo-Kobayashi-Maskawa matrix element $|V_{cb}|$. *Phys. Rev. D*, 93:032006, 2016.
- R. Glattauer. Semileptonic B and B_s decays at Belle. *Proceedings of Science*, EPS-HEP page 14, 2015.
- F. Thorne *et al.* (Belle Collaboration). Measurement of the decays $B_s^0 \rightarrow J/\Psi\phi(1020)$, $B_s^0 \rightarrow J/\Psi f_2'(1525)$ and $B_s^0 \rightarrow J/\Psi K^+K^-$ at Belle. *Phys. Rev. D*, 88:114006, 2013.
- R. Frühwirth *et al.* Track finding in silicon trackers with a small number of layers. *Nucl. Instrum. Methods Phys. Res. Sect. A: Accelerators, Spectrometers, Detectors and Associated Equipment*, 732:95–98, 2013.
- R. Glattauer *et al.* Forward Tracking in the ILD Detector. *arXiv*, 1202.2761, 2012.

Outreach and Organization

- 2016 **Instruction of Exhibit-Explainers**, *Natural History Museum Vienna*, Exhibit: “The Beginning of Everything. About Galaxies, Quarks and Collisions”.
- 2015 **Assistant Chairman and Coordinator of Assistant Chairmen**, *European Physical Society: Conference on High Energy Physics*, Vienna.
- 2014 **Design of the Exhibit “Strong Pairs”**, *Exhibition “Wirkungswechsel”*, Touring Austria.
- 2014 **Explainer**, “*Long Night of Research*”, Vienna.
- 2014 **Explainer for Children**, “*Getting in Touch with Physics*”, Elementary School Deutschkreuz.
- 2014 **Assistant Chairman**, *CKM-Conference*, Vienna.
- 2013 **Chairman**, *PASCOS-Conference*, Taipei, Taiwan.
- 2013 **Assistant Chairman**, *Vienna Conference on Instrumentation*, Vienna.

Conference Presentations

- 2015 **Semileptonic B and B_s Decays at Belle**, *European Physical Society: Conference on High Energy Physics*, Vienna.
- 2015 **V_{cb} Measurement with $B \rightarrow D\ell\nu$ at Belle**, *Lake Louise Winter Institute*, Lake Louise, Canada.
- 2014 **V_{cb} Experimental Review**, *CKM-Conference*, Vienna.
- 2014 **Semileptonic B and B_s Decays at Belle**, *International Conference on High Energy Physics*, Valencia, Spain.
- 2013 **Semileptonic B Decays and CKM Elements V_{ub} and V_{cb} from Belle**, *PASCOS-Conference*, Taipei, Taiwan.
- 2011 **Forward Tracking in the ILD Detector**, *International Workshop on Future Linear Colliders*, Granada, Spain.

Language Skills

- German **Mother Tongue**
- English **Fluent**
- Japanese **Intermediate**

Further Knowledge

- Programming Languages **C++, Java, Bash, LabVIEW.**
- Environments **GNU tool chain, KDevelop, IntelliJ IDEA.**
- Tools **make, cmake, google test, SVN, Git, GDB, Valgrind.**
- Others **Photoshop, Gimp, Inkscape, LaTeX.**